Fisheries and Oceans Canada | Pêches et Océans Canada
Ecosystems and Oceans Science | Sciences des écosystèmes et des océans

Canadian Science Advisory Secretariat (CSAS)

Research Document 2026/005

National Capital Region

Assessment of Port Ocean Prediction System Developed Under Canada's Oceans Protection Plan: Strait of Canso

A. Drozdowski[2], M. Dunphy[1], S. Taylor[2], M. Krassovski[1], H. Blanken[1], S. St-Onge Drouin[3], R. Horwitz[2]

[1] Fisheries and Oceans Canada
Institute of Ocean Sciences
9860 West Saanich Road
Sidney, British Columbia V8L 4B2

[2] Fisheries and Oceans Canada
Bedford Institute of Oceanography
1 Challenger Drive
Dartmouth, Nova Scotia B2Y 4A2

[3] Fisheries and Oceans Canada
Maurice Lamontagne Institute
850 route de la Mer
Mont-Joli, Quebec G5H 3Z4

February 2026

Canada

Foreword

This series documents the scientific basis for the evaluation of aquatic resources and ecosystems in Canada. As such, it addresses the issues of the day in the time frames required and the documents it contains are not intended as definitive statements on the subjects addressed but rather as progress reports on ongoing investigations.

Published by:

Fisheries and Oceans Canada
Canadian Science Advisory Secretariat
200 Kent Street
Ottawa ON K1A 0E6

http://www.dfo-mpo.gc.ca/csas-sccs/
DFO.CSAS-SCAS.MPO@dfo-mpo.gc.ca

ISSN 1919-5044
ISBN 978-0-660-97520-7 Cat. No. Fs70-5/2026-005E-PDF

Correct citation for this publication:

Drozdowski, A., Dunphy, M., Taylor, S., Krassovski, M., Blanken, H., St-Onge Drouin, S., and Horwitz, R. 2026. Assessment of Port Ocean Prediction System Developed Under Canada's Oceans Protection Plan: Strait of Canso. DFO Can. Sci. Advis. Sec. Res. Doc. 2026/005. viii + 83 p.

Aussi disponible en français :

Drozdowski, A., Dunphy, M., Taylor, S., Krassovski, M., Blanken, H., St-Onge Drouin, S. et Horwitz, R. 2026. Évaluation du système de prévisions océaniques portuaires élaboré dans le cadre du Plan de Protection des océans du Canada : Détroit de Canso. Secr. can. des avis sci. du MPO. Doc. de rech. 2026/005. viii + 87 p.

TABLE OF CONTENTS

LIST OF TABLES

LIST OF FIGURES

ABSTRACT

Canada's Oceans Protection Plan (OPP) was launched in 2016 to support initiatives aimed at protecting our marine environment from anthropogenic pressures. To this end, the Improving Drift Prediction and Nearshore Modelling sub-initiative of OPP developed six high-resolution port-scale hydrodynamic models, to improve safe navigation, and provide operational emergency response to events such as marine oil spills. The models were downscaled from the Coastal Ice-Ocean Prediction Systems East and West (CIOPS-E, CIOPS-W). Atmospheric forcing was provided by the High-Resolution Deterministic Prediction System (HRDPS). Model performance is assessed against available observational data and contrasted with the parent model CIOPS-E using a multi-year hindcast. Evaluations of 48-hour forecasts are performed during a two-month period.

This report reports the assessment of the nested Strait of Canso port models (STC500 and STC100). Water level was found to be well modelled by the three models examined, with the finest resolution (STC100) port model improving scores by ~10%. The analysis showed that only 2.2% of unmodelled variance remains, with the bulk of it in the non-tidal component. Stability of the models was demonstrated with consistent scores and tidal constituents for each of the five years examined. Scores during extreme weather events (six large storms) were found to be within the expected range with the exception of two storms where the models underestimated the harbour seiching. The water level forecast evaluation found the model scores to be within the acceptable range during the 48-hour forecast period. In terms of the evaluation of currents, the port models demonstrated a large improvement over CIOPS-E inshore, and where topography played a role, particularly near the bottom. No significant improvement was found for the stations examined on the open shelf. However, drifter analysis did show a moderate improvement over CIOPS-E in terms of drift scores. Overall port model temperature and salinity scores were close to CIOPS-E but had significant improvements in near-bottom coastal regions, where resolution of bathymetry plays a role. In particular, the port models were able to model over the sill deep water renewal, a process unresolved by CIOPS-E.

1. INTRODUCTION

Under the Improving Drift Prediction and Nearshore Modelling (DPNM) sub-initiative of Canada's Oceans Protection Plan (OPP), high-resolution models were developed for six Canadian ports and their approaches to enhance the Government of Canada's ocean modelling capabilities in support of environmental protection and marine safety applications (e.g., drift prediction for oil spills) and safety for navigation via a hydrographic e-navigation application. The six ports (three on the east coast and three on the west coast) were selected as at-risk for environmental incidents owing to their high tanker traffic and complex navigational needs. Models have been developed for the west coast ports of Kitimat, Lower Fraser River and Vancouver Harbour, and for the east coast ports of Saint John, the Strait of Canso, and the St. Lawrence estuary.

The models have been developed with both hindcast and forecast capabilities. For each port, a multi-year hindcast is presented with model validation against observations of water levels, velocities, temperature and salinity, as well as a drift experiment conducted using available drifters. Forecast performance is assessed over a two-month period.

The purpose of this document is to review the performance of the model for the Strait of Canso. The design is common to all port models and is presented in Section 2, while Section 3 describes the specifics of the Strait of Canso port model. The evaluation parameters used to evaluate all models are detailed in Section 4, and Sections 5 and 6 respectively analyze the long hindcast evaluation results and the forecasts evaluation results for the port of Strait of Canso. The performance of the Strait of Canso port model is summarized in Section 7, and the main key findings are listed in Section 8.

2. PORT MODEL DESIGN

The port models ("port ocean prediction systems," or POPS) follow a common structure designed to constrain system complexity. We use the same ocean general circulation model and code version, downscaling strategy, preprocessing tools, surface forcing product, and automation suite for all six POPS. The model grids, configuration/tuning, open boundary forcing, and freshwater input sources differ between POPS configurations.

2.1. MODEL SELECTION

The precursor to much of the OPP port modelling effort was conducted using the Finite Volume Community Ocean Model (FVCOM) (Chen, Liu, and Beardsley 2003) under the World Class Tanker Safety System (WCTSS) program, yielding prototype models for ports of Canso, Kitimat, and Vancouver Harbour. Even earlier, there have been modelling efforts based on Backhaus (Backhaus 1983; 1985) yielding models for the St. Lawrence estuary (Saucier and Chassé 2000) and the Gulf of St. Lawrence (Saucier 2003). These were then followed by implementation of an equivalent NEMO model by Environment and Climate Change Canada (ECCC), the Regional Marine Prediction System (RMPS) GSL. The RMPS was operational from 2011 to 2021, though none of these earlier models were considered for use in OPP. The WCTSS FVCOM prototypes used unstructured model meshes to resolve the coastal regions to within tens of metres or less, with resolution gradually decreasing to kilometres to match the parent model grid on the open boundary.

FVCOM has no history of operational deployment in Canada, while NEMO 3.6 (Nucleus of European Modelling of the Ocean) is used operationally by the Canadian Operational Network for Coupled Environmental PredicTion Systems (CONCEPTS). In the early part of OPP, a

comparison exercise between FVCOM 4.1 and NEMO 3.6 (Nudds et al. 2020) informed the decision-making process to select which codebase to use for the POPS models. Both codebases were used to construct models of the Bay of Fundy and the Port of Saint John (Paquin et al. 2020), which was chosen due to the large tides and complex circulation. NEMO 3.6's most significant deficiency in this context is the lack of wetting and drying, so if NEMO 3.6 could provide satisfactory results in the Bay of Fundy, then it would likely be suitable for use in the other regions. The two models were evaluated on how well they matched observations, as well as on computational efficiency, stability, and robustness. Both models were found to be skillful at reproducing observed data: neither model was significantly superior, and the choice of model to use going forward rested more heavily on the other factors.

Ultimately the decision was taken to proceed with NEMO 3.6, despite its structured grid, a somewhat coarser nearshore resolution, and higher demand for computational resources, to facilitate operationalization and align with modelling efforts at ECCC. Additional advantages of NEMO include active development that delivers regular code updates and bug fixes, an international NEMO Consortium group where members steer code development, and a well-established international operational modelling community.

Thus the ocean model used for all port ocean prediction systems is the CONCEPTS code: a fork of NEMO 3.6 (Madec 2016) that has been customized to meet the operational needs of CONCEPTS, for example (Dupont et al. 2015).

2.2. DOWNSCALING STRATEGY

The port models are downscaled solutions driven by larger-scale coastal ocean models currently operational at ECCC: the Coastal Ice-Ocean Prediction Systems East and West (CIOPS-E, CIOPS-W; Paquin et al 2021a, Paquin et al 2021b) have 2-2.5 km resolution, and Salish Sea 500 (~500 m resolution) which is part of the CIOPS-W system. Output from these models forms the boundary conditions for our higher-resolution, smaller-area models. We use two levels of nesting to achieve a resolution fine enough to reach port scale. The nesting is one-way (coarse to fine), so no information is fed back to the larger scale models, allowing the models to run sequentially but otherwise independently of each other. This one-way nesting strategy also enables systematic errors to be corrected at the open boundaries.

We do not employ a dynamic ice model. Instead, we use a NEMO feature called "ice if", which uses input ice fields and the local freezing point to assess where ice cover exists, and in those locations it restores the sea surface temperature to the local freezing point and sets heat fluxes to -4 Wm^{-2} (Madec 2016).

We do not employ data assimilation or spectral nudging; all model runs are free runs.

River discharge data is used where available to supply the most realistic freshwater input to the model, and climatology is used when this is not available. Gauge data is also used in some cases to construct water level boundary conditions.

2.3. SIMULATION SEQUENCING

The port models operate in three configurations: hindcast, pseudo-analysis and forecast. Hindcasts are the most straightforward, using larger-scale model forcing and quality-controlled gauge data to drive the models. The model begins in the past from a cold-start (temperature and salinity interpolated as initial conditions, water at rest) or a hot-start (temperature, salinity, velocity, and sea-surface height interpolated as initial conditions) and reaches a spun-up state after a period of adjustment to the forcing. The model output is considered usable once spun up, and the model can run nearly up to the present in this configuration, provided that forcing data is

available. Pseudo-analysis runs are daily runs that keep the model state caught up to near-real-time, and do not include a direct data-assimilation component. Rather, the state is indirectly driven by data via boundary and surface forcing terms. These runs are used to initialize the first forecast of each day and may use different input than hindcasts depending on what data is available in real-time.

The pseudo-analysis and forecast schedule is chosen to match the schedule of the parent models that we use for forcing. Shortly after 00Z each day, a 24 hour pseudo-analysis simulation runs to catch up the model state to 00Z. This process uses restart files (so no spin up needed) and, where possible, uses gauge data drawn from a near-real-time data feed which receives limited quality control. Following the pseudo-analysis, the POPS generates four forecasts per day, each 48 hours long, which start from 00Z, 06Z, 12Z and 18Z. The daily 00Z forecast starts using the restart file from the daily pseudo-analysis and runs for 48 hours, saving a restart file six hours into the simulation. The 06Z forecast starts from this restart file, also saving a restart file six hours in, and similarly for the 12Z and 18Z forecasts. A schematic of this setup is shown in Figure 1. We focus only on the 00Z forecasts in this evaluation.

While the 00Z forecast simulation is nominally started at 00Z each day, in practice, the initialization of the simulation is delayed as it can not begin until all inputs are available from the larger scale models and the pseudo-analysis completes. At time of writing, this delay is approximately 5 hours, such that upon completion, each forecast simulation has about 43 hours of output that is in the future.

2.4. SURFACE FORCING

Surface forcing is derived from the High-Resolution Deterministic Prediction System (HRDPS) (Milbrandt et al. 2016) that runs operationally at ECCC and provides atmospheric weather forecasts four times per day at 2.5 km resolution. This is the highest-resolution operational atmospheric product available and is chosen to be consistent with the forcing used in CIOPS-E/W. In hindcast and pseudo-analysis mode, we use a time-blended form of the HRDPS forecasts, where hours 06–17 from successive forecasts are combined using weighted averaging to form temporally continuous fields with the same blending schedule as CIOPS-E/W. Additional details are given in the technical documentation for CIOPS-W version 1.5 (Paquin et al. 2022). Time blending is not used for forecasts.

The surface forcing is applied to the NEMO model using the CORE algorithms (Large and Yeager 2004) with modifications by ECCC to (a) read input data from the in-house RPN file format and (b) use the lowest diagnostic level of the atmospheric model rather than the conventional 2 m and 10 m data. Precipitation and sea-level pressure variations are also applied to the surface of the model.

2.5. AUTOMATION SUITE

The hindcast, pseudo-analysis and forecast simulations are all managed using ECCC's Maestro sequencing software. We have constructed a Maestro suite that is based on ECCC's CIOPS-E/W suites, where we use some of ECCC's functionality for the atmospheric forcing preparation and the mechanics of running the NEMO model, including managing restart files and outputs. We augment this baseline with functionality to prepare boundary forcing, extract data from the real-time data feed, generate the runoff forcing and prepare ice-concentration input files for the "ice-if" feature. Fallback strategies for missing data and persistence strategies for forecasts using gauge data are also implemented here.

2.6. ROBUSTNESS AND LIMITATIONS

For an operational model to be useful, it must be robust and not prone to failure. We have not assessed the models exhaustively in this regard; such testing is an ongoing process. However, some aspects have been explored:

- Where gauge data is needed as a model input, fallback mechanisms are implemented to mitigate missing or bad gauge data. Typically, this means we prepare a climatology for each gauge to stand in when the gauge data is unavailable. With these prepared ahead of time and with appropriate tooling to automate the switchover, the models can run despite missing gauge data and experience a graceful degradation through forcing with lower-quality data rather than a failure. Measuring the severity of the degradation under data-loss scenarios is reserved for future work.
- A long hindcast is conducted for model performance assessment. This long simulation demonstrates that the model is stable subject to a multi-year sample of weather/forcing conditions. In some cases, the hindcast period samples some extreme events, which helps bolster the case for model stability.
- Daily demonstration simulations (pseudo-analysis and four forecasts) have run for order one year on the General Purpose Science Cluster (GPSC) on a best-effort basis, to show that the automation suite can run the models routinely and reveal edge cases that can be fixed to improve robustness further. The purpose of running these pre-operational, best-effort simulations is to demonstrate the functionality/stability of the NEMO-based numerical model and the driving automation suite, and identify issues that would impact operational deployment. The dominant source of issues experienced that impede on-schedule daily forecasts are (a) GPSC compute system downtime, both planned and unplanned, and (b) lack of availability of the forcing data from the larger-scale models that are nominally mirrored on schedule from ECCC's systems. These issues are deemed an expected consequence of using a research cluster and would be mitigated using an operational cluster.

The models will have some limitations:

- Intrinsic variability is expected in each model, and this has not been characterized.
- The lack of wetting and drying capability in NEMO 3.6 requires artificial bathymetry deepening in intertidal regions.

3. STRAIT OF CANSO

3.1. REGIONAL OCEANOGRAPHY

Figure 2 and Figure 3 provide maps of the port area. A brief description of the port is taken from Drozdowski and Horne (2022), hereafter DH22:

> "The Strait of Canso is actually a 20 km long, 2-3 km wide fjord with steep sides and a 35-55 m deep main channel behind a 30 m sill near the entrance. The name is retained from the original strait that separated Cape Breton Island from the mainland and was blocked by a causeway in the 1950s. The causeway is fitted with a small lock to accommodate small-to-medium-sized vessel traffic during ice-free months and separates the head of the strait from the Gulf of St. Lawrence. The causeway was treated as a closed land boundary by the present model, as the through-flow is negligible (Bugden et al. 2020). The strait is connected to the open shelf through Chedabucto Bay, a large bay roughly 20 by 30 km and as deep as 150 m. The region has two rivers

> Guysborough and Inhabitants, with climatological average monthly discharge peaking in April at 17 and 33 $m^3 s^{-1}$. The entire Canso-Chedabucto embayment has a water shed area of 2148.4 km^2 with maximum discharge of 155 $m^3 s^{-1}$ (Gregory 1993). The water properties of the region are typical of the inner eastern Scotian Shelf (Petrie et al. 1996), largely influenced by runoff from the Gulf of Saint Lawrence."

The seasonal T-S cycle and stratification in the region is summarized by Drozdowski and Jiang (2020), hereafter DJ20:

> "Salinity increases from the surface to about a depth of 100 m (top layer) in a near-linear fashion for all seasons and is near-constant below that (bottom layer). The surface salinity peaks at 30.5 during winter and spring and has a minimum of approximately 29.7 in the fall, consistent with the outflow from the Gulf of St. Lawrence and the Nova Scotia Current (Drinkwater et al. 1979). Salinity in the bottom layer peaks in the summer at approximately 33 and drops to 32.3 in the winter. Temperature profiles in the top layer are also near linear and near constant in the bottom layer. Surface temperatures vary greatly throughout the year, starting off near 0°C in winter and peaking at 15°C in the summer. Bottom temperatures do not vary significantly throughout the year staying in the 0.5°–2°C range. The salinity profile is the main driver of stratification leading to buoyancy frequencies above 0.01 s^{-1} in the top layer year-round. Temperature only contributes significantly to stratification in the summer, when it pushes the buoyancy frequency to its highest seasonal value around 0.025 s^{-1}."

The mean (large) tide range in the strait is 1.40 (2.00) m as reported by Gregory (1993). They report mean (peak) tidal currents of 0.02 (0.03) m/s inside the inner part of the strait and 0.05 (0.08) m/s in the outer and approaches. The strongest barotropic tidal currents are in the entrance to Chedabucto Bay at 0.2 m/s (DJ20). Additionally, the strait has an active internal M2 tide as reported by DJ20, which varies seasonally with stratification, at its peak can producing near-surface and near-bottom baroclinic tidal currents which exceed the barotropic and lead to enhanced mixing through dissipation.

The Canso Strait, Chedabucto Bay complex has an active seiche which can cause water level to change by tens of centimeters with period of 2-4 hours. Barber and Taylor (1977) investigated the resonant response of the embayment using a two-dimensional circulation model, and found the model reproduced the strong resonance response observed in the 2-4 hour band of the water level spectra. Harbour seiches are excited by the passage of storms and presence of external oceanic forcing in the resonant band (Petrie 2022).

Deep water renewal in the strait is limited by a sill. DH22 reports episodic deep water renewals of the type often observed in fjords:

> "As the station is a deep nearshore station, isolated behind a sill, near-bottom T-S (CW2016-57m) characteristics are very different from the CB-49m station outside. The salinity remains between 30.5 and 31.5 g kg-1 during the observation period. The water stays cool all summer, peaking at 8°C in October. Synoptic fluctuations were not present, and the overall trends were linear increase (decrease) for temperature (salinity), interrupted by episodic step-like features indicative of external water intrusions over a sill. This process is known to contribute to stagnant water renewal in fjords (Farmer and Freeland 1983)."

3.2. DOMAIN AND CONFIGURATION

The grid design strategy for the port models aimed to downscale CIOPS-E to the port area by reducing the grid spacing to 1/5 of the parent in two steps. The resulting two Strait of Canso port

model domains have nominal horizontal spacing of 500 and 100 m (nesting and bathymetry are show in Figure 2). Both grids follow the tri-polar ORCA configuration following Drakkar Group (2007). The Strait of Canso 500 m (hereafter STC500 or Canso500) resolves the Strait of Canso, Chedabucto Bay and coastal margins, as well as a part of the inner eastern Scotian Shelf. The finest resolution, Strait of Canso 100 m grid (hereafter STC100 or Canso100) extent is limited to the coastal regions of the port. The narrowest parts of the Strait are resolved with four grid cells in the 500 m model and twenty grid cells in the 100 m model. The 2.5 km resolution of the HRDPS atmospheric forcing product is similar to the width of the strait. These domains extend far beyond the strait proper because there are industrial terminals and offloading points along and just outside of the strait, which draw high-risk ship traffic throughout the area. The vertical grid for STC500 (STC100) has 47 (39) z-levels with both partial cells and a variable volume formulation (Levier et al. 2007). Vertical resolution for both models decreases from 1 m in the surface, to ~18 m in the deepest cells. The water depth in the STC500 (STC100) does not exceed 353 (197) m. Bathymetry for both grids was generated by an interpolation of data files assembled from various requests (2015-2017) made to the Canadian Hydrographic Service (CHS). Prior to interpolation, the bathymetry was decimated to 200 m for STC500 and 50 m for STC100, using a median filter. This was done to create a more uniform product before interpolation, as the original data had patches of dense data (e.g., multi-beam) mixed with regions of low data availability. The 200 m decimated bathymetry is shown in Figure 4. The model bathymetry uses Chart Datum (CD) depths. The CanCoast coastline product (Atkinson et al. 2016) was used to delineate land from ocean. As NEMO 3.6 does not have a wetting and drying formulation, to ensure model stability, water depths less than 5 m were set to 5 m. Key model setup features from are included in Table 1.

3.3. INITIALIZATION

Each port model was initialized (hot-started) with saved temperature, salinity, sea-surface height and velocities fields from the parent model. A horizontal flooding-type extrapolation near coastlines and a vertical extrapolation near the bottom was done as needed to ensure initialization of all grid points. STC500 was initialized on 5-Feb-2016 while STC100 on 9-Feb-2016.

3.4. OPEN BOUNDARY FORCING

Both port models used the *specified* NEMO3.6 open boundary condition (OBC) for 3D fields and Flather (Flather 1976) for 2D fields. STC500 had an east, south and west open boundary, while STC100 had east and south. Temperature, salinity, sea-surface height and velocities fields at open boundaries for each port model were supplied by the parent model at 1-hour intervals. No filtering was required to correct the tides and this signal was inherited directly from each parent model through sea-surface height and velocities fields as specified on the open boundaries. The sea surface height was passed from CIOPS-E to STC500 without any adjustment for vertical datum, so STC500 and STC100 sea surface heights inherit CIOPS-E's EGM-DIR-R4 geoid datum. The vertical datum used by CIOPS-E was not known at the time of model development. The difference between the Chart Datum used for bathymetry and the EGM-DIR-R4 datum used for sea surface height forcing could lead to a small (~1.6 m) error in total water depth, which is expected to have a negligible impact on the dynamics.

Smoothing of bathymetry was applied within the first 10 grid cells of the open boundaries to ensure a smooth transition from the parent model. For STC500, the eastern boundary required additional smoothing to improve the advection of the coastal freshwater signal associated with the runoff from the Gulf of Saint Lawrence into the port domain.

3.5. FRESHWATER INPUT

The region has no large river inputs. The two largest rivers, Guysborough and Inhabitants, have combined climatological average monthly discharge peaking in April at 40 m^3 s^{-1}. However, early test revealed that local spring runoff had a small impact on SST which CIOPS-E was able to model effectively with its monthly climatological runoff inputs, which discharged freshwater over a large patch near the coast. The discharge was spread over top 7 m and had no modification to temperature. The same strategy was adopted for the port models by interpolating the discharge mask from CIOPS-E to each port model grid.

3.6. ICE MODEL

None, but NEMO's "ice-if" formulation is used as temperature limiter (see Section 2.2).

3.7. MODELLING SYSTEM STABILITY

The robustness of the present port modelling system was demonstrated by the ability to hot-start and run 6 years of stable hindcast without the models becoming unstable or drifting (Section 5; e.g. Figure 9). The hindcast period included a number of weather events, six of which were chosen for closer investigation and revealed no flaws in the modelling system. Additionally, a set of 60 00Z 48-hour forecasts were carried out and evaluated during this period.

Aside from the hindcast and forecast evaluation discussed in this report, the Strait of Canso models ran in demonstration mode (demo) on GPSC using an automation system ("port_models Maestro suite") which runs the daily pseudo-analysis and forecasts runs. The Strait of Canso models came online in demo mode in the summer of 2021 and remained running until the GPSC migration in 2022.

Systematic stress testing, including but not limited to applying exaggerated forcing, to probe the stability limits has not been conducted at the time of writing and is reserved for future work.

4. EVALUATION METRICS

The model performance is assessed through the analysis of a multi-year hindcast and a shorter set of forecasts, where the dates considered are constrained by available surface and boundary forcing from larger scale models. The hindcast evaluation uses a wide set of observations to analyze the model's representation of ocean conditions, including tidal analysis and model drift that would be difficult to assess on a short model run. Meanwhile, the forecast evaluation focuses on measuring the degradation of model skill as a function of forecast lead time for a smaller set of observations available during the forecast period.

Quality controlled data sources were preferred where possible. We performed additional quality control to some data as needed, including visual inspection, thresholding and automatic de-spiking to eliminate suspect data.

4.1. HINDCAST

Hindcast performance is assessed through comparison with available observational data. For each observation, we extract the corresponding virtual observation from the model. The error is defined as

$$\text{ERROR} = \mathcal{X}_m - \mathcal{X}_o ,$$

where $\mathcal{X}_o$ and $\mathcal{X}_m$ are the observed and modelled values such that a positive/negative value indicates a model over/underestimate. For currents, $\mathcal{X}_o$ and $\mathcal{X}_m$ are taken as complex numbers with the real part representing the eastward and imaginary the northward components of velocity.

We use several scores, the bias, the centered root mean square error (hereafter CRMSE) and the root mean square error (hereafter RMSE),

$$\text{bias} = \frac{1}{N}\sum \text{ERROR} = \frac{1}{N}\sum \mathcal{X}_m - \frac{1}{N}\sum \mathcal{X}_o = \overline{\mathcal{X}_m} - \overline{\mathcal{X}_o},$$

$$\text{CRMSE} = \sqrt{\frac{1}{N}\sum (ERROR\text{-}bias)^2},$$

$$\text{RMSE} = \sqrt{\frac{1}{N}\sum ERROR^2} = \sqrt{bias^2 + CRMSE^2},$$

and these measures retain the units of $\mathcal{X}$.

We also use the unitless gamma squared score,

$$\gamma^2 = \frac{CRMSE^2}{\sum(\mathcal{X}_o - \overline{\mathcal{X}_o})^2},$$

which is the ratio of error variance to observed variance, such that zero indicates perfect agreement between model and observation variance, and unity indicates error variance is as large as the signal variance. A value of unity or larger indicates no skill.

For scalar quantities, we use the unitless sample Pearson correlation coefficient score,

$$\text{PEARSONR} = \frac{\sum(\mathcal{X}_m - \overline{\mathcal{X}_m})(\mathcal{X}_o - \overline{\mathcal{X}_o})}{\sqrt{\sum(\mathcal{X}_m - \overline{\mathcal{X}_m})^2 \sum(\mathcal{X}_o - \overline{\mathcal{X}_o})^2}},$$

where zero indicates no correlation and unity indicates perfect correlation. For vector quantities (currents) we have the vector correlation coefficient (Kundu 1976; Röhrs and Christensen 2015),

$$\text{VECTORR} = \frac{\sum(\mathcal{X}_m - \overline{\mathcal{X}_m})^* (\mathcal{X}_o - \overline{\mathcal{X}_o})}{\sqrt{\sum(\mathcal{X}_m - \overline{\mathcal{X}_m})^2 \sum(\mathcal{X}_o - \overline{\mathcal{X}_o})^2}},$$

where the asterisk represents complex conjugation, which is also implied for squaring of complex numbers. This quantity is a complex number, where the magnitude measures the overall correlation and the angle is a measure of the average angle of the modelled current with respect to the observation. Here we compute the angle as positive clockwise to be consistent with the convention of representing the velocity direction as positive clockwise from North. Lastly, the vector correlation angle is only considered meaningful when the correlation magnitude is large (Kundu 1976).

4.1.1. Water level

Water level observations from the Canadian Hydrographic Service (CHS) are transformed from CHS Chart Datum to Canadian Geodetic Vertical Datum of 1928 (CGVD28) by subtracting a station-specific offset. CHS provides these offsets are based on measurements from a GNSS (Global Navigation Satellite System) occupation at each station. Pacific US stations are shifted from the US datum to CGVD28 via NOAA's VDatum and NRCan Vertical Datum Transformations online tools. Atlantic US stations were gathered with a mean low-low water datum and converted to CGVD28 using conversion surfaces provided by CHS. Water level

observations from the Water Survey of Canada (WSC) are shifted to CGVD28 using offsets provided by WSC.

Tidal analysis is performed using T_TIDE on one-year segments at an hourly sampling interval. Where data is available at a higher frequency, it is interpolated/subsampled to hourly frequency. Observations missing more than 10% of the data points are not detided. The tidal analysis enables the decomposition of the total water level into tidal and non-tidal parts as

$$H_{total} = H_{tidal} + H_{nontidal}.$$

The annual (SA) and semi-annual (SSA) constituents are excluded from the tidal analysis; these constituents are subsumed into the non-tidal component. For the present purpose this is adequate as the same process is applied to both model and observations, and the extent to which the models do not reproduce SA or SSA is captured in the non-tidal error scores. Constituents with signal-to-noise ratios below 2 are also subsumed into the non-tidal part. Water level bias is included in the non-tidal component. Scores are reported for the total, tidal and non-tidal components. Owing to a negligible cross-correlation between tidal and non-tidal water levels, to a good approximation, we have

$$\mathrm{CRMSE}^2_{total\,wl} \cong \mathrm{CRMSE}^2_{tidal\,wl} + \mathrm{CRMSE}^2_{nontidal\,wl},$$

which shows how these two errors contribute to the total. Amplitude and phase errors are reported for the significant constituents, as is the tidal error,

$$\text{TIDAL ERROR} = \left[\frac{1}{2}({h_o}^2 + {h_m}^2) - h_o h_m \cos(\phi_o - \phi_m)\right]^{\frac{1}{2}},$$

where h_o and ϕ_o are the observed (subscript *o*) amplitude and Greenwich phase lag for a given tidal constituent, while h_m and ϕ_m are the modeled (subscript *m*) amplitude and phase (Cummins and Oey 1997).

4.1.1.1. Storm surge evaluation

To evaluate the port models' performance during storms, a handful of stormy periods are selected for each port. The cyclone database of (Zhang et al. 2019), which provides global storm tracks from 1958 to 2021 (Figure 5 shows a zoom of North America), guides the selection. The database was queried for storms passing within a few hundred kilometres of each port model domain, and it provides a comprehensive list of storm events during the hindcast period. However, this list is quite extensive for some ports (particularly Canso and Saint John), so longer lists are narrowed down by considering minimum central pressure, examining water level gauges, and local media reports of storm impacts. The evaluation follows the residual water level hindcast evaluation in terms of performance scores and plots but is limited to the storm periods.

Storm surge detiding is done using a 40-day window around the storm's peak, i.e., 20 days before to 20 days after. This differs from the typical water level analysis, which is done in yearly spans and as such can include more constituents. However, using a shorter window does a better job removing the tides during each storm, particularly in areas with non-stationary tides.

We note that storm surges may interact non-linearly with tides to impact water levels, but we do not investigate this phenomenon here.

4.1.2. Water velocity

Velocity data is available from ADCPs and some current metres in one of four configurations: mounted on a mooring, buoy mounted (i.e., floating), in a float towed by a ship, or horizontally mounted on a shore structure (HADCP). Only horizontal (east-west / north-south, u/v) velocities

are considered here. The horizontal velocity's u/v and speed/direction decompositions are both considered, and directions are calculated as positive clockwise from north.

Model data is extracted to match the observed data's time span and spatial location. Time series longer than 29 days and with less than 10% of data points missing are detided using T_TIDE; hourly data is used for detiding, and where more frequent data is available, it is first down sampled. As with water level, the SA and SSA constituents are excluded from fitting, a Rayleigh value of 2 is used, and the observations and model data are processed the same way.

Currents are noisier, tend to have more missing data, are less stationary, and are impacted by more non-linear processes than water level observations, and these factors make the detiding process less robust. Owing to nonlinear processes such as bottom friction, some tidal (kinetic) energy will spread into adjacent frequencies, so fitting to tidal harmonics does not capture all variability induced by the tides, and some near-tidal variability remains in the residual velocities. We do not apply low-pass or band-stop filters to the residual to reduce the noise. While doing so would provide a more completely de-tided residual time series, some of the total signal would be unaccounted for by either the tidal or non-tidal evaluation. Given these caveats, the tidal component may be more accurately described as "the component of the currents that T_TIDE is able to fit." Currents are evaluated using similar metrics to water level, using complex formulations. Tidal constituents are evaluated using the ellipse error (Cummins and Thupaki 2018).

$$D_u = \left[\frac{1}{2}(A_o^2 + B_o^2 + A_m^2 + B_m^2) - \cos(g_o - g_m)\cos(\theta_o - \theta_m)(A_o A_m + B_o B_m) - \sin(g_o - g_m)\sin(\theta_o - \theta_m)\,(A_o B_m + A_m B_o)\right]^{1/2},$$

where A and B are semi-major and semi-minor axes, respectively, the subscripts *o* and *m* correspond to observed and modelled, g is phase, and θ is angle of inclination. For the non-tidal and total time series, complex formulations of the metrics listed at the beginning of the section are used, including bias, CRMSE, γ^2, and vector correlation.

We note that for single-location instruments, in particular moored current meters and moored and horizontally mounted ADCPs, we expect the scoring to be sensitive to the details of the model run under evaluation. Small errors in bathymetry can adjust the location of deterministic features (eddies, jets, meanders, etc.) and this can lead to large errors in the scoring. Meanwhile, chaotic internal variability can also affect the location of such features. An ensemble of model runs could help mitigate the latter but is beyond the scope of the current effort.

4.1.2.1. Horizontal ADCPs

HADCP data is decomposed into along- and cross-channel components, and evaluation is done primarily with mid-beam data to avoid edge effects. When a long enough time series is available, a tidal analysis is done as with moored instruments. Time series of the first week of data are plotted, regardless of how long the total time series is, to show the daily variability in the signal and how well the model captures it. Scatter plots are used to show the distribution of speed and direction of the total velocity, and the semi-major axis for the tidal ellipses are compared when feasible.

4.1.2.2. Current meters and moored ADCPs

Current meters report velocity at a single depth, so those velocities are evaluated at instrument-specific depths. For ADCPs on moorings or buoys, a standard set of depths at which to evaluate the velocities is selected on a per-port basis, taking into account local bathymetry and data availability; for brevity, statistics may be reported only at some depths for each instrument

considered. These levels are defined relative to either a nominal surface (i.e., one with no sea-surface height variation) or the time varying sea surface. For regions with ADCPs in relatively deep water without a large tidal range, using the nominal surface is sufficient. For shallow regions and/or those with large tidal ranges, the evaluation is done relative to the time-varying sea surface, using the observed total water depth to process the observations and modelled sea surface to process the modelled currents.

The observations are preprocessed to remove any spurious data points: values larger than 10 m/s are discarded and the data points are resampled if needed to be evenly spaced.

Tidal analysis is done on all timeseries of at least 29 days at depths with less than 10% of the data missing. Tidal ellipses are plotted for the largest tidal constituents, including depth profiles of tidal ellipses for the largest constituents. Time series and histograms are plotted for both the non-tidal and total velocities. Analysis of total velocities only is done for shorter time series or time series with missing data. We note that if data is missing at consistent phases of the tide, then the analyzed results may be aliased, and so time series with substantive regular gaps are not analyzed or presented.

4.1.2.3. ADCP transects

ADCP transects are too short for tidal analysis, so only the total velocities are considered. An along-transect / cross-transect decomposition is used, with a constant angle used for decomposition for the entire transect; this is sufficient as the transects are typically short and straight. Along-transect plots of velocities at depth are used for evaluation. Scatter plots of bias vs CRMSE are also plotted, with the statistics calculated at each physical point and integrated over the transect.

4.1.3. Water properties

Conductivity-Temperature-Depth (CTD) profiles are grouped into manually defined subregions based on the geography of each port domain. This enables an aggregate assessment over areas, including bias and CRMSE as a function of depth for each area. Model results are taken from the nearest point to the data location and nearest to the observation time. Vertical profiles are interpolated to the model z-levels to bring all data to consistent depths.

Sea surface temperature buoy and moored CTD measurements are evaluated using the bias, CRMSE, χ^2 and Pearson's *r* scores over the evaluation period. Model values are linearly interpolated to observation locations in the horizontal and vertical dimensions. The observed and modelled time series are interpolated to the largest common data interval.

Ferry thermosalinographs are vessel-mounted temperature and conductivity sensors. They provide a measure of near-surface water temperature and salinity by collecting data through one of the vessel's seawater circuits. Model results for comparison with these data are taken from the point nearest to the observed locations both horizontally and vertically and then linearly interpolated to the observation times. Hovmöller plots of observations, model results and differences, plus basic statistics, are used to assess the model performances relating to near-surface water.

4.1.4. Drift

The models' performance in drift trajectory prediction is assessed by comparing the observed tracks of ocean surface drifters with analogous trajectories modelled using the surface currents output by the port models, in combination with wind forcing from the National HRDPS atmospheric forecast. This comparison is done using the drift evaluation tool developed as part of the DPNM sub-initiative, in the OpenDrift configuration (Soontiens and Holden 2024).

Windage on the surface drifters is applied by computing the wind drag coefficient based on the drifters' drag area ratio (Niiler et al. 1995; Daniel et al. 2002; Röhrs et al. 2012; Hourston 2021; Blanken et al. 2021). This coefficient parameterizes the effect of direct wind drag on the parts of the drifter exposed above the water surface and varies with drifter geometry. To account for wave-induced Stokes' drift, an additional 1% of the wind speed is added (Sutherland et al. 2020), and this sum is applied as the windage in the trajectory prediction.

This method of applying windage assumes that currents over the draft of the drifter are known exactly, as are winds directly at the ocean surface. However, in reality, neither of these assumptions is true, since:

1. The representation of surface currents in NEMO is limited by stability restrictions on near-surface vertical resolution and model uncertainty in general; and
2. Wind speed from the HRDPS model is also subject to model uncertainty and given at 10 m where winds are usually ~30% larger than at 1 m but could be as much as five times larger depending on wind speed and atmospheric stability (Smith 1988).

The representation of Stokes' drift as 1% of the wind speed represents a further assumption, as this value was derived by comparing tracks from various types of surface drifters to currents from the Regional Ice-Ocean Prediction System (RIOPS) ocean model and Canadian Arctic Prediction System (CAPS) atmospheric model (Sutherland et al. 2020). As noted in the discussion section of (Sutherland et al. 2020) and references therein, this value can vary widely depending on the combination of ocean and atmospheric forcing, which implies that model uncertainty contributes significantly to the appropriate value here. The authors also note that explicitly including Stokes drift based on a wave prediction system is preferable over parameterization based on wind velocity.

The windage term used here could be optimized by deriving it for each ocean/atmospheric model combination using the procedure in (Sutherland et al. 2020). However, this is beyond the scope of this report: the focus is on improvements to the current forcing for drift simulations without evaluating the suitability of wind predictions in the port model domains for drift prediction or commenting on the potential utility of a port-scale wave prediction system. The windage parameterization used here is merely intended to provide a consistent, deterministic linkage between modelled currents, winds, and the motion of various drifter types. As considerable uncertainty is associated with this windage term, evaluation of surface currents against observations from ADCPs and current meters is deemed the primary determinant of model suitability for drift prediction, rather than analysis of observed and modelled drifter tracks.

Periods where drifters were active in the model domain are identified, and modelled trajectories are started every hour along the drift tracks. The benefits of starting drift tracks in this manner are to reduce the sensitivity to initial conditions and increase the number of tracks available. However, it means that some drift tracks are not independent and thus the errors may be correlated. Modelled trajectories were computed for a user-specified period of 24 hours or more, where possible. However, in some regions, the majority of the observed drifter tracks were less than 24 hours long, and here a shorter modelled trajectory length was chosen.

Observed drifter tracks were truncated to areas covered by the 'wet' cells of the port model domains to avoid launching virtual drifters in 'dry' parts of the domain where observed drifters are near the shoreline, which may not be precisely resolved. In addition, to facilitate interpolation of starting locations for virtual drifters, observed trajectories were split where time gaps between position records exceeded two hours. In the remaining portions, position records were interpolated to a consistent time interval ranging from five minutes to one hour.

For each model – observation pair of trajectories, two statistics are computed to assess the model performance. First is the separation distance, D, which is given by,

$$D(t) = |\dot{x_o}(t) - \dot{x_m}(t)|$$

Here $\dot{x_o}$ and $\dot{x_m}$ are the positions of the observed and modelled drifter, and || denotes the magnitude of the vector difference, i.e., the distance, between them.

Second is the instantaneous skill score, S, following (Molcard et al. 2009), which is given by

$$S(t) = \max\left(0, 1 - \frac{D(t)}{d_o(t)}\right)$$

Here $d_o(t)$ is the displacement of the observed drifter from the starting point of the pair. The rationale for the normalization by $d_o(t)$ is to increase the skill assigned to a trajectory prediction as the trajectory length increases, even if the separation distance remains constant. A separation distance of, for example, 500 m represents a less grievous error in a trajectory that is 10 km long than in one that is 500 m long. A value of S=1 indicates a perfect prediction.

4.2. FORECAST

The forecast evaluation involves running a set of forecasts (here 48 hours long, each starting at 00Z) and evaluating the performance over the independent forecasts as a function of lead time. Forecast evaluation was performed for a set of order 60 consecutive forecasts by comparing the model values with tide gauge, sea surface temperature and horizontal ADCP records. The set of forecasts were taken from winter 2021/22 for logistical reasons. Forecast performance was evaluated as the discrepancy (bias and CRMSE) with observed values as a function of forecast lead time. The error growth curves represent the discrepancy averaged over the set of evaluated forecasts, and we include 95% confidence intervals computed with a bootstrap method.

To detide the forecast and the corresponding hindcast water level series we subtract the tidal signal precalculated based on the hindcast covering the forecast evaluation period. The tidal signal is obtained with a T_TIDE fit with a Rayleigh number as low as 0.1 (overfitting) to ensure maximal energy removal at tidal frequencies. Such strong suppression of tidal energy was implemented to clear the error growth curves of any tidal residual, which otherwise would dominate the curve.

5. HINDCAST EVALUATION RESULTS

The STC500 hindcast covered the period 5-Feb-2016 to 31-Jan-2022 for a total of 2187 days. The STC100 hindcast covered the period 9-Feb-2016 to 30-Jan-2022 for a total of 2182 days. Evaluation was performed on observational data available during the simulation period and the results will be shown below for the two port models and CIOPS-E. Available observational data will be summarized in each of subsections below which are divided into instrument category.

5.1. WATER LEVEL

Modelled water level was validated by means of a single CHS water level station available in the model domain. The station (ID=00575) is located in Port Hawkesbury, Nova Scotia (45.6167°N, 61.3667°W; see location in Figure 8 inset) and provides hourly water level data extracted from the Canadian Tides and Water Levels Data Archive. The time series was shifted from chart datum to the CGVD28 as discussed in section 4.1.1. The CD-CGVD28 offset for this station was -0.884 m. Furthermore, the water level from the model was adjusted from the EGM-DIR-R4

datum inherited from CIOPS-E to CGVD28 by applying the constant offset of -0.622 m during analysis.

5.1.1. Mean sea surface height

The 2016-2021 mean sea surface height (ssh) map from STC500 is shown in Figure 6. The mean ssh varies from -0.42 to -0.35 m across the domain with a positive landward and along-shore gradient. The absolute scale of ssh is inherited from the vertical datum of the parent model and the map will serve as a means of converting the modelled elevation to CGVD28 datum. The elevation gradients reflect the steric height adjustment from the Nova Scotia Current (NSC; Drinkwater et al. 1979)), which is driven by the outflow of fresher/lighter water from the Gulf of Saint Lawrence (GSL).

5.1.2. Tidal water level

Table 2 presents a comparison of individual tidal constituents from the water level station and the three models for 2017. Only diurnal and semi-diurnal constituents were investigated, as this formed the dominant part of the tidal signal. M2 was the most dominant constituent with amplitude at just under 0.6 m. The next largest contributions were from N2 and S2 with amplitudes a fifth of M2, while K1, O1 and K2 a tenth of M2. P1 and Q1 had relatively minor contributions.

All models did well in constituent-wise comparison with amplitude errors generally under 0.01 m and phase errors less than six degrees. The total error which includes the combined effect of amplitude and phase (complex distance) was mostly under 0.01 m with the largest being 0.017 m for CIOPS-E M2. The port models tend to have smaller errors, this being most visible in M2 which dropped to 0.008 m for STC500 and to 0.004 m for STC100.

The year-to-year tidal performance was consistent as seen in the total tidal $CRMSE^2$ score (Figure 7). Hence tidal analysis results from other years are not shown but can be summarized as follows. Amplitudes fluctuations from year-to-year were <= 5 mm, occurring in both models and observation (largest fluctuation was for observed M2). Modelled M2 phases remained within 0.2 degrees, N2 and S2 within one degree. Phase modulation gradually increased with decreased constituent amplitude. O1, K1 and K2 fluctuated by a few degrees while P1 and Q1 by as much as 20 degrees. The large fluctuations of these minor constituent phases were however present in both observation and model, suggesting that the issue is related to resolution in tidal analysis rather than model performance.

Two historic tide gauges located inside the Strait of Canso (locations and other metadata included in Table 3) sufficiently long for analysis (>29 days) were available in the STC100 domain. To ensure the comparison is as objective as possible, tidal analysis was done on a series of equivalent length, and as the historic gauges' constituents were from a period before the hindcast analysis period, the start time for our analysis was taken on the first day of the same month as the gauges. For example, if the gauge analysis was done during June 1999, here we take the start as 1-Jun-2016. The available constituents, with amplitudes larger than 0.04 m, and corresponding constituents from tidal analysis of the modelled hindcasts are presented in Table 4. Overall, the agreement is similar to that from the long-term gauge (Table 2) but slightly worse. This is to be expected, as the analysis is based on fairly short periods with different start dates that might not have some constituents as accurately resolved as the previous analysis based on the yearlong series. No graphical representation was included here due to small number of stations.

5.1.3. Non-tidal water level

Figure 8 shows a yearlong time series of the observed and modelled, non-tidal water level and difference. Non-tidal skill scores are described in comparison to the tidal and total results in the following Section 5.1.4.

5.1.4. Overall scores

Water level scores for the Port Hawkesbury station are tabulated in Table 5 for the two resolutions of the port model as well as the parent model. Scores are presented per full year of available model data for the total water level as well as for the non-tidal and tidal contributions. Bias was small and ranged from -0.01 to 0.02 m over the five years. CRMSE ranged from 0.071 to 0.083 m for the total, 0.061 to 0.071 m for the non-tidal and 0.039 to 0.046 m for the tidal water level. Not shown here, but the direction of the CRMSE was in the underestimation of the non-tidal component by ~25% (see Figure 5 of DH22). PEARSONR scores were above 0.984 for the total, between 0.828 and 0.882 for the non-tidal and above 0.995 for the tidal, which clearly demonstrates that the tidal component was modelled better than the non-tidal. In addition, χ^2, which can be interpreted as percent of un-modelled variance, suggests that in STC100, there's <1% of room for improving the tides, while the non-tidal has 22-30%. However, as the tidal signal is larger than non-tidal (ratio of tidal to non-tidal variance was 12.4 in the observations), there is only about 2.2-2.8% of room for improvement in the total. Overall, the scores indicate a modest improvement of the port models over the parent, in particular for STC100, which consistently outperformed the others (more on this below).

Figure 7 summarizes model performance over the five years examined. The metric shown is the $CRMSE^2$ which represents the absolute unmodelled variance and has the property where tidal and non-tidal components add to give the total (hence bar graph is stacked). The figure shows that model performance is stable from year to with around 10% fluctuation. Non-tidal error accounted for around two-thirds of total $CRMSE^2$ indicating that this was the main source of errors. STC100 consistently outperformed the other two models by 10-20% in total $CRMSE^2$. Both tidal and non-tidal components contributed to the improvement in performance of the highest resolution model.

Figure 9 shows the power spectra of the observed and modelled water level from Port Hawkesbury. There is high agreement between all models and observation at low frequency. The tide and over-tide peaks are well modelled, although there’s a broad shoulder on the semi-diurnal peak that the models don’t reproduce. The seiche band (5-10 cpd) appears to be double peaked. A sharp peak appears at 5 cpd and a broader one 7-10 cpd. The second peak is the one identified by Barber and Taylor (1977), however the nature of the 5 cpd peak is unclear. The models reproduce both peaks as features but, the modelled power is only about 1/10 of the observed.

5.1.5. Storm surge water level

A total of six storms were chosen, one most significant for each year of the hindcast. Non-tidal water level scores for the storm period (included 2 days before and 2 after the peak), are shown in Table 6. CRMSE is slightly above the range of yearly tabulated scores described in Section 5.1.4, reaching 0.095 m for the Christmas storm. Only storm Teddy had CRMSE in the normal annual range, perhaps as this storm was fairly weak compared to the others. In general, a stronger signal will lead to larger CRMSE as DH22 found in a similar analysis performed season-wise. Additionally, the Christmas storm had χ^2 and PEARSONR scores within the normal annual range suggesting these normalized scores are more suitable here as the CRMSE largely reflects the intensity of the storm. With this in mind, only the Oct-23-2016 and

Nov-24-2021 storms had χ^2 and PEARSONR outside the annual range. The time series for storm are shown in Figure 10. There was a prominent seiche event during this storm which the models do not reproduce and is evidently the source of the large errors. The time series of the second poorly modelled storm also had high seiche activity. Overall, there was a modest improvement in the scores of higher resolution models.

5.2. WATER VELOCITY

5.2.1. Moored ADCPs

Seventeen ADCPs were available for evaluation. This collection was comprised from observations collected 2015-17 as part of the World Class Tanker Safety System (WCTSS) program. Additionally, three deployments were done 2018-19 for the OPP initiative. For locations and additional metadata refer to Drozdowski et al. (2018) for WCTSS and to Schillinger (2022) for OPP instruments. The entire collection was evaluated in terms of total, non-tidal and tidal scores at standard depths which models resolve (Table 7 - Table 9). Unresolved depths were left blank. Standard depths were chosen to represent the water column (10, 20, 30, 40, 50, 60, 70 m). For the purpose of further discussion and plots, the large collection was limited to a representative subset (highlighted in score Tables). From the WCTSS collection, this included the main strait (CM1_May2016; hereafter CM1) and strait entrance (CM7_May2016; hereafter CM7). From OPP, Chedabucto Bay (M2086), north flank of Canso Bank (M2087) and south flank (M2088). The latter two were on the Scotian Shelf and hence only STC500 and CIOPS-E evaluation was made there.

5.2.1.1. Scores

Overall total χ^2 scores were under 1.0 and improved with depth. CM7 was the best modelled of the representative stations with total current χ^2 = 0.75 for CIOPS-E, < 0.45 for STC500 and <0.38 for STC100. Total RMSE errors were ~0.07 m/s at CM1, 0.09-0.12 m/s at CM7, 0.09-0.14 m/s at M2086, and 0.11-0.21 m/s for M2087 and M2088. The gradual offshore increase in RMSE reflects the progressively stronger currents.

5.2.1.2. Vertical profiles

Profiles of the mean total current are shown in Figure 11 and Figure 12 for the outer stations (M2087 and M2088). There is southwesterly flow of around 0.1 m/s. At M2087 the mean flow is reasonably well reproduced by both models but t M2088 it is underestimated by both models but more so by STC500. Also, the direction of mean flow is off by ~20° in STC500 and ~30° in CIOPS-E. The stations inside the embayment area (inner) had negligible mean currents and are omitted.

Figure 13 to Figure 17 show the vector correlation profiles for the five representative stations. For CM1, correlations were 0.4 to 0.6 with angles close to zero. STC100 consistently outperformed STC500 by 0.05-0.1. There was very little difference between the total and non-tidal, reflecting the weak barotropic tides here and dominance of non-tidal flow. Correlations at CM7 are high (~0.8) for the port models while CIOPS-E underperforms due to poor resolution. At this station, the tides in the total current comparison add between 0.1 and 0.5 to the non-tidal solution indicating the more significant role played by the tides here particularly at 12-16 m depth. At M2086 the correlations were somewhat poor near the surface (~0.4), but gradually increase to reasonable values of ~0.65 near the bottom. The influence of tides is weak here as indicated by the similarity between total and non-tidal scores. At M2087 and M2088 total (non-tidal) current correlations were generally 0.6 to 0.7 (0.5 to 0.6).

Figure 18 to Figure 24 show the elliptic tidal constituent profiles. Only largest (M2) constituent is shown (other constituents are small) for CM1, CM7 and M2086. For M2087 and M2088 both M2 and K1 are included as both are large. At CM1, the M2 major amplitude is ~0.03 m/s and slightly overestimated by the models. Phases change from surface to bottom by ~50 degrees, indicative of internal tides. The phase variation was partially modelled by STC100. At CM7 major axis amplitude increases to 0.15 m/s and is well modelled by STC100. STC500 performed well near the surface but degraded towards the bottom, while CIOPS-E performed poorly. At this station the 50 degree surface to bottom phase variation was also present, and well modelled by both port models. At M2086, the major axis M2 amplitude is ~0.05 m/s and are overall well modelled by all models except CIOPS-E performance degraded near the bottom. At M2087 and M2088 both M2 and K1 major axis amplitudes are 0.03-0.09 m/s and modeled reasonably well by both models.

5.2.1.3. Time series and rotary spectra

Time series showing approximately 1.5 months of the near-surface (10 m), non-tidal currents at each of the five representative stations are shown in Figure 25 to Figure 29. For the inner stations, the port models improve over CIOPS-E, particularly at CM7 where they effectively model many of the large inflow/outflow events. For the outer stations, both STC500 and CIOPS-E resolve much of the observed variability equally well. Rotary spectra of the non-tidal currents are shown in Figure 30 to Figure 34. The clockwise and counterclockwise spectra are very similar, and no indication of inertial oscillations is visible. Overall, the models have lower than observed power levels, particularly at higher frequencies. For the inner stations the port model power levels were closer to the observed levels than CIOPS-E at all frequencies. For the outer stations, STC500 had a better representation of the power at high frequencies but performed equally with CIOPS-E at low frequency.

5.3. WATER PROPERTIES

5.3.1. Sea surface temperature

Here we present model comparison with observations of surface recording thermographs. Two-year-long time series were available from two marine weather stations in Chedabucto Bay, east (44488) and west (44489). Time series and distribution comparisons are shown in Figure 35 and Figure 36. The plots also show the mooring locations. All models reproduced the two seasonal cycles over the observation period as well the observed temperature distribution. Largest errors tended to be in the summer months where more upwelling/downwelling variability was present and the models underestimated the peak temperatures. Errors reach 5 ^{o}C, but are generally within 1 ^{o}C. This is summarized in Table 10, where a slight (<0.5 ^{o}C) bias is present and CRMSE error is around 1 ^{o}C. χ^2 is close to zero and PEARSONR to one, reflecting the high agreement in capturing the seasonal cycle. Port models show a modest improvement over CIOPS-E in the scores.

5.3.2. Moored CTDs

Here we present model comparison with observations of T-S recorded by moored CTDs. Data was available from two locations (shown in figures; for addition metadata refer to DH22), one of which was in Chedabucto Bay (CB_10m and CB_48m) moored at 48 and 10 m. The other instrument was near the causeway in the strait (CW_55m) but as CIOPS-E does not resolve the location at all and STC500 was too shallow at the location for the analysis to extract a time series, hence only results from STC100 are shown.

At CB_10m (Figure 37) the temperature has similar features to the nearby SST observations discussed above, but as the series is shorter, the underestimation of peak summer temperatures is more apparent. The salinity at CB_10m had a seasonal cycle reaching its highest point in spring at around 31 PSU and dropping to 29.5 PSU in the fall. The models reproduce the seasonal cycle and many of the fluctuations, but there is an overall salty bias of 0.4 PSU (see Table 10) which was as large as 1 PSU during the fall salinity low. The models did capture much of the covariance of the salinity signal though, which was reflect in low χ^2 (~0.19) and high PEARSONR (~0.91). There was no improvement for the port models over CIOPS-E here.

At CB_48m (Figure 38), the near-bottom record, temperature had a seasonal cycle similar to the near-surface record but lagging by a few months and slightly cooler. Synoptic fluctuations were prominent during the summer and fall. The models do a good job reproducing the seasonal cycle and fluctuations with 0.1-0.12 χ^2 and 0.94-0.95 PEARSONR. Also, there is a small improvement over CIOPS-E at this location. The near-bottom salinity was dominated by synoptic fluctuations which were well modelled with 0.17-0.4 χ^2 and 0.78-0.91 PEARSONR. The improvement in the port models is significant here with χ^2 dropping by more than half between the CIOPS-E and STC100.

5.3.3. CTD profiles

In this section we discuss model comparisons with available CTD profiles. The comparison includes the WCTSS CTD collection of 22 casts (14 inside the Strait of Canso and 8 outside; see DH22) as well as additional casts available in the outer region during the hindcast period (~70) which were made mostly on easter Scotian Shelf in the domain of STC500. The WCTSS CTD collection occurred mainly in the months of May and November while outer casts were collected between May and November with the bulk in July and August. A map of cast locations and regions used in analysis below in shown in Figure 40.

Results are summarized with profiles of T-S bias ± CRMSE taken over all the CTDs available in each of the two regions in Figure 41 and Figure 42. The first region corresponds to the inner port area and corresponds to the domain of STC100, which includes a smaller number of casts mostly inside the strait, while the second to STC500 less the STC100 domain (i.e., outer region only). The figure also includes the total number of observations at each depth, which tended to decrease with depth.

In the inner region, all models had ~0.5 ^{o}C warm bias through out water column (no observations below 60 m). The port model salinity had a salty bias of 0.5 PSU which decreases with depth. CRMSE was around 0.5 ^{o}C and 0.25 PSU. CIOPS-E was not considered in this region as it does not resolve the strait.

For the outer regions, temperature had a cold bias of 0.8 ^{o}C in the top 10 m, which reversed to a warm bias of the same magnitude at around 100 m and continued increasing at depth but the statistics below 200 m becomes unreliable as the number of samples becomes small. The salty bias in this region was also present but here reached a maximum of 0.75 PSU at around 15 m and then decreased to zero at around 200 m. The subsequent increase below 200 m is statistically unreliable. The CRMSE was larger in the outer region, reaching a maximum of around 2 ^{o}C and 0.75 PSU. Both STC500 and CIOPS-E produced very similar results.

5.4. DRIFT

Sixteen CODE/DAVIS surface drift tracks where available for drift analysis. They were all located on the Scotian Shelf (Figure 43) and hence only STC500 and CIOPS-E were able to be evaluated. The tracks were multi-day long and afforded ample 24-hour segments allowing for

reliable calculation of mean scores. A standard literature windage of 1.36% was applied to the drift tracking (Sutherland et al. 2020). Figure 44 shows the mean Molcard score (over all available 24-hour segments) as a function of drift time, while Figure 45 shows the mean separation distance. The STC500 skill peaks at just under 0.4 at 10 hours for STC100, while CIOPS-E performs somewhat poorer starting at 0.35 and degrading after. The standard deviation envelope on the score is quite wide (~0.6) indicating a large variation in skill for individual 24-hour segments. The mean separation distance increases linearly to maximum value of 10 (8) km for CIOPS-E (STC500). Hourly Molcard skill and separation distance is included in Table 11.

6. FORECAST EVALUATION RESULTS

The forecast evaluation was performed during the period 27-Nov-2021 to 27-Jan-2022. Only water level (Port Hawkesbury gauge) data was available for evaluation during this period.

6.1. NON-TIDAL WATER LEVEL

Figure 46 shows the growth of average non-tidal error (bias and CRMSE) during the 48-hour forecast period. Given these statistics were calculated from a relatively small samples size of 60 forecasts, a shaded envelope is included to show the 95% confidence limits based on the boot-strap method. The bias fluctuates in the -0.08 to 0.03 m range with what appears to be a five-hour period. The proximity of the feature to the seiche band suggest a possible connection. However, it is unclear what the generation mechanism would be. Additionally, the connection is unlikely as averaging 60 forecasts would tend to average out non-coherent fluctuations. The CRMSE stays between 0.05 and 0.12 m, with a small trend, consistent with forecast error growing with time. These errors are slightly larger than the annual scores reported in Table 5, but are reasonable given the small sample size and forecast error present here.

7. SUMMARY

Available observational data which including water level gauges, multilevel (ADCP) current meters, weather-buoy based SST, moored CTD, CTD casts and surface drifter data were used to evaluate port scale models of the Strait of Canso. The evaluation was done by comparing model performance scores, time series and tidal constituents where applicable (see Section 4), of each of the two port models and CIOPS-E (where available). A 2016-2021 model hindcast, downscaled from the Coastal Ice-Ocean Prediction Systems East (CIOPS-E), was used for this purpose. Furthermore, for water level, the evaluation included a check of stability over 5 years of hindcast, evaluation of scores during large historic storm periods, and a forecast lead hour investigation (using a ~60 00Z forecasts). Model performance was summarized, with focus placed on identifying improvements in finer scale models, as well as identifying model limitations.

One long-term water level station (Port Hawkesbury) was available for evaluation. At this station, all models performed well in terms of water level scores, with total CRMSE 0.071 to 0.083 m. About 1/3 of this score was attributed to tides while the remaining 2/3 to the non-tidal component. Examining five years of this score (computed yearly) revealed only about 10% of fluctuation in this score, demonstrating model stability (Figure 7). Additionally, tides were modelled much better than the non-tidal part, with tidal χ^2 score (here % of un-modelled variance) of < 1%, while the non-tidal had 22-30%. However, as the tidal signal is larger than non-tidal (ratio of tidal to non-tidal variance was 12.4 in the observations), there is only 2.2-2.8% of unmodelled variance in the total score. Overall, the scores indicate a significant improvement of the port models over the parent, in particular for STC100, which consistently outperformed

the others by 10-20% in terms of CRMSE. The excellent tidal performance was also reflected in small (< 0.01 m) tidal error based on constituents from tidal analysis (Table 2). The water level performance findings at the Port Hawkesbury station can be generalized to the whole port model domain, which is small (STC500 is ~150 x 150 km). For instance, M2 has only 0.1 m variation in amplitude and a few degrees in phase over the STC500 domain (WEBTIDE; Dupont et al. 2002). Tidal performance was also checked at two historic gauge stations inside the Strait of Canso and found to be reasonably consistent with above findings.

Six storms were analyzed during the hindcast period by comparing scores during a four-day storm window to the annual scores. The storm CRMSE scores were generally above the annual range, but this was attributed to higher overall variance during the storm period. A normalized score proved to be more appropriate; χ^2 was in the normal range for all but two of the storms. The two outliers were attributed to unresolved seiching (Barber and Taylor, 1977) which was particularly active during these storms (e.g., Figure 10). Furthermore, spectral analysis found all models to lack high frequency energy, particularly in the seiche band (5-10 cpd).

Water level forecast evaluation was performed during the period 27-Nov-2021 to 27-Jan-2022 for the Port Hawkesbury gauge. The bias fluctuates in the -0.08 to 0.03 m range with what appears to be a five-hour period. The CRMSE stays between 0.05 and 0.12 m, with a small trend, consistent with forecast error growing with time. These errors are slightly larger than those reported annually in Table 5, but are reasonable given the small sample size and forecast error present here.

A collection of seventeen ADCP current meters was available for evaluation. Scores from all were presented in Table 7 to Table 9, but discussion was limited to a representative subset of five (three inside the embayment and two on the open shelf) at standard depths (see Section 5.2.1). Overall total χ^2 scores were under 1.0. For the embayment stations, scores improved with depth and model resolution (particularly where topographic steering is present). In particular, the station in the entrance to the strait (CM7) which is the most energetic station in the embayment, as well highly constrained by topography, was also the best modelled with total current χ^2 = 0.75 for CIOPS-E, < 0.45 for STC500 and < 0.38 for STC100. A time series of the non-tidal current from this station (Figure 26), shows how port models (in particular STC100) was able to effectively model much of the variability in the flow field and improve over CIOPS-E.

A large improvement of ADCP scores with depth was seen at M2086 where for STC500, total χ^2 went from 0.97 near the surface to 0.62 near the bottom (70 m). On the open shelf, scores tended to worsen near the surface and near the bottom, suggesting inadequate resolution of those boundary layers. Additionally, improvement of STC500 over CIOPS-E was not evident in the open shelf scores.

Mean flow inside the embayment area was negligible, but on the open shelf a southwest mean current, associated with the Nova Scotia Current (Drinkwater et al. 1979) of 0.1 m/s was well modelled by both STC500 and CIOPS-E.

From tidal current constituent evaluation, it was found that in the main part of the Strait of Canso, the barotropic tide is weak (M2 current amplitudes ~ 0.03 m/s; other constituent negligible), while in the entrance to the strait, M2 current amplitude increases to 0.15 m/s. A 50 degree phase difference, associated with internal tides (DJ20; DH22) is present throughout. These features were well modelled by STC100 (RMSE for all resolved tidal constituents 0.014-0.024 m/s), modestly well by STC500 (RMSE 0.021- 0.053 m/s), and poorly (unresolved) by CIOPS-E. In Chedabucto Bay, M2 amplitudes drop to ~ 0.05 m/s and were well modelled by all models (RMSE 0.018-0.035 m/s) with the port models offering a small improvement near the bottom. On the open shelf, K1 is as important as M2 (current amplitudes 0.03 to 0.09 m/s), and both were well modelled (RMSE 0.26-0.053 m/s).

Rotary spectra at the five representative stations showed no indication of inertial oscillations or any other Coriolis type asymmetry between clockwise and counterclockwise spectra. Overall, the models have lower than observed power levels, particularly at higher frequencies. For the inner stations the port model power levels were closer to the observed levels than CIOPS-E at all frequencies. For the outer stations, STC500 had a better representation of the power at high frequencies but performed equally with CIOPS-E at low frequency.

Currents on the open shelf were also evaluated with drift analysis of sixteen available CODE/DAVIS surface drifters (Section 5.4). The STC500 Molcard skill peaks at just under 0.4 at 10 hours for STC100, while CIOPS-E performs somewhat poorer starting at 0.35 and degrading after. The variation in skill of individual 24-hour drift segments was large with STD ~ 0.3. For context, the Molcard score by design suggest any value above zero implies the model has some skill (compared to persisting initial release position). Additionally, the scores here fall in the range of (Paquin et al. 2020) who report Molcard scores in the range of 0.2 to 0.6, although the range included scores from windage sensitivity analysis and hence the lower scores represent inappropriate values such as 3% for the CODE/DAVIS drifter. Additionally, their study area was the Bay of Fundy, a strong tidally driven flow, compared to mostly wind driven and residual flow here, weakening the analogy between the two studies. Perhaps more useful (from dominant flow perspective) is the evaluation presented by (Soontiens and Holden 2022) which looked at CIOPS-E and it's parent models in the non tidal Flemish Cap region of the North West Atlantic. They found Molcard scores of 0.2-0.25 and CIOPS-E did not outperform the parent models until unconstrained scale features were removed by spatial filtering.

Multiyear time series of SST were available from two marine weather stations in Chedabucto Bay. The seasonal SST cycle was well modelled by all three models (e.g., Figure 35). The CRMSE error was around 1 ^{o}C, with the largest point errors associated with upwelling/downwelling variability during summer and fall. The port models demonstrated only a very modest improvement over CIOPS-E.

Observations of T-S recorded by moored CTDs were available in Chedabucto Bay (CB) and inside the strait towards the causeway (CW; see Section 5.3.2). Near the surface, the temperature evaluation was comparable to SST above. Salinity at had a seasonal cycle reaching its highest point in spring at around 31 PSU and dropping to 29.5 PSU in the fall. This is the salinity low signal associated with the outflow from the Gulf of Saint Lawrence (Drinkwater et al. 1979; Petrie et al. 1996). The models reproduce the seasonal cycle and many of the fluctuations (χ^2 ~ 0.19), but there is an overall salty bias of 0.4 PSU (1 PSU during the salinity low).

There was no improvement for the port models over CIOPS-E here.

At CB, the near-bottom temperature had a seasonal cycle similar to that of the near-surface temperature but lagging by a few months and slightly cooler. Synoptic fluctuation associated with upwelling and downwelling were prominent during the summer and fall. All models did a reasonable job reproducing these features (χ^2 between 0.1-0.12) with the port models improving slightly over CIOPS-E. The near-bottom salinity was dominated by synoptic fluctuations which were well modelled with χ^2 varying from 0.17 to 0.4. The improvement in the port model's salinity scores was more pronounced than for temperature with χ^2 dropping by more than half between the CIOPS-E and STC100. The near-bottom T-S improvement in the port models is expected, as they do a better job resolving the bathymetry which is a strong driver of near-bottom circulation.

The CW station was included in the evaluation for demonstration of the port model's ability to model deep water intrusion into the strait, first identified by DH22. Intrusions are characterized by sudden shift in T-S properties corresponding to the displacement of stagnant water with

water beyond the sill (Farmer and Freeland 1983). Five such events were identified in the observations and three of those were capture by STC100 (Figure 39). In particular, the largest event at the end of October was particularly well reproduced with salinity (temperature) increasing (decreasing) by 1 PSU (5 ^{o}C). These features were unresolved (poorly resolved) by CIOPS-E (STC500).

A collection of ~ 90 CTD casts was available for evaluation (Section 5.3.3). The evaluation was divided into the inner (STC100 domain) and outer region (STC500 excluding STC100). The inner region had few casts, and these were mostly inside the strait. In the inner region, the port models had ~0.5 ^{o}C warm bias through out the water (no observations below 60 m). In addition, a salty bias of 0.5 PSU (same feature noted above in near-surface salinity time series) was present which decreased with depth.

For the outer evaluation region, temperature had a cold bias of 0.8 ^{o}C in the top 10 m, which reversed to a warm bias of the same magnitude at around 100 m. The salty bias in this region was also present but here reached a maximum of 0.75 PSU at around 15 m and then decreased to zero at around 200 m. Both STC500 and CIOPS-E produced very similar results. This is not unexpected as the region is a through flow area for the Nova Scotia current (NSC; Drinkwater et al. 1979), which brings fresher water from the Gulf of Saint Lawrence. The persistence of the salty bias suggest it is inherited from the parent model. The findings also suggest that source of the warm bias in the inner region (this feature was more pronounced further inshore in the analysis of DH22) is warm offshore bias of the bottom layer, which invades the coastal regions through Ekman upwelling near topographic boundaries (Petrie et al. 1987).

8. KEY FINDINGS

- The Strait of Canso is currently unresolved by any operational models. The port models evaluated here are the first to do so.
- All models performed very well in terms of total water level scores but STC100, consistently outperformed the others by 10-20% in terms of total water level CRMSE.
- Examining five years of CRMSE (computed yearly) revealed only about 10% of fluctuation, demonstrating model stability.
- The models ran successfully during six storms analyzed. Scores were reasonable during the storms for all but two storms which had somewhat higher errors due to unresolved seiching. The mechanism causing the error is unknown. No improvement over parent model.
- Water level forecast evaluation revealed that the port models performed reasonably well but no improvement over CIOPS-E.
- For the inshore ADCP stations, scores improved with depth and model resolution, particularly where topographic steering is present.
- On the open shelf, ADCP scores tended to worsen near the surface and near the bottom, suggesting inadequate resolution of those boundary layers. Additionally, no clear improvement of STC500 over CIOPS-E.
- On the open shelf a southwest mean current, associated with the Nova Scotia Current of 0.1 m/s was well modelled by both STC500 and CIOPS-E. no clear improvement of STC500 over CIOPS-E.
- Tidal currents inside the Strait of Canso (and near the entrance) were well modelled by the port models but unresolved (or poorly modelled) by CIOPS-E.

- Drifter analysis revealed a slight improvement of STC500 over CIOPS-E in terms of the Molcard skill. However, these results pertain only to open shelf due to lack of drifter data inside the port region.
- In Chedabucto Bay, the seasonal SST cycle was well modelled by all three models. No clear improvement over CIOPS-E.
- SSS followed the correct seasonal cycle but there was 0.4 PSU salty bias persisting in all three models. No clear improvement over CIOPS-E.
- Near-bottom temperature and salinity were well modelled in terms of the seasonal cycle and fluctuations. Port models improve over CIOPS-E, particularly for salinity.
- STC100 was able to model deep water intrusion/renewal over the sill with reasonable skill. This feature was not modelled/resolved by CIOPS-E.
- Inshore CTD profiles were well modelled by the port models but unresolved by CIOPS-E.
- No clear improvement over CIOPS-E was seen in the offshore CTD profiles.

9. ACKNOWLEDGEMENTS

The initial development of the NEMO based Strait of Canso models was facilitated by contributions from Li Zhai and Xianmin Hu. Field data collection was and continues to be critical to the success of this project. The authors extend gratitude to Doug Schillinger and Ed Horne who were and continue to be instrumental in the data collection effort. Drift analysis code (and guidance through the drift analysis process) was provided by Nancy Soontiens and Jennifer Holden. Helpful guidance was offered by many DFO managers involved in this project, in particular Joël Chassé and Youyu Lu. We thank the ACOM committee and CSAS reps. for their helpful reviews towards improving this manuscript. Gratitude is extended to numerous other individuals in DFO, ECCC and SSC, without who's contributions these modelling systems would not be where they are. This work was supported by Canada's Ocean Protection Plan.

10. REFERENCES CITED

Atkinson, David E, Donald L Forbes, Thomas S James, Nicole J Couture, and Gavin K Manson. 2016. “DYNAMIC COASTS IN A CHANGING CLIMATE,” 27–68.

Backhaus, Jan O. 1983. “A Semi-Implicit Scheme for the Shallow Water Equations for Application to Shelf Sea Modelling.” Continental Shelf Research 2 (4): 243–54. https://doi.org/10.1016/0278-4343(82)90020-6.

———. 1985. “A Three-Dimensional Model for the Simulation of Shelf Sea Dynamics.” Deutsche Hydrographische Zeitschrift 38 (4): 165–87. https://doi.org/10.1007/BF02328975.

Barber, F. G., and J. Taylor. 1977. “A Note on Free Oscillations of Chedabucto Bay.” https://waves-vagues.dfo-mpo.gc.ca/Library/53791.pdf.

Blanken, Hauke, Caterina Valeo, Charles Hannah, Usman T. Khan, and Tamás Juhász. 2021. “A Fuzzy-Based Framework for Assessing Uncertainty in Drift Prediction Using Observed Currents and Winds.” Frontiers in Marine Science 8 (November): 618094. https://doi.org/10.3389/fmars.2021.618094.

Bugden, Gary, B. A. Law, Edward P. W. Horne, and Shawn E. Roach. 2020. “Flow through the Canso Causeway.” https://waves-vagues.dfo-mpo.gc.ca/Library/40884533.pdf.

Chen, Changsheng, Hedong Liu, and Robert C. Beardsley. 2003. “An Unstructured Grid, Finite-Volume, Three-Dimensional, Primitive Equations Ocean Model: Application to Coastal Ocean and Estuaries.” Journal of Atmospheric and Oceanic Technology 20 (1): 159–86. https://doi.org/10.1175/1520-0426(2003)020<0159:AUGFVT>2.0.CO;2.

Cummins, Patrick F., and Lie-Yauw Oey. 1997. “Simulation of Barotropic and Baroclinic Tides off Northern British Columbia.” Journal of Physical Oceanography 27 (5): 762–81. https://doi.org/10.1175/1520-0485(1997)027<0762:SOBABT>2.0.CO;2.

Cummins, Patrick F., and Pramod Thupaki. 2018. “A Note on Evaluating Model Tidal Currents against Observations.” Continental Shelf Research 152 (January): 35–37. https://doi.org/10.1016/j.csr.2017.10.007.

Daniel, Pierre, Gwénaële Jan, Fanch Cabioc’h, Yves Landau, and Erwann Loiseau. 2002. “Drift Modeling of Cargo Containers.” Spill Science & Technology Bulletin 7 (5–6): 279–88. https://doi.org/10.1016/S1353-2561(02)00075-0.

Drakkar Group. 2007. “Eddy-Permitting Ocean Circulation Hindcasts of Past Decades.” *Clivar Exchanges* 42 (12 (3)): 8–10.

Drinkwater, K., B. Petrie, and W. H. Jr Sutcliffe. 1979. “Seasonal Geostrophic Volume Transports along the Scotian Shelf.” *Estuarine and Coastal Marine Science* 9 (1): 17–27.

Drozdowski, A., and E. Horne. 2022. “Strait of Canso Port Model Hindcast Evaluation.” https://waves-vagues.dfo-mpo.gc.ca/library-bibliotheque/41073095.pdf.

Drozdowski, A., E. Horne, and F. Page. 2018. “Seasonal Current Statistics and Tidal Constituents from Canso Strait and Eastern Nova Scotia.” https://waves-vagues.dfo-mpo.gc.ca/Library/4073495x.pdf.

Drozdowski, A., and D. Jiang. 2020. “Modelling Internal Tides in the Strait of Canso.” *Atmosphere-Ocean*, 1–18. https://doi.org/10.1080/07055900.2020.1744511.

Dupont, F, CG Hannah, DA Greenberg, JY Cherniawsky, and CE Naimie. 2002. “Modelling System for Tides for the Northwest Atlantic Coastal Ocean.” *Can. Tech. Rep. Hydrogr. Ocean. Sci. Department of Fisheries and Oceans* 221. http://www.dfo-mpo.gc.ca/Library/265855.pdf.

Dupont, F., S. Higginson, R. Bourdallé-Badie, Y. Lu, F. Roy, G. C. Smith, J.-F. Lemieux, G. Garric, and F. Davidson. 2015. “A High-Resolution Ocean and Sea-Ice Modelling System for the Arctic and North Atlantic Oceans.” Geoscientific Model Development 8 (5): 1577–94. https://doi.org/10.5194/gmd-8-1577-2015.

Farmer, David M, and Howard J Freeland. 1983. “The Physical Oceanography of Fjords.” *Progress in Oceanography* 12 (2): 147–219.

Flather, RA. 1976. “A Tidal Model of the North-West European Continental Shelf.” *Mem Soc R Sci Liege* 10(6): 141–64.

Gregory, D. 1993. “Oceanographic, Geographic and Hydrological Parameters of Scotia-Fundy and Southern Gulf of St. Lawrence Inlets.” *Can. Tech. Rep. Hydrogr. Ocean. Sci.* No. 143: viii + 248 pp. https://waves-vagues.dfo-mpo.gc.ca/Library/143396.pdf.

Hourston, Roy A.S. 2021. Surface Ocean Circulation Tracking Drifter Data from the Northeastern Pacific and Western Arctic Oceans, 2014-2020. Sidney, B.C.: Fisheries and Oceans Canada - Pêches et Océans Canada.

Kundu, Pijush K. 1976. “Ekman Veering Observed near the Ocean Bottom.” Journal of Physical Oceanography 6 (2): 238–42. https://doi.org/10.1175/1520-0485(1976)006<0238:EVONTO>2.0.CO;2.

Large, William George, and Stephen G. Yeager. 2004. “Diurnal to Decadal Global Forcing for Ocean and Sea-Ice Models: The Data Sets and Flux Climatologies.” NCAR Technical Note NCAR/TN-460+STR. Boulder, CO: Climate and Global Dynamics Division: National Center for Atmospheric Research.

Levier, B, AM Tréguier, G Madec, and V Garnier. 2007. “Free Surface and Variable Volume in the NEMO Code.” *MERSEA IP Report WP09-CNRS-STR03-1A*. https://zenodo.org/record/3244182/files/NEMO_vvl_report.pdf.

Madec, Gurvan. 2016. NEMO Ocean Engine. Note Du Pole de Modélisation de l’Institut Pierre-Simon Laplace 27. NEMO European Consortium.

Milbrandt, Jason A., Stéphane Bélair, Manon Faucher, Marcel Vallée, Marco L. Carrera, and Anna Glazer. 2016. “The Pan-Canadian High Resolution (2.5 Km) Deterministic Prediction System.” Weather and Forecasting 31 (6): 1791–1816. https://doi.org/10.1175/WAF-D-16-0035.1.

Molcard, A., P.M. Poulain, P. Forget, A. Griffa, Y. Barbin, J. Gaggelli, J.C. De Maistre, and M. Rixen. 2009. “Comparison between VHF Radar Observations and Data from Drifter Clusters in the Gulf of La Spezia (Mediterranean Sea).” Journal of Marine Systems 78 (November): S79–89. https://doi.org/10.1016/j.jmarsys.2009.01.012.

Niiler, Pearn P., Andrew S. Sybrandy, Kenong Bi, Pierre M. Poulain, and David Bitterman. 1995. “Measurements of the Water-Following Capability of Holey-Sock and TRISTAR Drifters.” Deep Sea Research Part I: Oceanographic Research Papers 42 (11–12): 1951–64. https://doi.org/10.1016/0967-0637(95)00076-3.

Nudds, Shannon, Youyu Lu, Simon Higginson, Susan P. Haigh, Jean-Philippe Paquin, Mitchell O’Flaherty-Sproul, Stephanne Taylor, et al. 2020. “Evaluation of Structured and Unstructured Models for Application in Operational Ocean Forecasting in Nearshore Waters.” Journal of Marine Science and Engineering 8 (7): 484. https://doi.org/10.3390/jmse8070484.

Paquin, Jean-Philippe, Youyu Lu, Stephanne Taylor, Hauke Blanken, Guillaume Marcotte, Xianmin Hu, Li Zhai, et al. 2020. “High-Resolution Modelling of a Coastal Harbour in the Presence of Strong Tides and Significant River Runoff.” *Ocean Dynamics* 70: 365–85.

Paquin, Jean-Philippe, François Roy, Gregory C. Smith, Frédéric Dupont, Sarah MacDermid, Yukie Hata, Oleksandr Huizy, Ji Lei, Yosvany Martinez, Hauke Blanken, Jennifer Holden, Nancy Soontiens. 2021a. "Coastal Ice Ocean Prediction System for the East Coast of Canada (CIOPS-E): Update from version 1.50 to 2.0.0." Canadian Centre for Meteorological and Environmental Prediction Tech. Note. https://collaboration.cmc.ec.gc.ca/cmc/cmoi/product_guide/docs/tech_notes/technote_ciops-east-200_e.pdf.

Paquin, Jean-Phillipe, Gregory C. Smith, Frederic Dupont, Sarah MacDermid, Yukie Hata, Oleksandr Huizy, Ji Lei, Yosvany Martinez, Michael Dunphy, Maxim Krassovski, Stephanne Taylor, Hauke Blanken, Jennifer Holden, Nancy Soontiens, Susan E. Allen, and Doug Latornell. 2021b. “Coastal Ice Ocean Prediction System for the West Coast of Canada (CIOPS-W): Update from version 1.5.0 to 2.0.0.” Canadian Centre for Meteorological and Environmental Prediction Tech. Note. https://collaboration.cmc.ec.gc.ca/cmc/cmoi/product_guide/docs/tech_notes/technote_ciops-west-200_e.pdf.

Paquin, Jean-Phillipe, Gregory C. Smith, Francois Roy, Frederic Dupont, Sarah MacDermid, Ji Lei, Youyu Lu, Stephanne Taylor, Hauke Blanken, and Li Zhai. 2022. “Coastal Ice Ocean Prediction System for the West Coast of Canada (CIOPS-W): System Description for Versions 1.0.0 and 1.5.0.” Canadian Centre for Meteorological and Environmental Prediction Tech. Note. https://collaboration.cmc.ec.gc.ca/cmc/cmoi/product_guide/docs/tech_notes/technote_ciops-west-100_e.pdf.

Petrie, B., K. Drinkwater, D. Gregory, R. Pettipas, and A. Sandstrom. 1996. “Temperature and Salinity Atlas for the Scotian Shelf and the Gulf of Maine.” https://waves-vagues.dfo-mpo.gc.ca/Library/193505.pdf.

Petrie, B., B. Topliss, and D. Wright. 1987. “Coastal Upwelling and Eddy Development off Nova Scotia.” *Journal of Geophysical Research* 29: 12979–91.

Petrie, Brian. 2022. “Sydney Harbour: Seiches, Tides and Mean Circulation.” *Proceedings of the Nova Scotian Institute of Science (NSIS)* 52 (2): 225.

Röhrs, Johannes, and Kai H. Christensen. 2015. “Drift in the Uppermost Part of the Ocean.” Geophysical Research Letters 42 (23). https://doi.org/10.1002/2015GL066733.

Röhrs, Johannes, Kai Håkon Christensen, Lars Robert Hole, Göran Broström, Magnus Drivdal, and Svein Sundby. 2012. “Observation-Based Evaluation of Surface Wave Effects on Currents and Trajectory Forecasts.” Ocean Dynamics 62 (10–12): 1519–33. https://doi.org/10.1007/s10236-012-0576-y.

Saucier, François J. 2003. “Modeling the Formation and Circulation Processes of Water Masses and Sea Ice in the Gulf of St. Lawrence, Canada.” Journal of Geophysical Research 108 (C8): 3269. https://doi.org/10.1029/2000JC000686.

Saucier, François J., and Joël Chassé. 2000. “Tidal Circulation and Buoyancy Effects in the St. Lawrence Estuary.” Atmosphere-Ocean 38 (4): 505–56. https://doi.org/10.1080/07055900.2000.9649658.

Schillinger, Douglas J. 2022. “ADCP and Drifter Measurements on a Shallow Plateau (80m Depth) on the Eastern Scotian Shelf: 1 November 2018 - 27 March 2019.” https://waves-vagues.dfo-mpo.gc.ca/library-bibliotheque/41081833.pdf.

Smith, Stuart D. 1988. “Coefficients for Sea Surface Wind Stress, Heat Flux, and Wind Profiles as a Function of Wind Speed and Temperature.” Journal of Geophysical Research 93 (C12): 15467. https://doi.org/10.1029/JC093iC12p15467.

Soontiens, N., and J. Holden. 2022. “The Impact of Ocean Model Resolution on the Accuracy of Drift Predictions.” Presented at the 56th Annual Canadian Meteorological and Oceanographic Society Congress, Virtual, June.

Soontiens, Nancy, and Jennifer Holden J. 2024. "A framework for evaluation and characterization of drift prediction in the marine environment." Can. Tech. Rep. Hydrogr. Ocean Sci. 383: ix + 45 p. https://waves-vagues.dfo-mpo.gc.ca/library-bibliotheque/41252287.pdf.

Sutherland, Graig, Nancy Soontiens, Fraser Davidson, Gregory C. Smith, Natacha Bernier, Hauke Blanken, Douglas Schillinger, et al. 2020. “Evaluating the Leeway Coefficient of Ocean Drifters Using Operational Marine Environmental Prediction Systems.” *Journal of Atmospheric and Oceanic Technology* 37 (11): 1943–54. https://doi.org/10.1175/JTECH-D-20-0013.1.

Zhang, Minghong, William Perrie, and Zhenxia Long. 2019. “Springtime North Pacific Oscillation and Summer Sea Ice in the Beaufort Sea.” Climate Dynamics 53 (1–2): 671–86. https://doi.org/10.1007/s00382-019-04627-1.

11. TABLES

Table 1. Key model setup parameters.

Parameter	Outer grid (STC500)	Inner grid (STC100)
Grid dimensions, NX × NY × NZ	379 × 374 × 47	714 × 479 × 39
Horizontal resolution	nominal 500 m, actual 407-422 m	nominal 100 m, actual 82-83 m
Vertical resolution	1 m surface, 18.5 m bottom	1 m surface, 18.2 m bottom
Baroclinic / barotropic time step	90 s / 3 s	18 s / 0.6 s
Open boundary update frequency	1 h (W, S, E)	1 h (S, E)
Open Boundary SSH offset	0 cm	0 cm
Tide forcing source	CIOPS-E	STC500
Tidal constituents forced	From parent model at OBC	From parent model at OBC
Equation of state	EOS-80	EOS-80
Free surface	Variable volume	Variable volume
Light penetration	RGB	RGB
Lateral boundary condition	Partial slip (shlat=0.1)	Partial slip (shlat=0.1)
Momentum advection	Vector form, 5 sub-steps for vertical advection	Vector form, 5 sub-steps for vertical advection
Momentum lateral diffusion	Horizontal Laplacian and Smagorinsky	Horizontal Laplacian and Smagorinsky
Tracer advection	Total Variance Dissipation, 5 vertical advection sub-steps	Total Variance Dissipation, 5 vertical advection sub-steps
Tracer lateral diffusion	Iso-neutral Laplacian and Smagorinsky	Iso-neutral Laplacian and Smagorinsky
Vertical diffusion	k-ε	k-ε
Bottom friction	Log-layer	Log-layer

Table 2. Tidal constituent comparison for Port Hawkesbury wharf station. For each constituent, modelled values listed top to bottom for CIOPS-E, STC500 and STC100.

Constituent	Amplitude (A; m)			Phase (φ; °GMT)			Tidal Error (m)
	Observed	Modelled	Difference	Observed	Modelled	Difference	
M2	0.593	0.591	-0.002	345.6	343.3	-2.3	0.017
		0.594	0.001	345.6	344.6	-1.1	0.008
		0.598	0.005	345.6	346.0	0.3	0.004
N2	0.127	0.128	0.001	322.9	321.8	-1.1	0.002
		0.128	0.001	322.9	323.5	0.6	0.001
		0.129	0.002	322.9	324.8	1.9	0.003
S2	0.140	0.128	-0.011	24.5	18.1	-6.4	0.013
		0.130	-0.009	24.5	19.2	-5.3	0.011
		0.131	-0.009	24.5	21.1	-3.4	0.008
K1	0.072	0.085	0.014	50.7	46.7	-4.0	0.010
		0.083	0.011	50.7	46.7	-4.0	0.009
		0.085	0.013	50.7	47.7	-3.0	0.010
O1	0.050	0.057	0.007	343.4	344.4	0.9	0.005
		0.056	0.005	343.4	343.8	0.3	0.004
		0.056	0.006	343.4	345.0	1.6	0.004
K2	0.041	0.038	-0.003	23.5	16.8	-6.7	0.004
		0.039	-0.002	23.5	18.3	-5.2	0.003
		0.039	-0.002	23.5	20.2	-3.3	0.002
P1	0.022	0.026	0.004	37.5	35.3	-2.2	0.003
		0.026	0.004	37.5	35.1	-2.4	0.003
		0.026	0.004	37.5	36.6	-0.9	0.003
Q1	0.007	0.006	-0.000	328.7	331.9	3.2	0.000
		0.006	-0.000	328.7	332.2	3.5	0.000
		0.007	-0.000	328.7	334.9	6.3	0.001

Table 3. Historic tide gauge locations.

Station name	Common Name	Longitude (ºN)	Latitude (ºE)	Length (days)	Start
00563const	Sand Point	-61.2667	45.5167	43	11/2/1999
00570const	Port Hastings	-61.4000	45.6500	29	11/2/1999

Table 4. Tidal constituent comparison from historic tide gauges.

Station name	Amp. Obs. (m)	Phase Obs. (deg)	Amp. Model (m)			Amp (mod.-obs.) (m)			Phase Model (deg)			Phase (mod-obs) (deg)			Tidal error (m)		
			CIOPS-E	STC 500	STC 100	CIOPS-E	STC 500	STC 100	CIOPS-E	STC 500	STC 100	CIOPS-E	STC 500	STC 100	CIOPS-E	STC 500	STC 100
M2																	
00563const	0.596	344.3	0.589	0.597	0.573	-0.007	0.001	-0.023	342.8	344.7	344.7	-1.6	0.4	0.4	0.012	0.003	0.016
00570const	0.597	344.9	0.591	0.593	0.600	-0.006	-0.004	0.003	343.3	344.5	346.0	-1.6	-0.4	1.1	0.012	0.004	0.008
N2																	
00563const	0.119	317.9	0.129	0.130	0.126	0.010	0.011	0.007	321.7	323.3	323.5	3.8	5.5	5.6	0.009	0.012	0.010
00570const	0.134	319.8	0.128	0.128	0.130	-0.006	-0.006	-0.004	321.8	323.5	324.8	2.1	3.7	5.0	0.006	0.007	0.009
S2																	
00563const	0.135	28.3	0.105	0.108	0.104	-0.029	-0.027	-0.031	14.7	17.3	16.8	-13.6	-11.1	-11.5	0.029	0.025	0.028
00570const	0.149	26.0	0.128	0.130	0.131	-0.021	-0.019	-0.018	18.1	19.1	21.2	-7.9	-6.9	-4.8	0.020	0.018	0.015
O1																	
00563const	0.043	343.7	0.053	0.054	0.054	0.010	0.011	0.011	340.6	340.7	340.8	-3.0	-3.0	-2.9	0.008	0.008	0.008
00570const	0.039	330.8	0.057	0.055	0.056	0.018	0.016	0.017	344.3	343.7	345.0	13.5	12.9	14.2	0.015	0.014	0.014
K1																	
00563const	0.072	52.9	0.118	0.120	0.118	0.046	0.048	0.046	39.1	39.3	39.8	-13.8	-13.6	-13.0	0.036	0.037	0.036
00570const	0.064	51.2	0.085	0.083	0.085	0.021	0.019	0.021	46.7	46.8	47.9	-4.5	-4.4	-3.3	0.016	0.014	0.015

Table 5. Water level scores at Port Hawkesbury.

Year	Model	Total				Non-Tidal			Tidal		
		bias (m)	CRMSE (m)	χ^2	Pearson	CRMSE (m)	χ^2	Pearson	CRMSE (m)	χ^2	Pearson
2017	CIOPS-E	0.022	0.081	0.029	0.985	0.067	0.314	0.833	0.046	0.010	0.995
	STC500	0.022	0.081	0.029	0.986	0.068	0.322	0.828	0.044	0.009	0.996
	STC100	0.020	0.076	0.025	0.987	0.065	0.295	0.842	0.039	0.007	0.997
2018	CIOPS-E	0.000	0.080	0.028	0.986	0.067	0.245	0.871	0.045	0.010	0.995
	STC500	-0.001	0.080	0.028	0.986	0.068	0.255	0.865	0.043	0.009	0.996
	STC100	-0.002	0.075	0.025	0.988	0.065	0.231	0.878	0.039	0.007	0.996
2019	CIOPS-E	-0.006	0.083	0.031	0.984	0.070	0.275	0.854	0.046	0.011	0.995
	STC500	-0.007	0.083	0.031	0.984	0.071	0.284	0.849	0.044	0.010	0.995
	STC100	-0.009	0.079	0.028	0.986	0.068	0.262	0.860	0.042	0.009	0.996
2020	CIOPS-E	0.000	0.082	0.031	0.984	0.068	0.309	0.834	0.045	0.010	0.995
	STC500	-0.002	0.081	0.030	0.985	0.069	0.319	0.829	0.043	0.009	0.995
	STC100	-0.003	0.076	0.027	0.987	0.066	0.290	0.844	0.038	0.007	0.996
2021	CIOPS-E	-0.012	0.077	0.028	0.986	0.064	0.241	0.872	0.044	0.010	0.995
	STC500	-0.013	0.077	0.028	0.986	0.065	0.253	0.866	0.043	0.009	0.995
	STC100	-0.014	0.071	0.024	0.988	0.061	0.222	0.882	0.037	0.007	0.997

Table 6. Non-tidal water level scores during six storm periods.

Storm Date	Storm Name	CIOPS-E			STC500			STC100		
		CRMSE (m)	χ^2	Pearson	CRMSE (m)	χ^2	Pearson	CRMSE (m)	χ^2	Pearson
Oct-23-2016	-	0.087	0.399	0.776	0.090	0.420	0.762	0.089	0.412	0.768
Dec-25-2017	Christmas	0.095	0.229	0.879	0.098	0.240	0.873	0.094	0.223	0.885
Jan-05-2018	-	0.085	0.151	0.922	0.087	0.159	0.917	0.083	0.145	0.925
Sep-08-2019	Dorian	0.090	0.341	0.823	0.086	0.313	0.830	0.084	0.303	0.836
Sep-23-2020	Teddy	0.069	0.136	0.931	0.065	0.120	0.942	0.062	0.112	0.947
Nov-24-2021	-	0.081	0.427	0.759	0.087	0.490	0.718	0.081	0.423	0.759

Table 7. Total ADCP skill scores at standard depths (full obs. collection; highlighted are representative stations).

score		bias U (m/s)			bias V (m/s)			χ^2			vector correlation mag.			vector correlation (deg)		
case name		CIOPS-E	STC 500	STC 100	CIOPS-E	STC 500	STC 100	CIOPS-E	STC 500	STC 100	CIOPS-E	STC 500	STC 100	CIOPS-E	STC 500	STC 100
Station name	Depth (m)															
CM1_23088_Nov2016	10	-	0.002	-0.005	-	-0.015	0.012	-	1.195	1.099	-	0.260	0.257	-	-13.0	5.9
	20	-	-0.019	0.005	-	0.002	-0.009	-	0.934	0.874	-	0.428	0.454	-	4.8	1.2
	30	-	-0.032	0.013	-	0.007	-0.017	-	0.716	0.610	-	0.542	0.631	-	10.4	-0.8
CM1_May2016_23091	10	-	-0.005	0.002	-	0.001	0.001	-	1.064	0.953	-	0.349	0.388	-	9.4	0.7
	20	-	-0.012	0.003	-	0.004	-0.005	-	1.001	0.803	-	0.542	0.570	-	-16.9	-4.5
	30	-	-0.010	0.004	-	-0.002	-0.005	-	0.777	0.739	-	0.519	0.615	-	-15.6	-2.1
CM1_Nov2015_23088	10	-	0.007	-0.013	-	-0.017	0.012	-	1.086	1.027	-	0.324	0.285	-	14.4	5.8
	20	-	-0.022	-0.002	-	0.002	-0.007	-	0.912	0.847	-	0.429	0.448	-	-14.7	-2.3
	30	-	-0.030	0.005	-	0.003	-0.012	-	0.654	0.461	-	0.612	0.739	-	-12.7	0.1
CM2_23113_Mar2017	10	-	0.009	0.003	-	-0.004	0.003	-	0.649	0.584	-	0.610	0.674	-	-4.7	0.4
	20	-	-0.003	0.010	-	0.014	-0.008	-	0.659	0.755	-	0.626	0.640	-	6.2	3.4
	30	-	0.004	0.010	-	0.007	-0.003	-	0.471	0.371	-	0.748	0.797	-	-1.0	4.9
	40	-	0.002	-0.007	-	-0.001	-0.004	-	0.812	0.580	-	0.574	0.652	-	-11.7	0.0
CM2_May2016_waves23092	20	-	-0.002	0.010	-	0.012	-0.006	-	0.519	0.594	-	0.722	0.738	-	-0.6	-3.8
	30	-	0.004	0.007	-	0.002	0.001	-	0.442	0.333	-	0.773	0.817	-	-7.2	0.8
	40	-	0.001	-0.009	-	-0.002	-0.005	-	0.797	0.558	-	0.632	0.669	-	-19.7	-4.9
CM2_Sep2016_waves23113	10	-	0.015	-0.011	-	-0.016	0.012	-	0.645	0.583	-	0.609	0.670	-	-6.3	-1.1
	20	-	-0.008	0.024	-	0.025	-0.013	-	0.695	0.882	-	0.598	0.562	-	10.5	6.3
	30	-	0.001	0.020	-	0.019	-0.010	-	0.501	0.387	-	0.722	0.787	-	-1.6	5.1
	40	-	0.002	-0.013	-	-0.011	0.000	-	0.826	0.557	-	0.557	0.667	-	-13.6	-2.9
CM3_Nov2015_23091	10	0.014	-0.014	-0.003	-0.013	0.001	-0.011	0.747	0.903	0.885	0.511	0.471	0.480	5.1	2.3	-1.6
	20	-	-0.043	0.011	-	0.014	-0.020	-	0.572	0.603	-	0.659	0.638	-	-6.2	-4.3
	30	-	-0.030	0.011	-	0.004	-0.006	-	0.450	0.381	-	0.770	0.791	-	11.1	0.0
CM4_Mar2016	10	0.005	-0.002	-0.009	-0.001	-0.011	0.000	0.721	0.642	0.677	0.533	0.632	0.612	-5.3	-2.0	-1.4
	20	-0.003	-0.019	-0.009	-0.011	-0.011	-0.012	0.636	0.496	0.512	0.619	0.713	0.703	-1.0	-4.9	-4.2

score		bias U (m/s)			bias V (m/s)			χ^2			vector correlation mag.			vector correlation (deg)		
case name		CIOPS-E	STC 500	STC 100	CIOPS-E	STC 500	STC 100	CIOPS-E	STC 500	STC 100	CIOPS-E	STC 500	STC 100	CIOPS-E	STC 500	STC 100
Station name	Depth (m)															
CM5_Nov2015_23089	10	-0.018	0.015	-0.017	0.020	-0.016	0.013	0.703	0.762	0.712	0.546	0.515	0.551	2.8	-4.8	-5.2
	20	-0.009	-0.004	-0.006	0.002	-0.007	-0.003	0.730	0.768	0.733	0.522	0.527	0.555	-4.6	-4.8	-6.5
	30	-0.004	-0.015	-0.003	-0.006	-0.005	-0.010	0.743	0.680	0.690	0.511	0.581	0.574	-4.9	-3.9	-2.0
	40	-0.005	-0.011	-0.007	0.002	-0.007	-0.004	0.718	0.710	0.707	0.548	0.569	0.569	-12.2	-5.1	0.1
	50	-0.002	-0.021	-0.009	-0.003	-0.007	-0.006	0.789	0.738	0.692	0.528	0.564	0.587	-22.7	-5.3	-4.1
	60	0.015	-0.016	0.006	-0.005	0.006	-0.005	0.948	0.569	0.549	0.512	0.668	0.680	-50.3	-4.8	-6.8
CM7_23089_Nov2016	10	0.009	0.037	-0.004	0.048	0.000	0.042	0.671	0.519	0.494	0.663	0.708	0.726	2.4	-3.2	-6.6
	20	-	-0.012	0.014	-	0.012	-0.004	-	0.377	0.357	-	0.793	0.802	-	5.5	-0.1
	30	-	-0.040	0.030	-	0.017	-0.026	-	0.396	0.320	-	0.815	0.825	-	15.3	0.4
CM7_May2016_23088	10	0.022	-0.001	0.000	0.019	0.003	0.012	0.746	0.358	0.343	0.551	0.802	0.811	2.9	-1.2	-1.5
	20	-	-0.007	0.008	-	0.003	-0.004	-	0.403	0.381	-	0.795	0.797	-	-13.1	1.0
	30	-	0.020	0.000	-	-0.010	0.013	-	0.442	0.303	-	0.834	0.836	-	-9.3	-0.3
CM8_23091_No	10	-0.001	0.027	0.011	0.006	0.010	0.009	0.695	0.406	0.414	0.623	0.773	0.776	3.0	-4.0	-1.8
	20	-	-0.018	0.013	-	0.016	-0.023	-	0.549	0.435	-	0.759	0.753	-	0.4	2.6
CM8_May2016	10	-0.001	0.027	0.011	0.006	0.010	0.009	0.695	0.406	0.414	0.623	0.773	0.776	3.0	-4.0	-1.8
	20	-	-0.018	0.013	-	0.016	-0.023	-	0.549	0.435	-	0.759	0.753	-	0.4	2.6
Canso_23089_May2017	10	-0.024	-0.018	-0.021	-0.020	-0.025	-0.027	0.613	0.652	0.675	0.656	0.666	0.660	-11.8	-4.1	-4.5
	20	-0.024	-0.010	-0.020	-0.025	-0.018	-0.026	0.566	0.641	0.658	0.685	0.700	0.690	-9.8	-1.6	-3.5
	30	-0.013	0.006	-0.006	-0.001	0.003	0.001	0.544	0.579	0.580	0.713	0.739	0.727	-6.8	-2.5	-3.6
	40	0.021	-0.001	0.009	0.035	0.014	0.048	0.474	0.416	0.415	0.759	0.806	0.790	-1.8	-16.2	-12.3
M2086	10	-0.005	0.019	-0.003	0.023	0.004	0.035	0.846	0.966	1.142	0.419	0.393	0.352	6.0	-0.8	-6.5
	20	-0.004	0.009	0.000	0.011	0.006	0.023	0.863	0.946	1.126	0.405	0.428	0.373	4.2	-4.6	-7.0
	30	-0.002	-0.001	0.001	-0.004	0.007	0.008	0.907	0.999	1.168	0.372	0.417	0.357	0.7	-9.2	-5.8
	40	0.001	0.001	0.006	-0.005	0.012	0.006	0.839	1.053	1.138	0.451	0.408	0.394	1.2	-6.2	-2.4
	50	0.006	-0.004	0.012	-0.012	0.014	-0.004	0.813	1.039	1.104	0.508	0.416	0.409	4.6	6.0	4.5
	60	0.016	-0.019	0.010	-0.015	0.007	-0.011	0.773	0.883	0.951	0.565	0.527	0.525	0.6	4.1	1.7
	70	0.042	-0.026	0.014	-0.014	0.013	-0.021	0.826	0.626	0.667	0.637	0.671	0.664	-16.4	3.7	3.4
M2008	10	0.037	-0.034	-	0.019	-0.030	-	0.775	0.763	-	0.606	0.600	-	1.3	2.9	-

score		bias U (m/s)			bias V (m/s)			χ^2			vector correlation mag.			vector correlation (deg)		
case name		CIOPS-E	STC 500	STC 100	CIOPS-E	STC 500	STC 100	CIOPS-E	STC 500	STC 100	CIOPS-E	STC 500	STC 100	CIOPS-E	STC 500	STC 100
Station name	Depth (m)															
	20	0.034	-0.037	-	0.020	-0.032	-	0.721	0.699	-	0.627	0.628	-	-1.1	-0.4	-
	30	0.026	-0.037	-	0.016	-0.033	-	0.722	0.680	-	0.635	0.652	-	-2.1	-1.2	-
	40	0.020	-0.037	-	0.013	-0.032	-	0.747	0.753	-	0.622	0.628	-	-0.4	1.4	-
	50	0.013	-0.035	-	0.012	-0.030	-	0.722	0.697	-	0.631	0.641	-	2.9	3.4	-
	60	0.006	-0.036	-	0.013	-0.034	-	0.640	0.570	-	0.671	0.693	-	3.9	1.5	-
	70	-0.003	-0.039	-	0.011	-0.037	-	0.748	0.643	-	0.609	0.640	-	7.4	3.9	-
M2088	10	0.057	-0.049	-	0.074	-0.014	-	0.552	0.587	-	0.717	0.690	-	-3.8	-1.4	-
	20	0.052	-0.053	-	0.073	-0.018	-	0.512	0.543	-	0.734	0.711	-	-3.7	-2.1	-
	30	0.044	-0.053	-	0.066	-0.024	-	0.519	0.538	-	0.739	0.727	-	-5.1	-2.9	-
	40	0.039	-0.044	-	0.056	-0.021	-	0.615	0.631	-	0.694	0.684	-	-5.8	-2.4	-
	50	0.042	-0.023	-	0.049	-0.010	-	0.595	0.531	-	0.727	0.728	-	2.2	2.5	-
	60	0.045	-0.017	-	0.049	-0.002	-	0.705	0.510	-	0.721	0.728	-	5.1	0.5	-
	70	0.047	-0.001	-	0.042	0.016	-	0.843	0.549	-	0.625	0.684	-	9.1	-0.5	-

Table 8. Non-tidal ADCP skill scores at standard depths (full obs. collection; highlighted are representative stations).

score		RMSE (m/s)			χ^2			vector correlation mag.			vector correlation (deg)		
case name		CIOPS-E	STC500	STC100	CIOPS-E	STC500	STC100	CIOPS-E	STC500	STC100	CIOPS-E	STC500	STC100
Station name	Depth (m)												
CM1_23088 _Nov2016	10	-	0.062	0.066	-	1.121	1.174	-	0.103	0.095	-	-78.4	13.3
	20	-	0.059	0.059	-	0.905	0.921	-	0.363	0.383	-	9.2	1.9
	30	-	0.073	0.067	-	0.732	0.642	-	0.556	0.603	-	12.4	-1.3
CM1_May2016 _23091	10	-	0.070	0.071	-	0.995	1.020	-	0.281	0.307	-	11.3	1.8
	20	-	0.069	0.065	-	0.941	0.845	-	0.498	0.525	-	-17.9	-4.7
	30	-	0.069	0.065	-	0.763	0.693	-	0.504	0.597	-	-14.9	-2.4
CM1_Nov2015 _23088	10	-	0.065	0.070	-	0.991	1.088	-	0.232	0.168	-	37.6	9.2
	20	-	0.066	0.066	-	0.853	0.875	-	0.408	0.394	-	-19.2	-3.5
	30	-	0.072	0.058	-	0.683	0.477	-	0.619	0.725	-	-12.6	0.0
	10	-	0.073	0.070	-	0.731	0.673	-	0.524	0.592	-	-8.3	0.0

score		RMSE (m/s)			χ^2			vector correlation mag.			vector correlation (deg)		
case name		CIOPS-E	STC500	STC100	CIOPS-E	STC500	STC100	CIOPS-E	STC500	STC100	CIOPS-E	STC500	STC100
Station name	Depth (m)												
CM2_23113_Mar2017	20	-	0.065	0.071	-	0.746	0.876	-	0.545	0.561	-	6.1	3.0
	30	-	0.086	0.076	-	0.492	0.393	-	0.736	0.784	-	-1.8	5.0
	40	-	0.095	0.081	-	0.842	0.623	-	0.528	0.619	-	-12.5	0.5
CM2_May2016_waves23092	20	-	0.059	0.064	-	0.609	0.703	-	0.652	0.675	-	-1.3	-4.1
	30	-	0.078	0.068	-	0.457	0.357	-	0.769	0.802	-	-7.8	0.8
	40	-	0.088	0.074	-	0.815	0.571	-	0.643	0.657	-	-19.9	-4.8
CM2_Sep2016_waves23113	10	-	0.077	0.076	-	0.710	0.667	-	0.550	0.589	-	-6.7	1.1
	20	-	0.071	0.081	-	0.852	1.103	-	0.445	0.388	-	13.6	5.3
	30	-	0.089	0.077	-	0.457	0.334	-	0.776	0.819	-	-2.1	4.9
	40	-	0.095	0.077	-	0.814	0.534	-	0.587	0.684	-	-15.0	-2.7
CM3_Nov2015_23091	10	0.066	0.072	0.072	1.003	1.267	1.265	0.161	0.176	0.171	12.9	25.6	13.8
	20	-	0.074	0.076	-	0.737	0.791	-	0.526	0.484	-	-10.8	-4.8
	30	-	0.079	0.073	-	0.514	0.442	-	0.733	0.752	-	11.6	-0.2
CM4_Mar2016_23113	10	0.067	0.066	0.069	1.007	0.935	0.975	0.276	0.420	0.407	14.4	1.1	-0.1
	20	0.075	0.068	0.070	0.719	0.599	0.620	0.539	0.636	0.621	7.9	-4.8	-3.9
CM5_Nov2015_23089	10	0.093	0.097	0.095	0.755	0.810	0.787	0.500	0.460	0.485	7.5	-5.5	-8.3
	20	0.077	0.077	0.077	0.825	0.830	0.835	0.421	0.462	0.475	-5.8	-8.9	-14.4
	30	0.086	0.080	0.082	0.862	0.754	0.793	0.386	0.516	0.485	-7.1	-5.5	-5.3
	40	0.081	0.080	0.080	0.834	0.823	0.819	0.437	0.476	0.470	-15.3	-8.9	-0.9
	50	0.076	0.074	0.072	0.880	0.883	0.827	0.387	0.449	0.483	-24.9	-11.7	-9.3
	60	0.074	0.061	0.060	0.971	0.711	0.679	0.355	0.570	0.589	-53.0	-3.5	-6.9
CM7_23089_Nov2016	10	0.096	0.104	0.100	1.014	1.110	1.062	0.221	0.087	0.193	71.4	12.6	-6.2
	20	-	0.082	0.081	-	0.993	0.964	-	0.270	0.313	-	12.4	2.9
	30	-	0.098	0.095	-	0.674	0.635	-	0.585	0.605	-	10.6	-1.7
CM7_May2016_23088	10	0.106	0.087	0.084	1.126	0.763	0.736	0.107	0.488	0.527	-167.0	3.0	-2.4
	20	-	0.082	0.084	-	0.802	0.850	-	0.529	0.547	-	-11.9	1.7
	30	-	0.108	0.095	-	0.597	0.475	-	0.723	0.725	-	-8.6	-2.4
CM8_23091_Nov2016	10	0.088	0.079	0.081	1.110	0.953	0.999	0.087	0.278	0.240	148.0	3.1	-2.7
	20	-	0.085	0.088	-	0.945	1.002		0.235	0.203	-	0.7	6.9
CM8_May2016_23099	10	0.088	0.079	0.081	1.110	0.953	0.999	0.087	0.278	0.240	148.0	3.1	-2.7
	20	-	0.085	0.088	-	0.945	1.002	-	0.235	0.203	-	0.7	6.9

score		RMSE (m/s)			χ^2			vector correlation mag.			vector correlation (deg)		
case name		CIOPS-E	STC500	STC100	CIOPS-E	STC500	STC100	CIOPS-E	STC500	STC100	CIOPS-E	STC500	STC100
Station name	Depth (m)												
Canso_23089 _May2017	10	0.167	0.171	0.176	0.691	0.725	0.752	0.601	0.612	0.604	-14.4	-5.7	-6.2
	20	0.153	0.160	0.162	0.666	0.722	0.744	0.616	0.641	0.631	-14.3	-4.2	-6.5
	30	0.147	0.150	0.151	0.622	0.648	0.663	0.656	0.675	0.661	-12.4	-2.6	-3.9
	40	0.128	0.122	0.129	0.632	0.538	0.558	0.682	0.712	0.683	-15.1	-14.7	-9.3
M2086	10	0.121	0.129	0.140	0.918	1.044	1.183	0.332	0.310	0.306	10.6	4.7	-5.5
	20	0.107	0.112	0.122	0.971	1.063	1.244	0.279	0.320	0.283	11.3	-0.4	-4.6
	30	0.099	0.104	0.112	1.020	1.129	1.277	0.241	0.308	0.280	5.8	-6.4	-1.1
	40	0.091	0.101	0.104	0.947	1.163	1.221	0.344	0.315	0.335	3.7	-3.4	2.0
	50	0.085	0.095	0.097	0.900	1.102	1.168	0.436	0.356	0.364	8.1	9.5	7.8
	60	0.090	0.094	0.097	0.850	0.958	1.039	0.522	0.478	0.471	3.1	6.4	2.9
	70	0.108	0.087	0.091	0.890	0.702	0.742	0.630	0.627	0.616	-17.8	3.7	3.3
M2087	10	0.205	0.200	-	0.870	0.853	-	0.548	0.532	-	1.8	3.6	-
	20	0.193	0.187	-	0.836	0.802	-	0.555	0.553	-	-1.0	-0.1	-
	30	0.173	0.165	-	0.865	0.806	-	0.551	0.569	-	-3.2	-1.8	-
	40	0.163	0.162	-	0.959	0.960	-	0.503	0.511	-	-1.6	0.4	-
	50	0.162	0.158	-	0.901	0.876	-	0.513	0.519	-	2.2	2.7	-
	60	0.156	0.149	-	0.831	0.755	-	0.552	0.571	-	3.3	3.9	-
	70	0.138	0.132	-	0.909	0.822	-	0.504	0.515	-	5.0	6.8	-
M2088	10	0.172	0.174	-	0.679	0.702	-	0.652	0.609	-	-5.4	-3.9	-
	20	0.163	0.167	-	0.648	0.676	-	0.663	0.622	-	-5.2	-4.9	-
	30	0.146	0.150	-	0.696	0.729	-	0.658	0.616	-	-7.9	-7.5	-
	40	0.144	0.146	-	0.877	0.892	-	0.562	0.524	-	-9.9	-6.8	-
	50	0.134	0.128	-	0.765	0.688	-	0.621	0.614	-	1.6	3.6	-
	60	0.130	0.117	-	0.816	0.629	-	0.639	0.643	-	3.7	0.7	-
	70	0.125	0.108	-	0.934	0.669	-	0.552	0.594	-	9.6	0.0	-

Table 9. Tidal ADCP skill scores at standard depths (full obs. collection; highlighted are representative stations).

score		RMSE (m/s)			χ^2		
case name		CIOPS-E	STC500	STC100	CIOPS-E	STC500	STC100
Station name	Depth (m)						
CM1_23088 _Nov2016	10	-	0.026	0.013	-	1.657	0.444
	20	-	0.021	0.013	-	0.958	0.377
	30	-	0.017	0.013	-	0.458	0.261
CM1_May2016 _23091	10	-	0.030	0.015	-	1.452	0.365
	20	-	0.027	0.014	-	1.270	0.350
	30	-	0.021	0.024	-	0.802	1.016
CM1_Nov2015 _23088	10	-	0.034	0.023	-	1.375	0.658
	20	-	0.026	0.016	-	1.218	0.463
	30	-	0.024	0.020	-	0.471	0.336
CM2_23113 _Mar2017	10	-	0.028	0.024	-	0.363	0.275
	20	-	0.022	0.021	-	0.327	0.292
	30	-	0.029	0.024	-	0.338	0.237
	40	-	0.036	0.026	-	0.655	0.348
CM2_May2016_ waves23092	20	-	0.015	0.014	-	0.153	0.144
	30	-	0.024	0.017	-	0.325	0.154
	40	-	0.025	0.020	-	0.647	0.427
CM2_Sep2016_ waves23113	10	-	0.030	0.026	-	0.379	0.288
	20	-	0.028	0.029	-	0.333	0.359
	30	-	0.043	0.041	-	0.754	0.690
	40	-	0.053	0.044	-	0.868	0.603
CM3_Nov2015 _23091	10	0.028	0.025	0.023	0.310	0.252	0.222
	20	-	0.022	0.021	-	0.169	0.163
	30	-	0.029	0.024	-	0.228	0.160
CM4_Mar2016 _23113	10	0.041	0.036	0.038	0.408	0.316	0.347
	20	0.045	0.036	0.036	0.496	0.318	0.324
CM5_Nov2015 _23089	10	0.033	0.035	0.029	0.467	0.531	0.347
	20	0.028	0.031	0.025	0.388	0.480	0.307
	30	0.022	0.027	0.022	0.244	0.368	0.249
	40	0.022	0.022	0.022	0.247	0.248	0.246
	50	0.032	0.023	0.022	0.510	0.274	0.252
	60	0.043	0.021	0.021	0.893	0.217	0.221
CM7_23089 _Nov2016	10	0.064	0.023	0.022	0.407	0.052	0.050
	20	-	0.029	0.026	-	0.060	0.050
	30	-	0.048	0.025	-	0.153	0.041
CM7_May2016 _23088	10	0.077	0.022	0.020	0.465	0.037	0.033
	20	-	0.037	0.023	-	0.118	0.046
	30	-	0.053	0.022	-	0.221	0.037

score		RMSE (m/s)			χ^2		
case name		CIOPS-E	STC500	STC100	CIOPS-E	STC500	STC100
Station name	Depth (m)						
CM8_23091 _Nov2016	10	0.067	0.022	0.019	0.440	0.049	0.037
	20	-	0.054	0.019	-	0.282	0.037
CM8_May2016 _23099	10	0.067	0.022	0.019	0.440	0.049	0.037
	20	-	0.054	0.019	-	0.282	0.037
Canso_23089 _May2017	10	0.044	0.050	0.050	0.237	0.305	0.311
	20	0.037	0.050	0.049	0.157	0.291	0.280
	30	0.045	0.051	0.045	0.227	0.288	0.222
	40	0.052	0.053	0.046	0.193	0.195	0.146
M2086	10	0.024	0.024	0.035	0.265	0.271	0.587
	20	0.023	0.022	0.033	0.264	0.249	0.543
	30	0.025	0.025	0.033	0.308	0.328	0.553
	40	0.022	0.028	0.032	0.292	0.462	0.605
	50	0.020	0.029	0.030	0.282	0.582	0.608
	60	0.022	0.026	0.025	0.289	0.410	0.381
	70	0.028	0.018	0.018	0.405	0.176	0.177
M2087	10	0.052	0.053	-	0.304	0.327	-
	20	0.046	0.048	-	0.225	0.245	-
	30	0.044	0.046	-	0.214	0.237	-
	40	0.040	0.042	-	0.168	0.186	-
	50	0.043	0.039	-	0.185	0.159	-
	60	0.037	0.028	-	0.127	0.074	-
	70	0.041	0.026	-	0.257	0.101	-
M2088	10	0.031	0.041	-	0.102	0.171	-
	20	0.031	0.036	-	0.093	0.123	-
	30	0.033	0.030	-	0.100	0.087	-
	40	0.030	0.031	-	0.090	0.094	-
	50	0.036	0.033	-	0.157	0.130	-
	60	0.050	0.033	-	0.396	0.169	-
	70	0.049	0.028	-	0.531	0.173	-

Table 10. *Model skill scores for SST and MCTD instrument stations.*

Station	bias (ºC ; PSU)			CRMSE (ºC ; PSU)			χ^2			Pearson		
	CIOPS-E	STC 500	STC 100	CIOPS-E	STC 500	STC 100	CIOPS-E	STC 500	STC 100	CIOPS-E	STC 500	STC 100
SST												
44488	-0.519	-0.281	-0.278	1.042	0.932	0.940	0.025	0.020	0.021	0.989	0.990	0.990
44489	-0.359	-0.243	-0.188	0.815	0.813	0.806	0.016	0.016	0.016	0.993	0.992	0.992
MCTD Temperature												
CW_55m	-	-	1.603	-	-	0.880	-	-	0.212	-	-	0.970
CB_10m	-0.722	-0.428	-0.357	1.457	1.239	1.256	0.063	0.045	0.046	0.971	0.980	0.979
CB_48m	0.062	0.303	0.362	1.117	0.988	1.022	0.120	0.097	0.104	0.938	0.953	0.948
MCTD Salinity												
CW_55m	-	-	0.198	-	-	0.158	-	-	0.454	-	-	0.751
CB_10m	0.418	0.406	0.405	0.178	0.174	0.179	0.192	0.187	0.198	0.912	0.915	0.910
CB_48m	0.290	0.202	0.225	0.318	0.202	0.205	0.395	0.169	0.175	0.779	0.913	0.910

Table 11. Hourly mean drift scores.

Hour	Molcard Skill		Separation Distance (km)	
	CIOPS-E	STC500	CIOPS-E	STC500
1	0.35	0.37	0.47	0.43
2	0.35	0.37	0.94	0.85
3	0.35	0.38	1.38	1.25
4	0.35	0.38	1.82	1.63
5	0.35	0.38	2.24	1.99
6	0.34	0.38	2.66	2.32
7	0.34	0.39	3.06	2.64
8	0.33	0.39	3.47	2.95
9	0.33	0.39	3.87	3.24
10	0.32	0.39	4.27	3.54
11	0.31	0.38	4.67	3.84
12	0.31	0.38	5.07	4.14
13	0.3	0.38	5.46	4.44
14	0.29	0.37	5.86	4.74
15	0.29	0.37	6.25	5.04
16	0.28	0.37	6.64	5.34
17	0.28	0.36	7.03	5.65
18	0.28	0.36	7.42	5.95
19	0.27	0.36	7.81	6.26
20	0.27	0.35	8.21	6.56
21	0.27	0.35	8.6	6.87
22	0.27	0.35	8.99	7.17
23	0.27	0.34	9.39	7.46
24	0.27	0.34	9.81	7.75

12. FIGURES

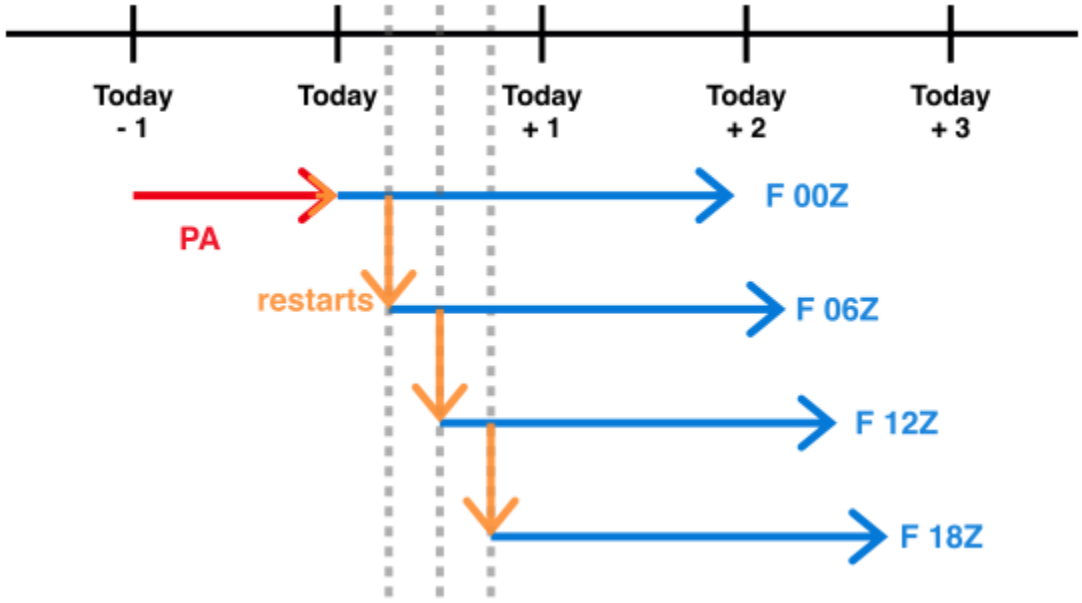

Figure 1. Schematic of one timestamp's set of pseudo-analysis (PA, in red) and forecast (in blue) runs. Grey dashed lines are spaced six hours apart, and orange arrows indicate where a restart file is generated and used to launch the subsequent step. The PA for today+1 will start with the same restart used to start today's 00Z forecast, and the pattern will repeat.

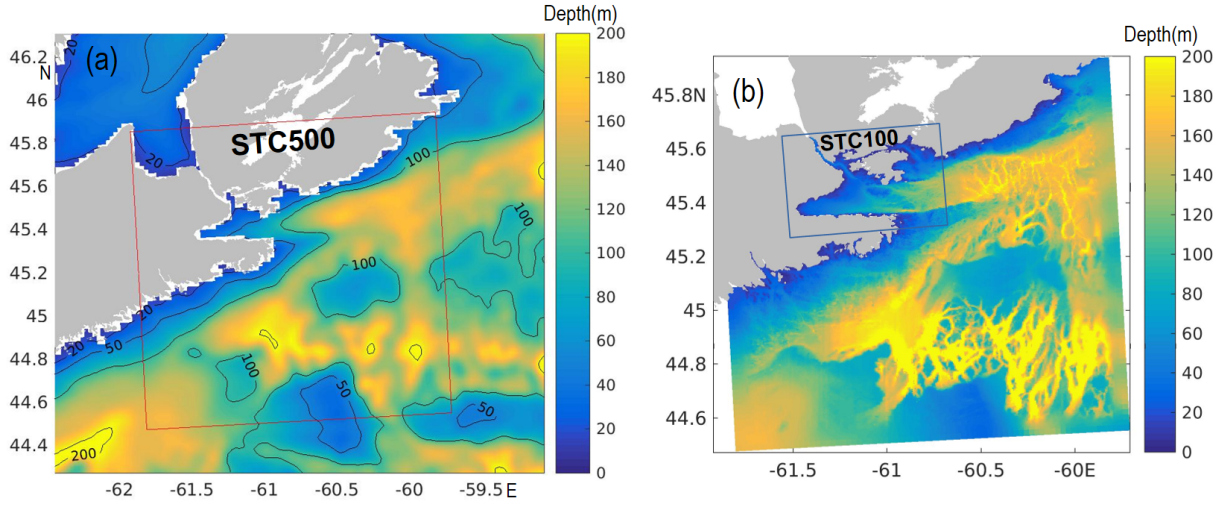

Figure 2. Port model domains: (a) STC500 inset shows nesting in CIOPS-E with CIOPS-E bathymetry, (b) STC100 inset shows nesting in STC500 domain with STC500 bathymetry. Reproduced from DH22.

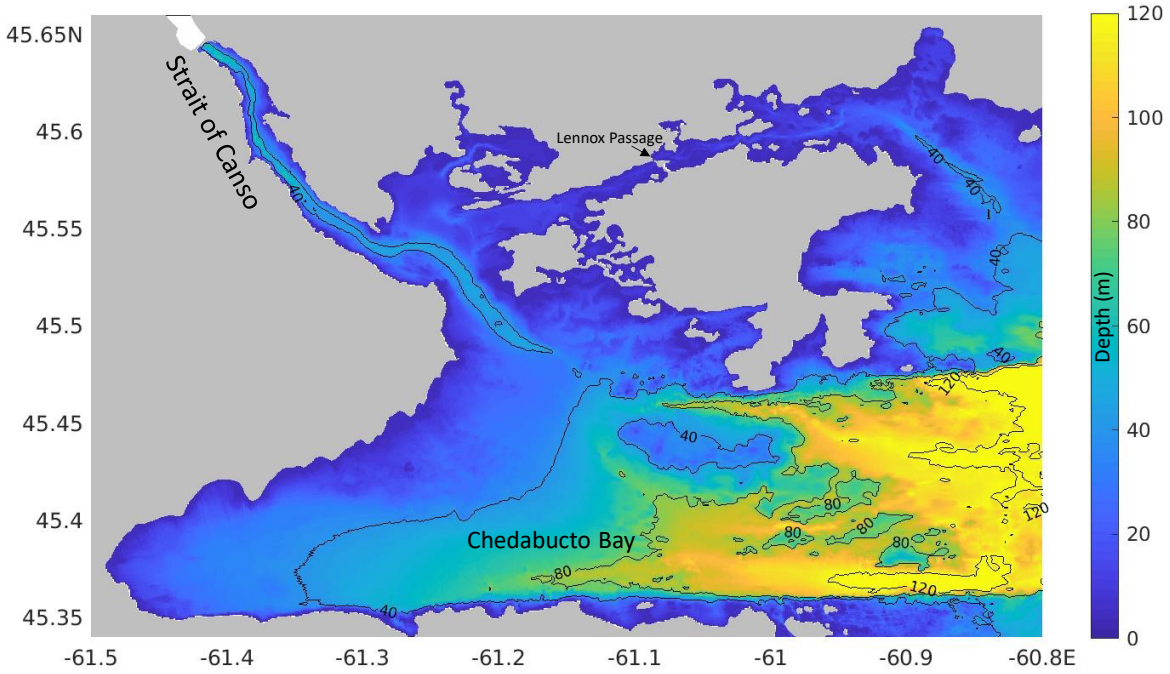

Figure 3. A detailed map of inner port area.

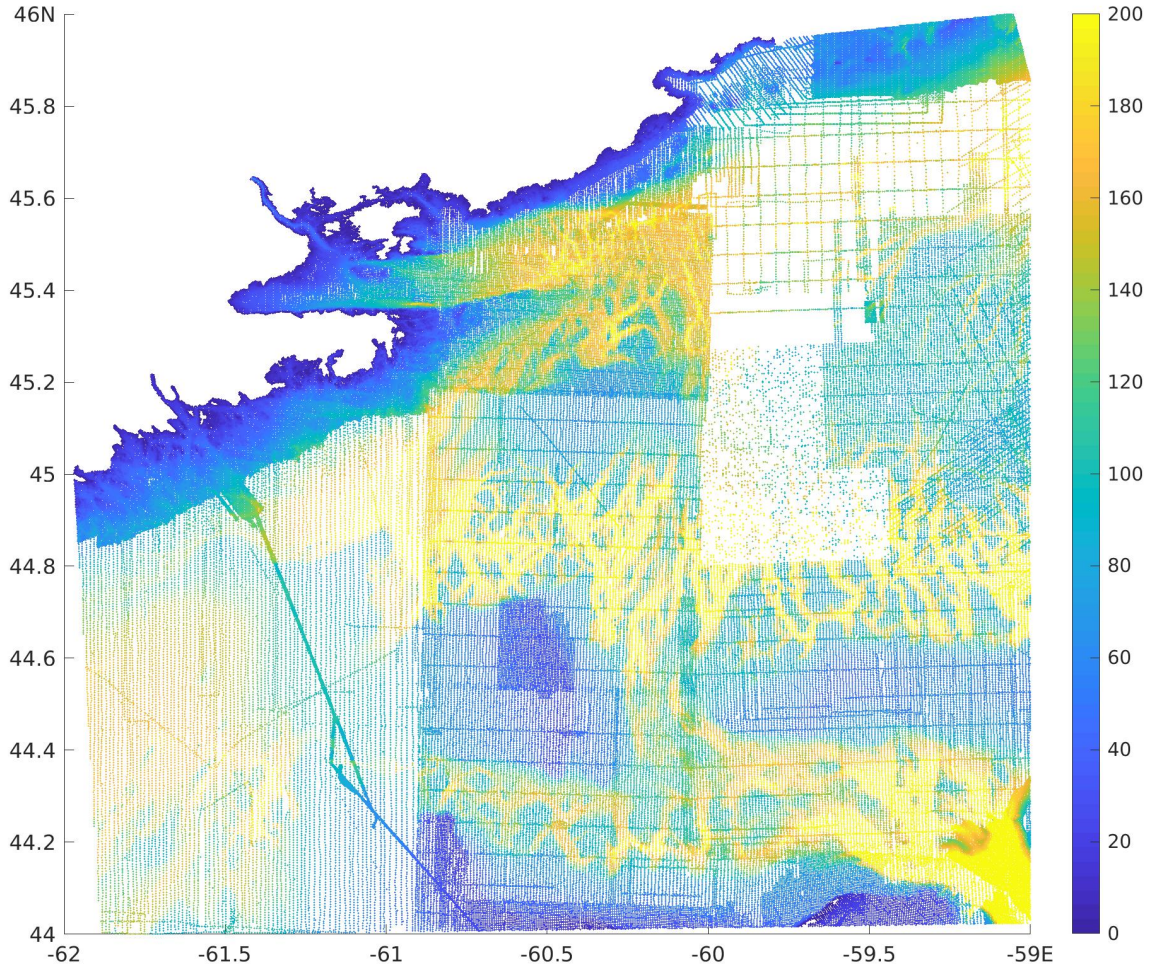

Figure 4. Original CHS data horizontally decimated with 200 m median box filter. Reproduced from DH22.

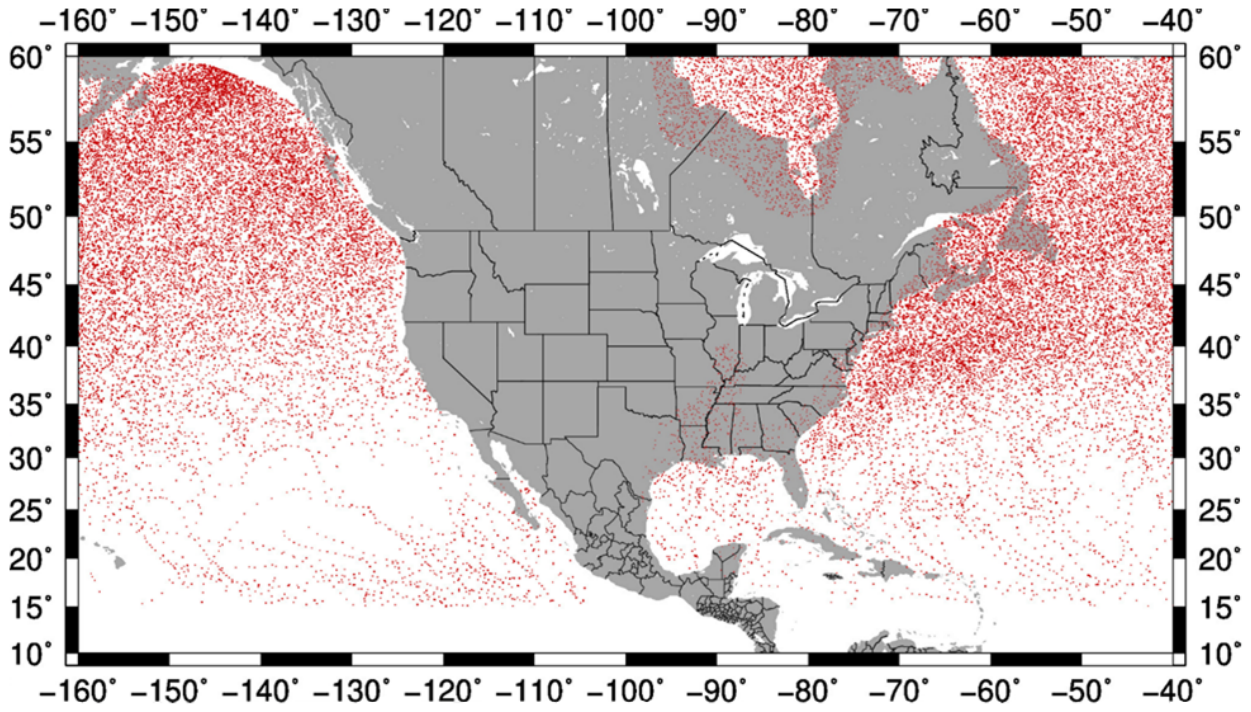

Figure 5. Cyclone locations every six hours from 2010-2021.

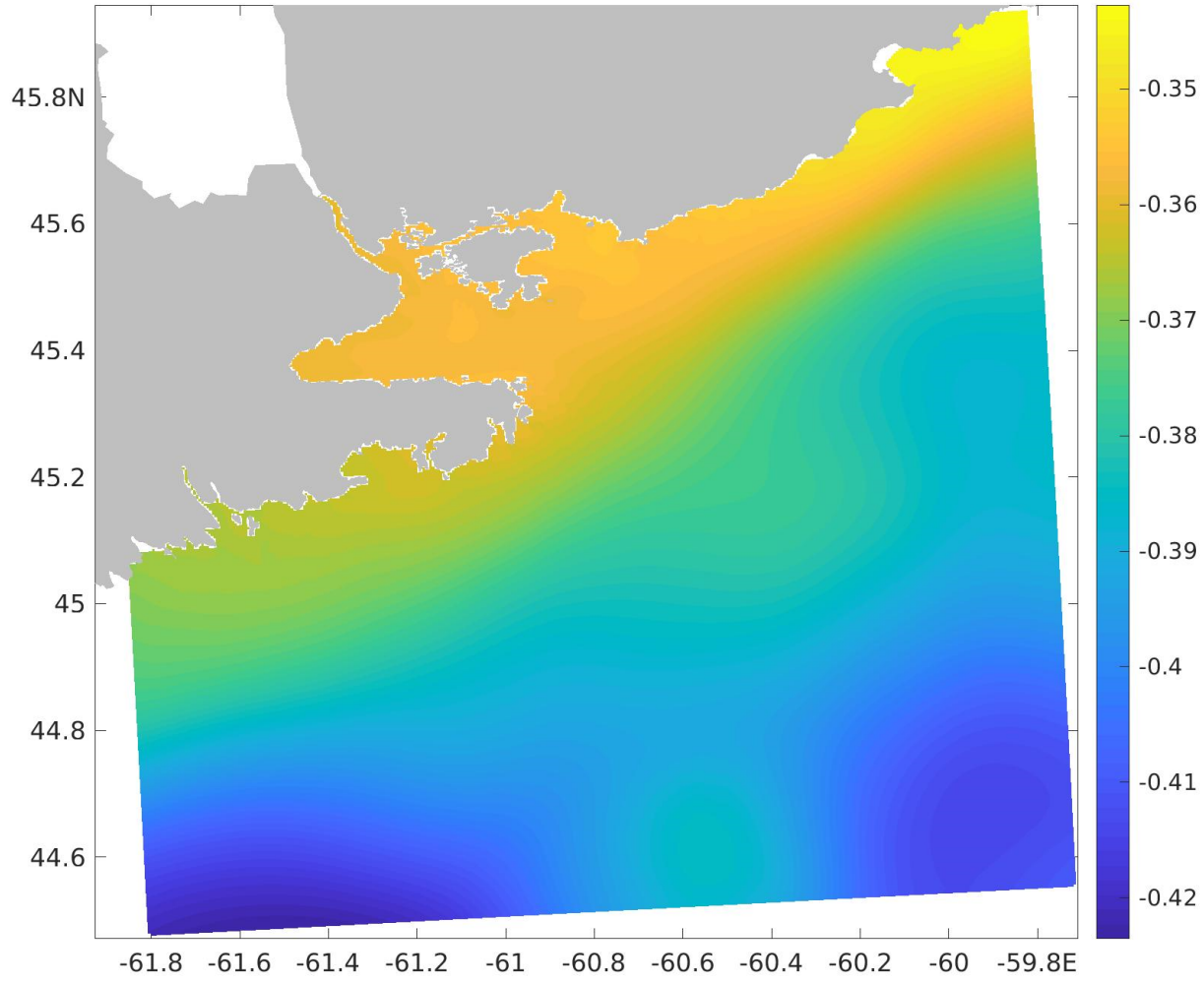

Figure 6. Mean sea surface height (m) from STC500 calculated for 2016-2021.

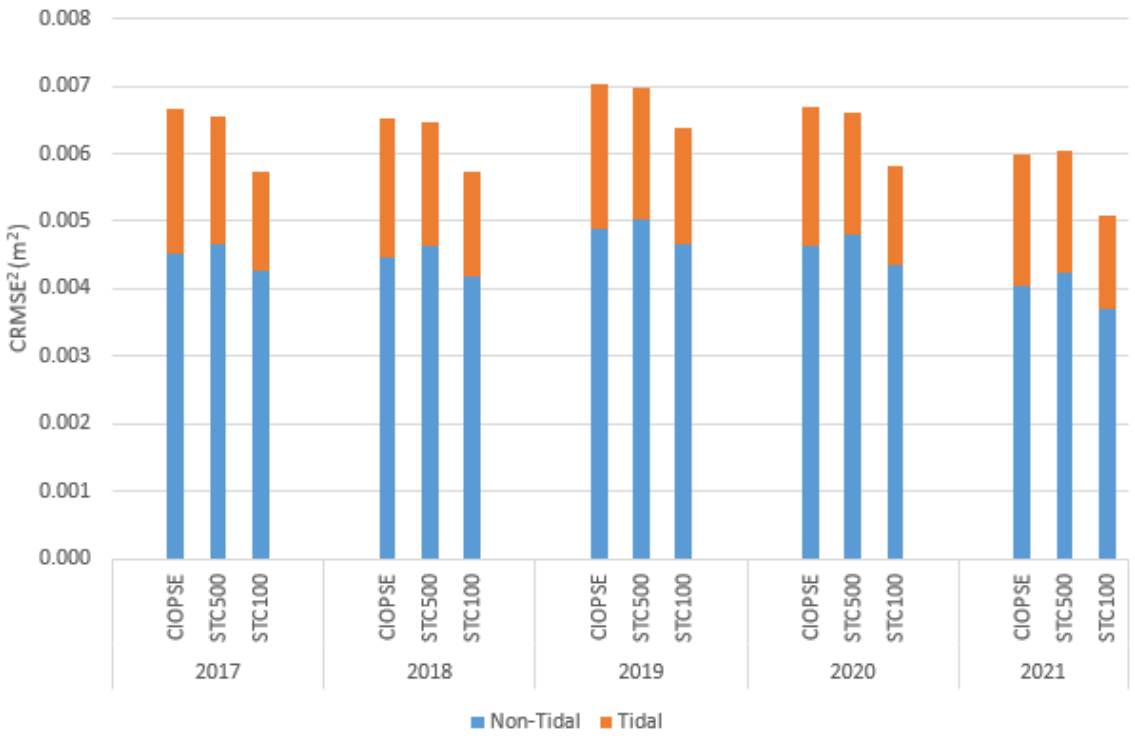

Figure 7. Inter-annual variation of unmodelled variance ($CRMSE^2$).

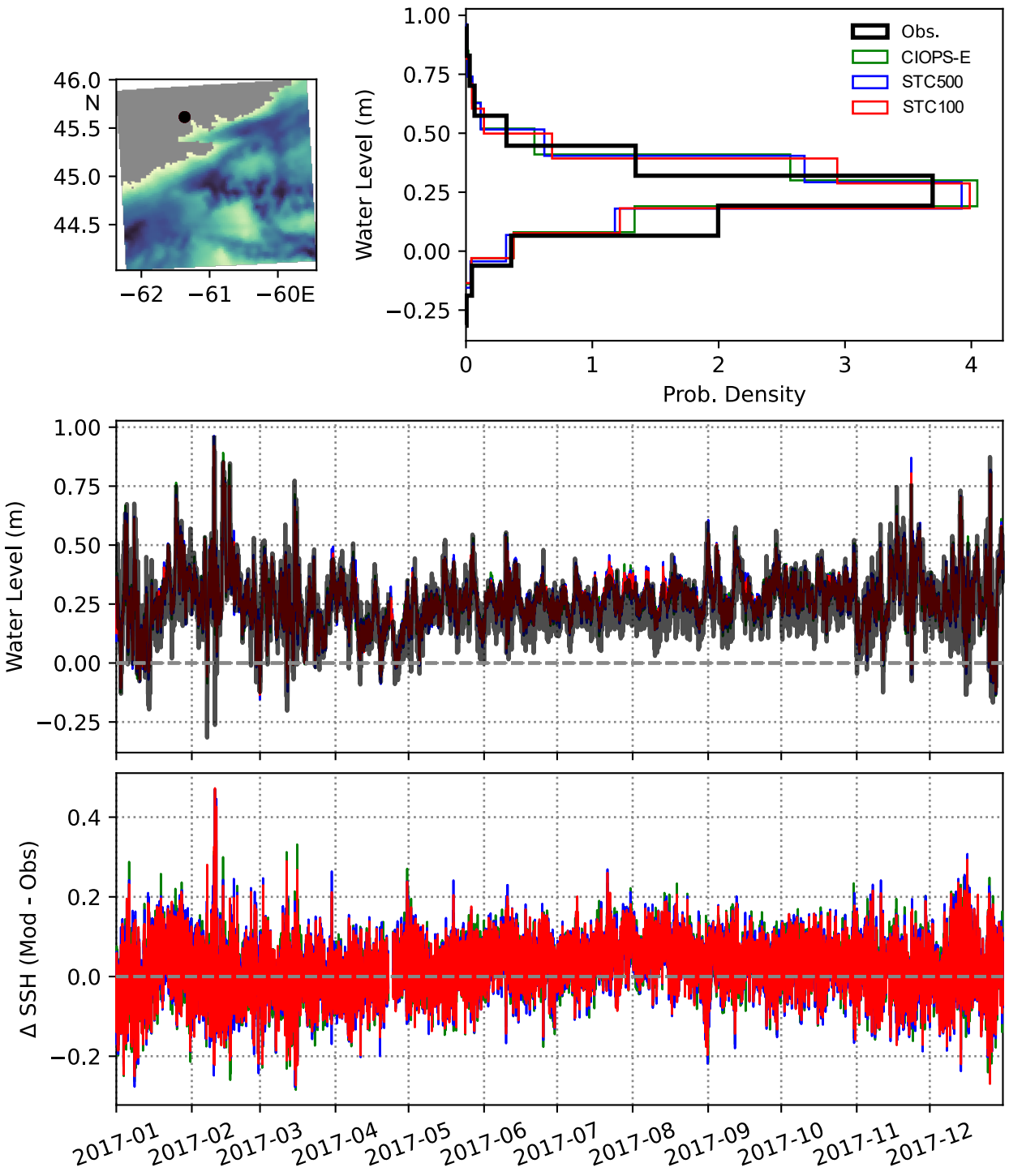

Figure 8. Observed and modelled (2017) non-tidal water level (CGVD28) and error. Dashed gray line highlights zero. Location of gauge shown in map.

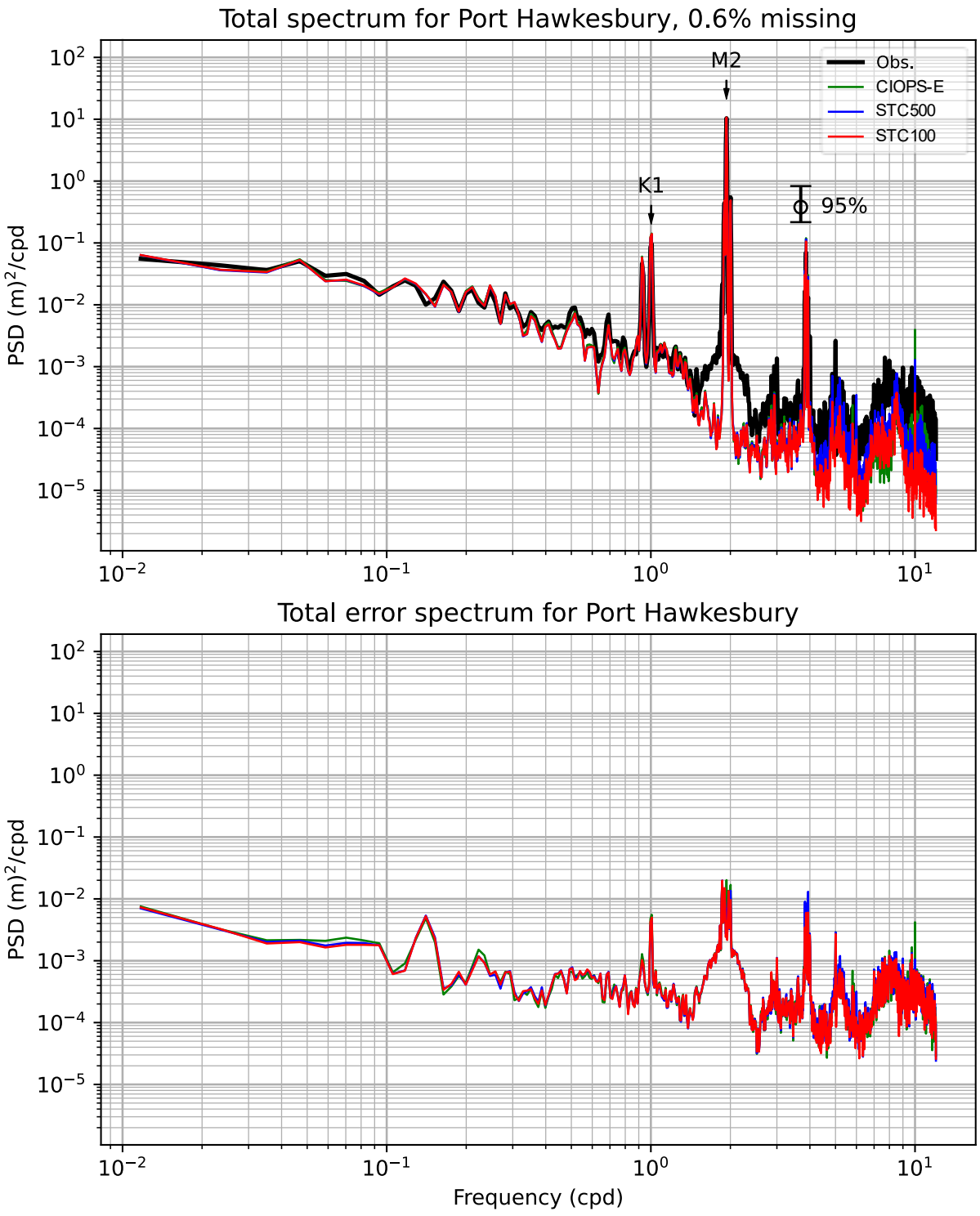

Figure 9. Total water level power spectra from gauge at Port Hawkesbury based on 2017 data.

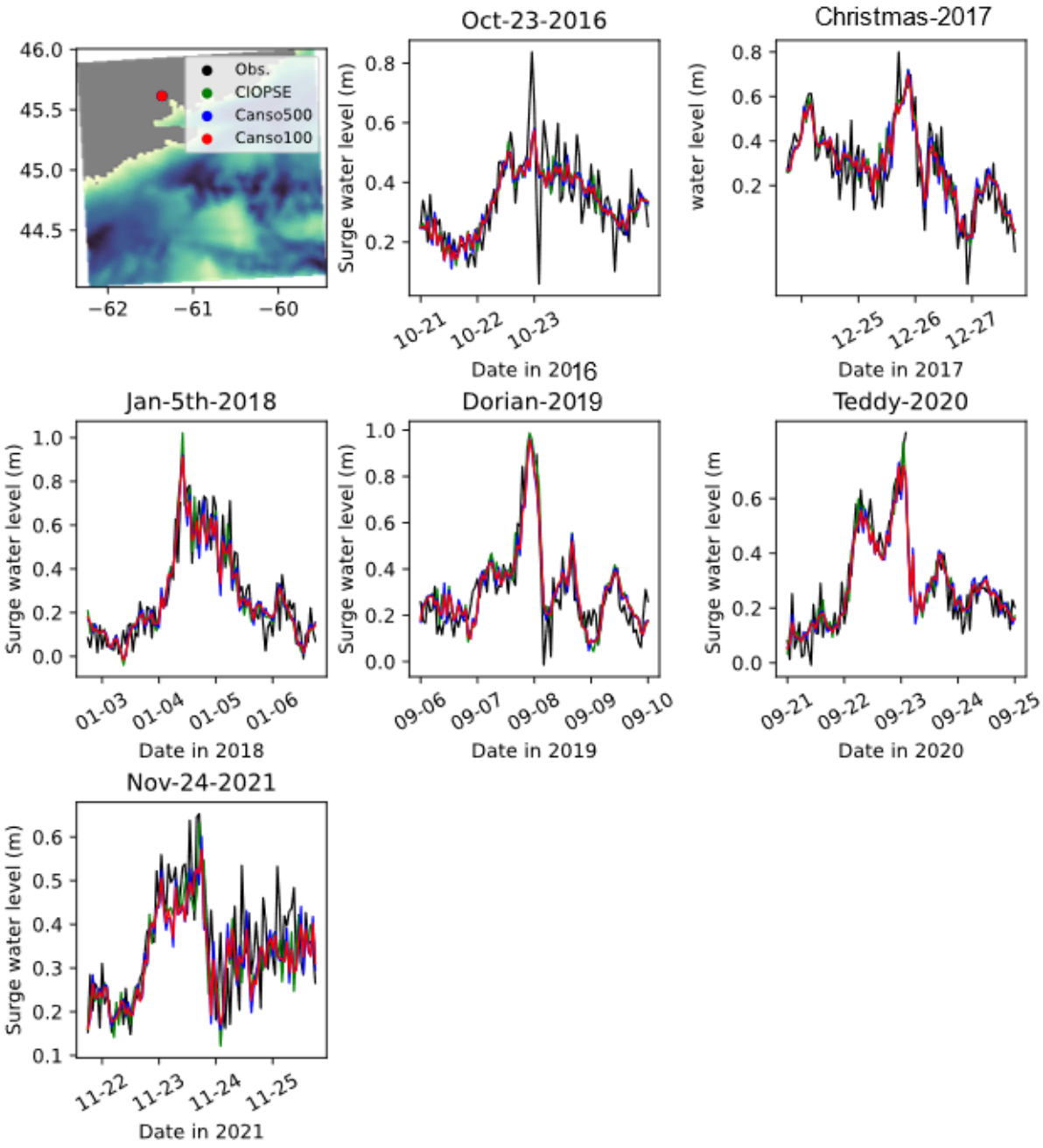

Figure 10. Non-tidal water level at Port Hawkesbury gauge during six documented storms.

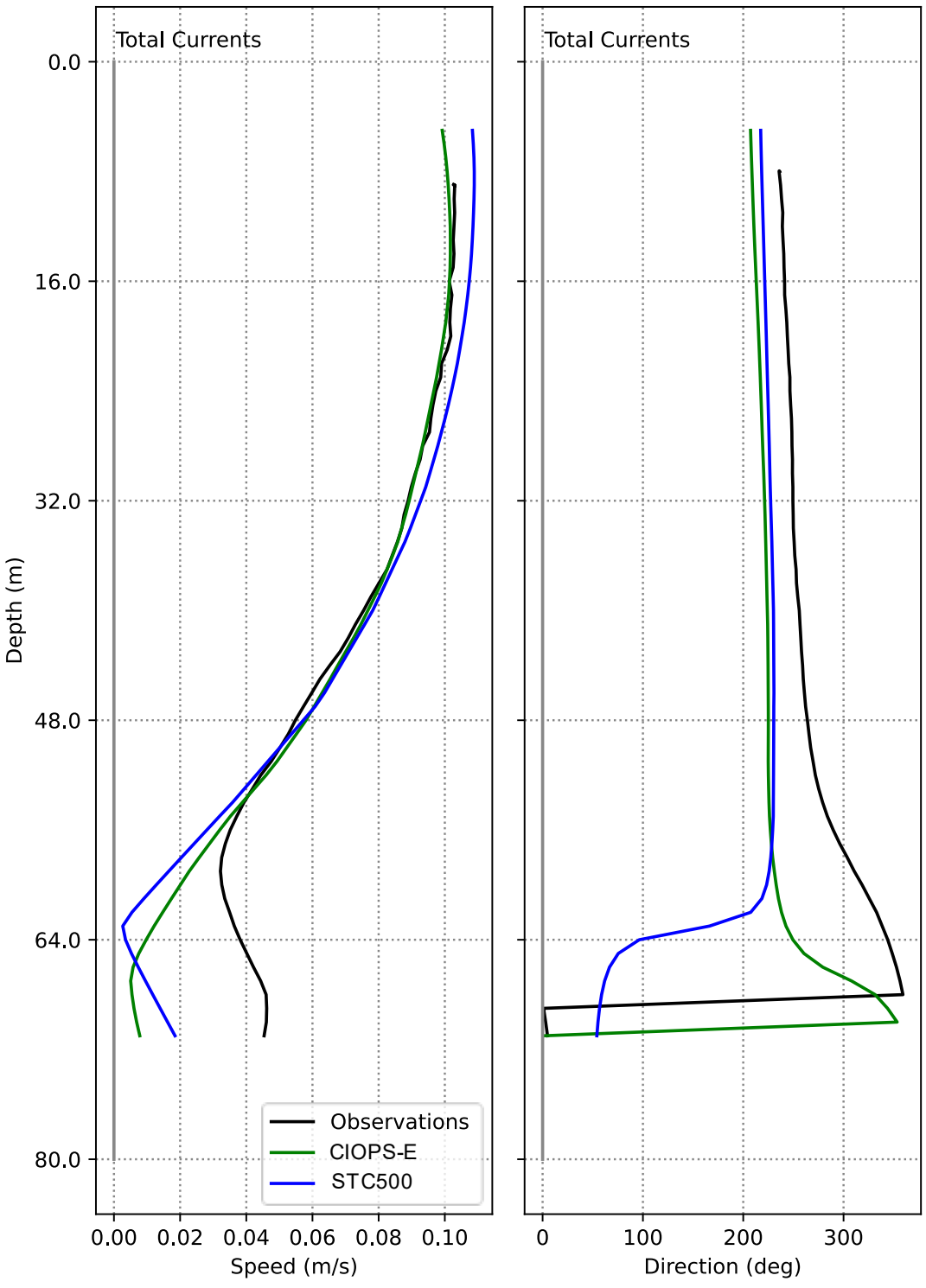

Figure 11. Vertical profile of mean current at M2087.

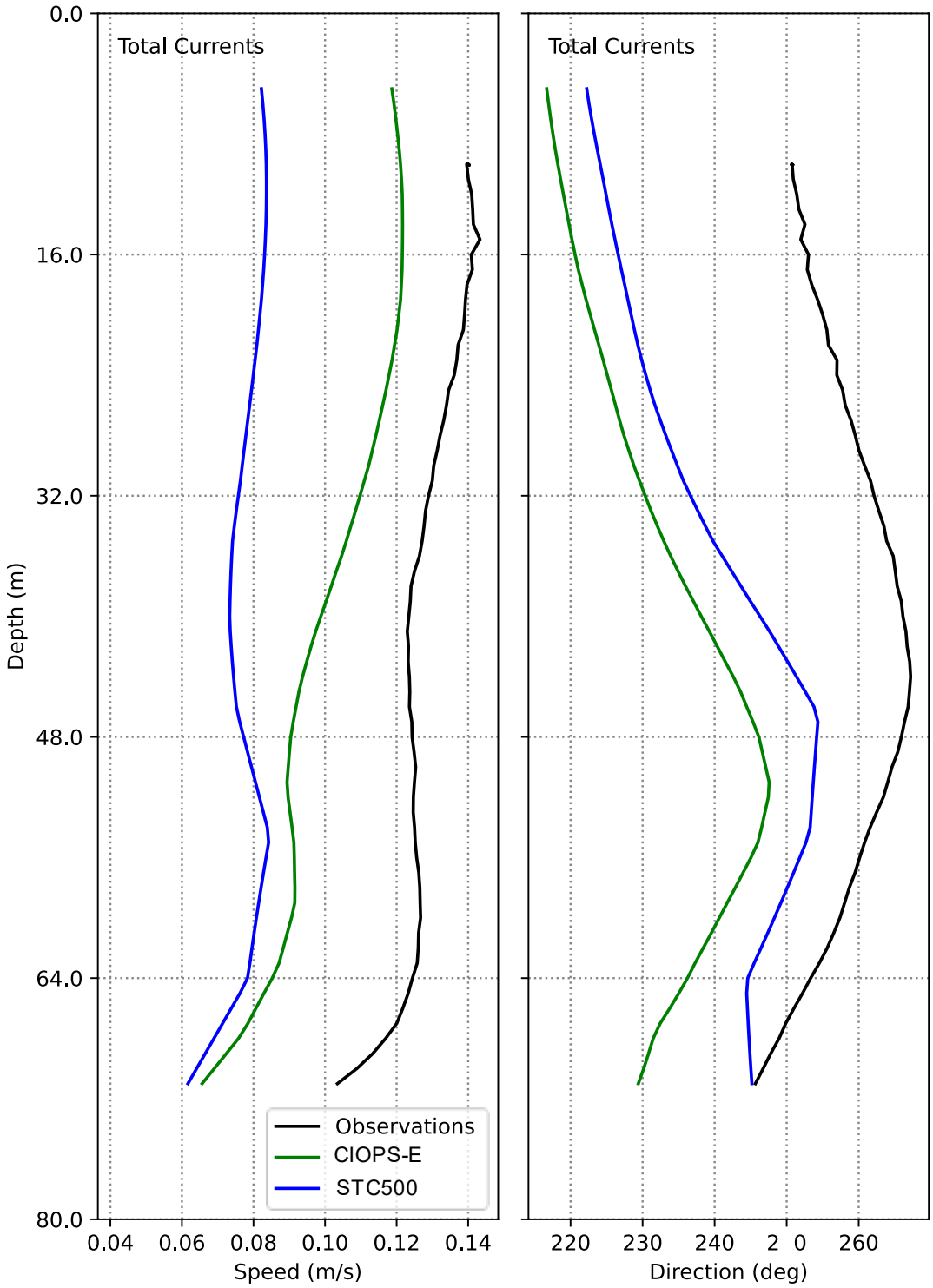

Figure 12. Vertical profile of mean current at M2088.

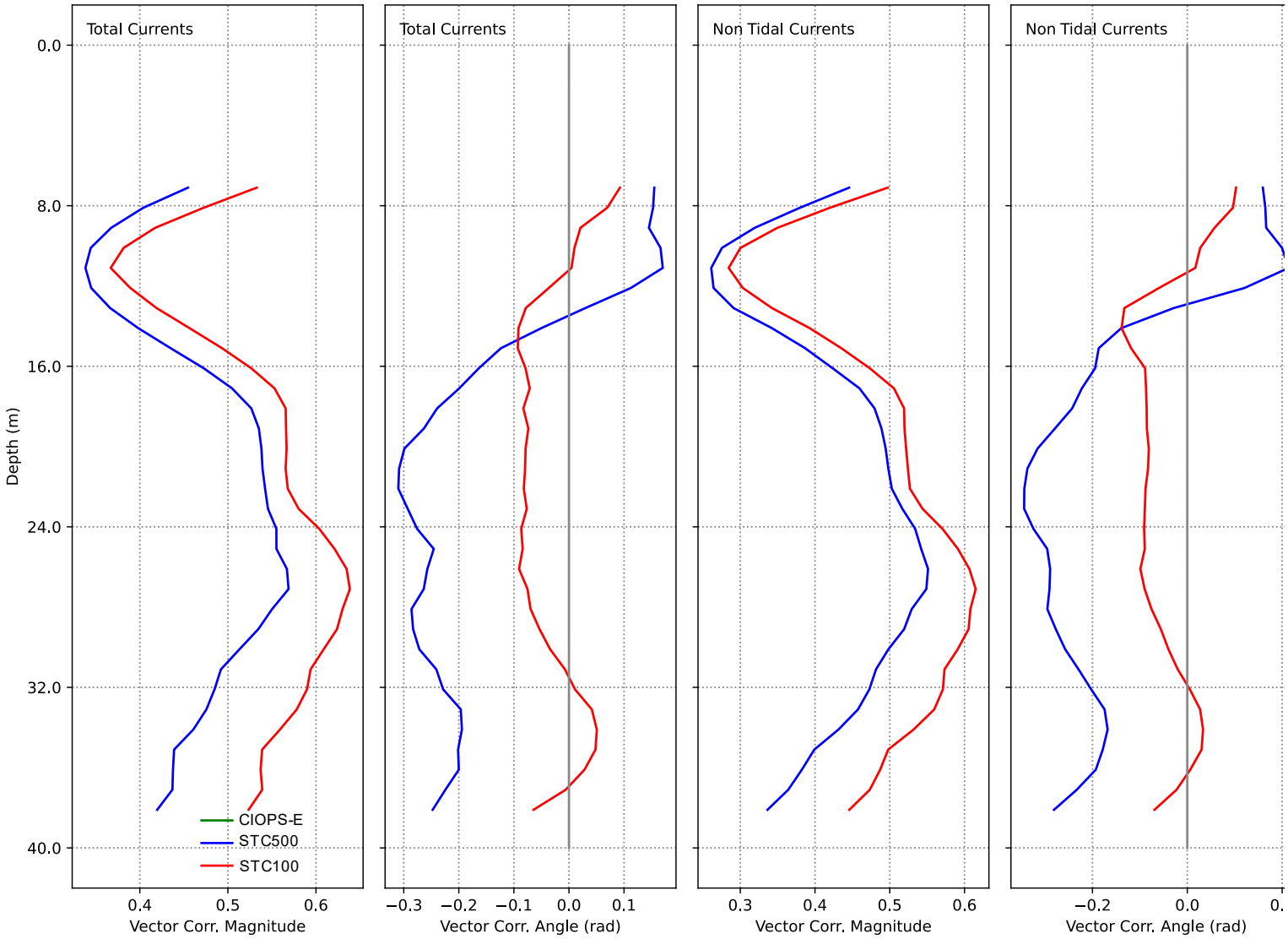

Figure 13. Profile of vector correlation at CM1_May2016.

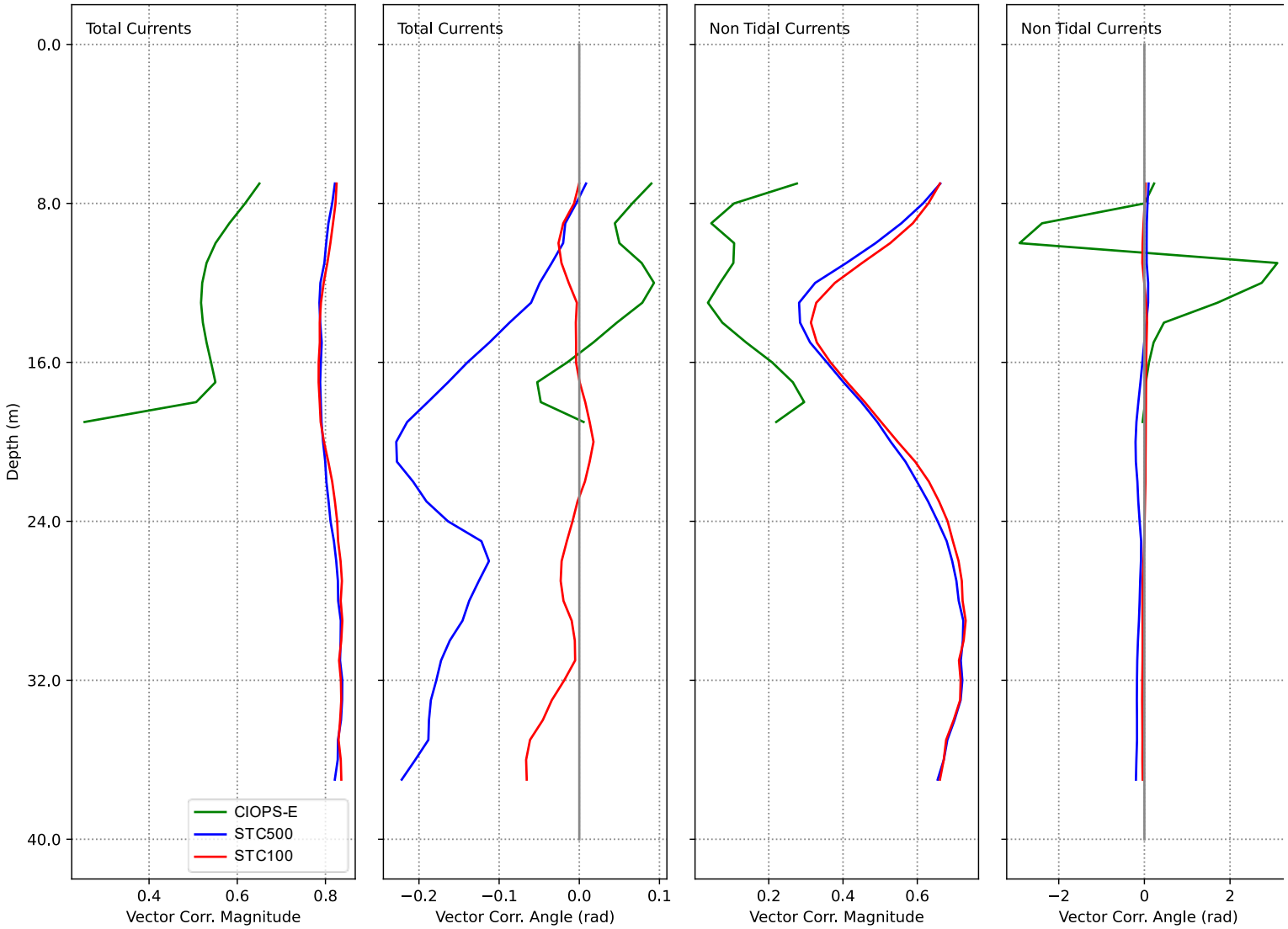

Figure 14. Profile of vector correlation at CM7_May2016.

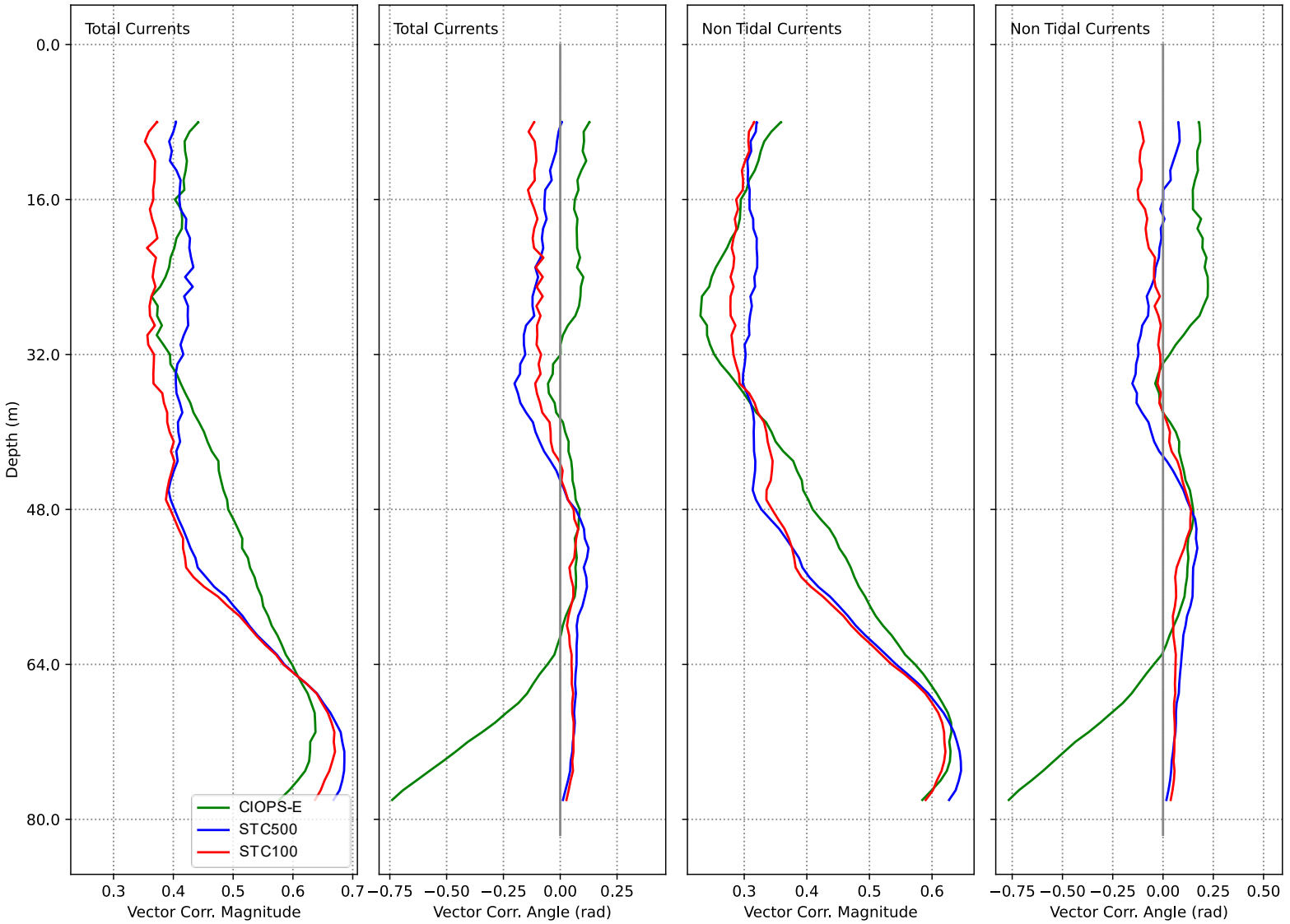

Figure 15. Profile of vector correlation at M2086.

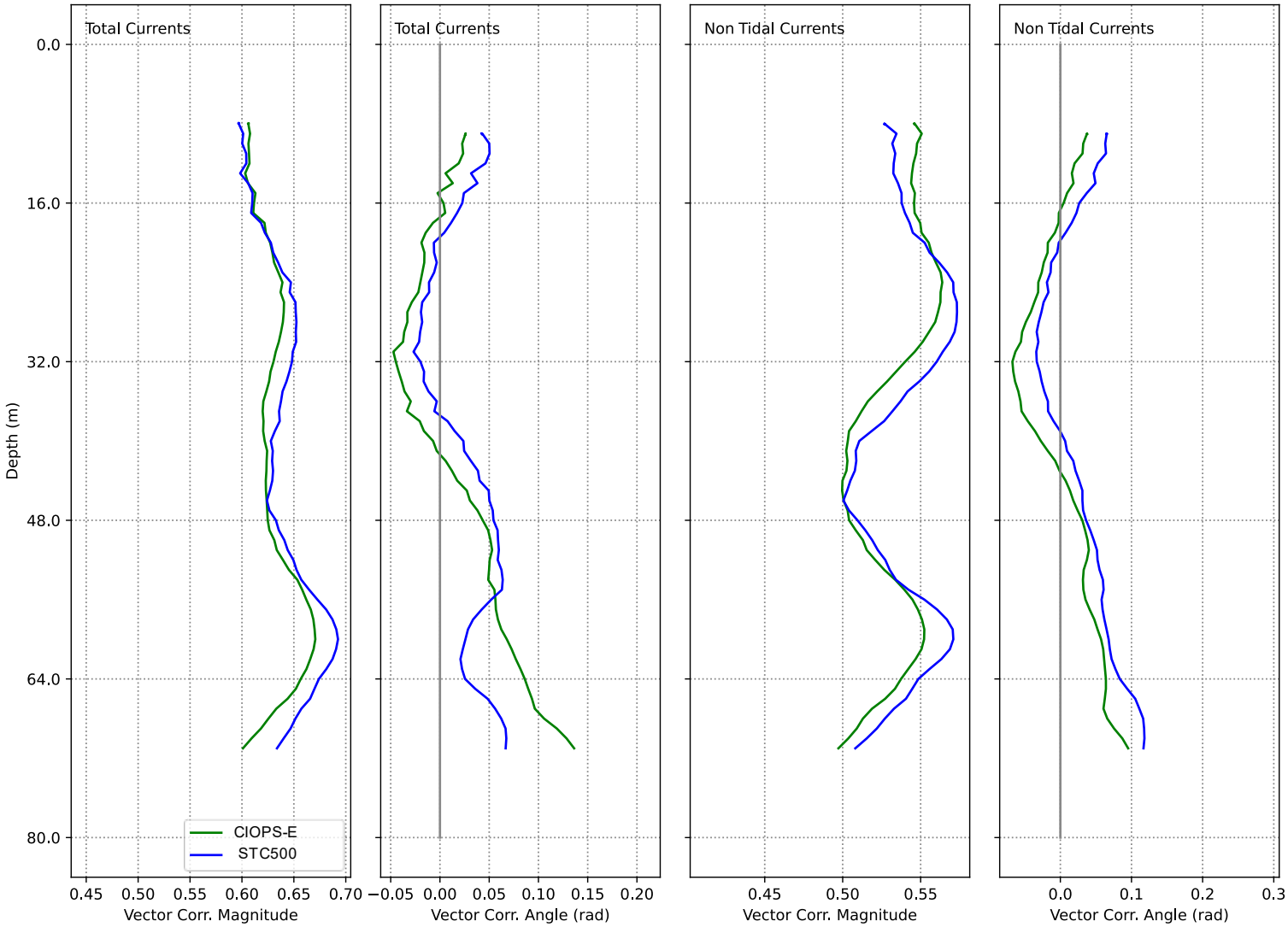

Figure 16. Profile of vector correlation at M2087.

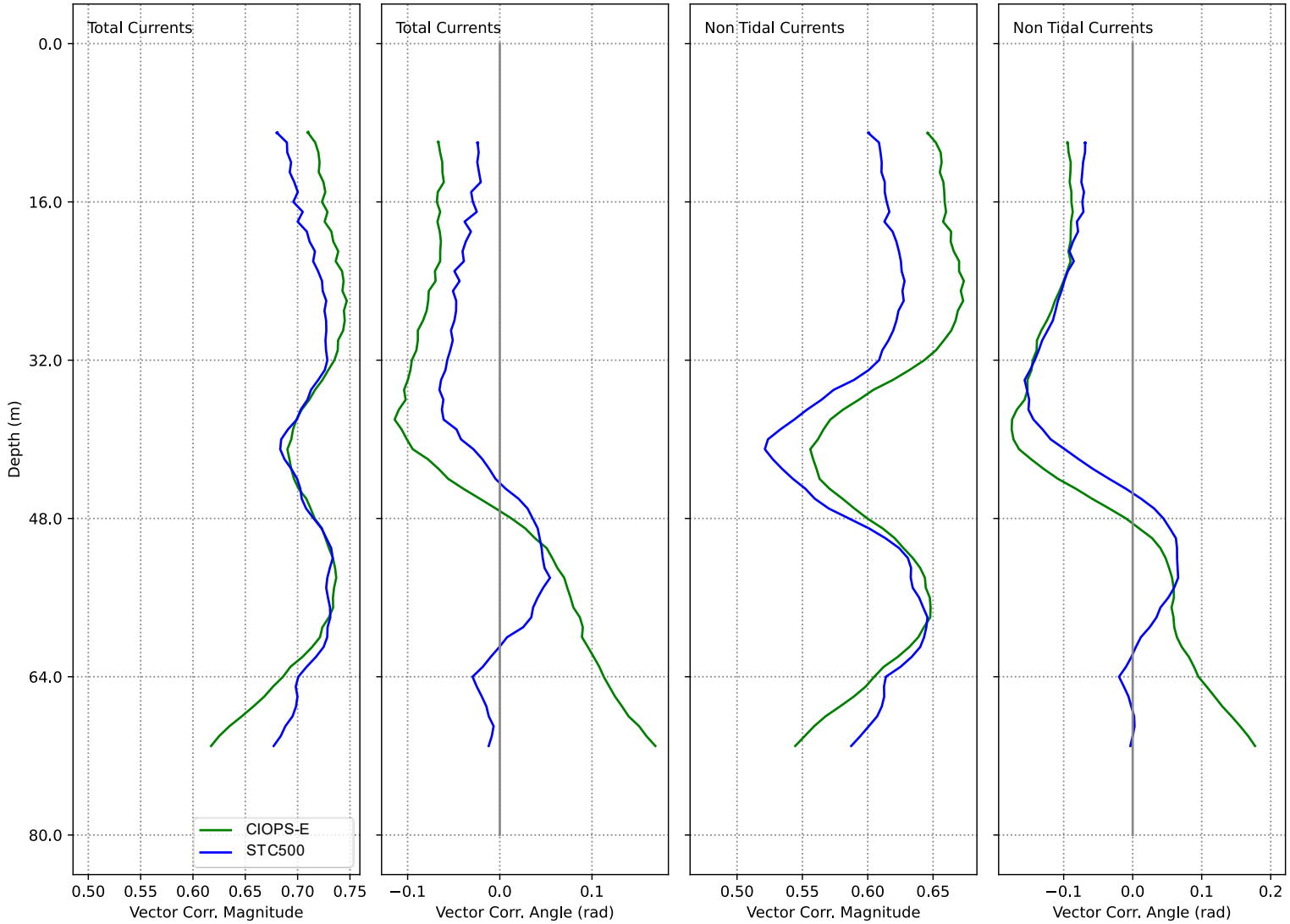

Figure 17. Profile of vector correlation at M2088.

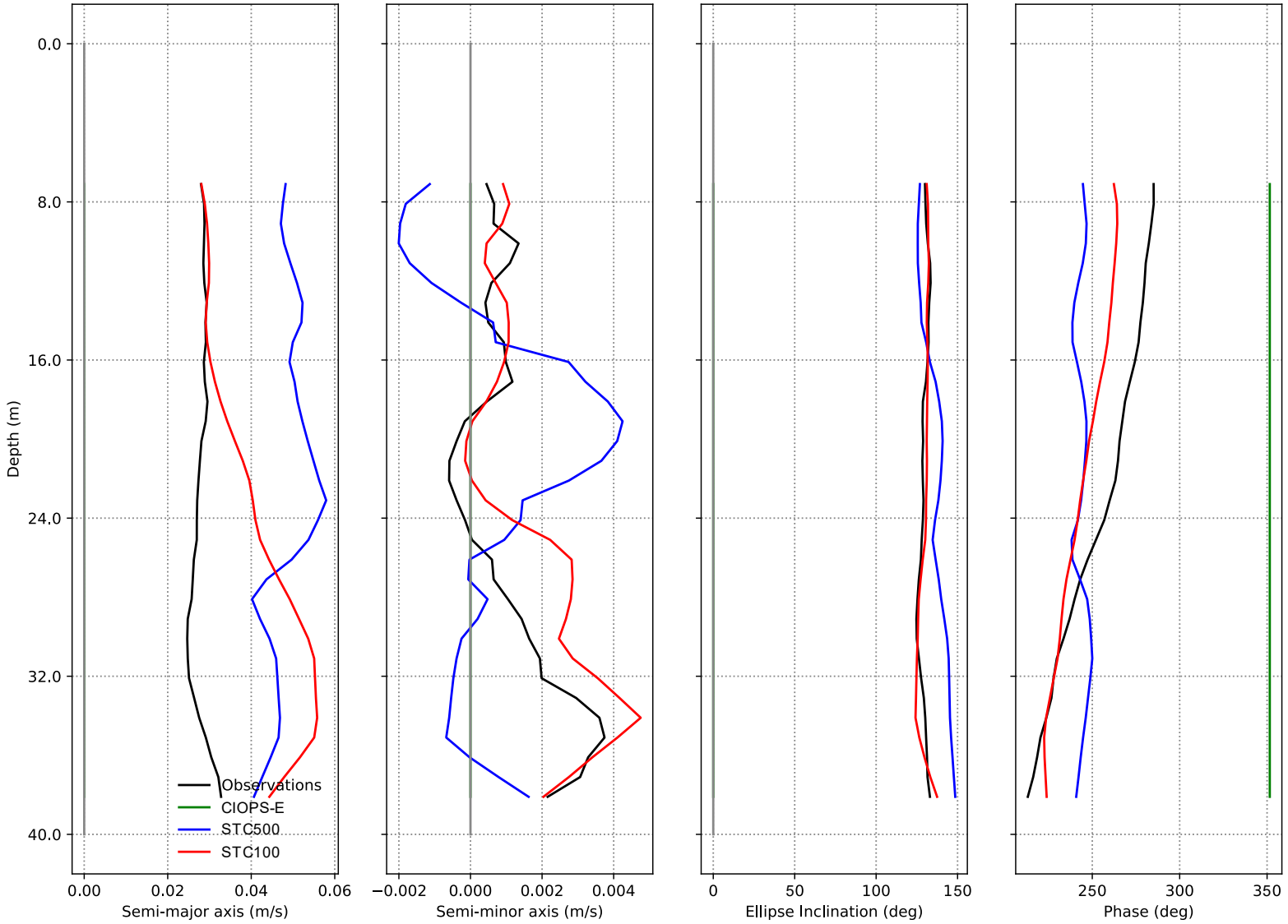

Figure 18. Profile of M2 elliptic constituents at CM1_May2016.

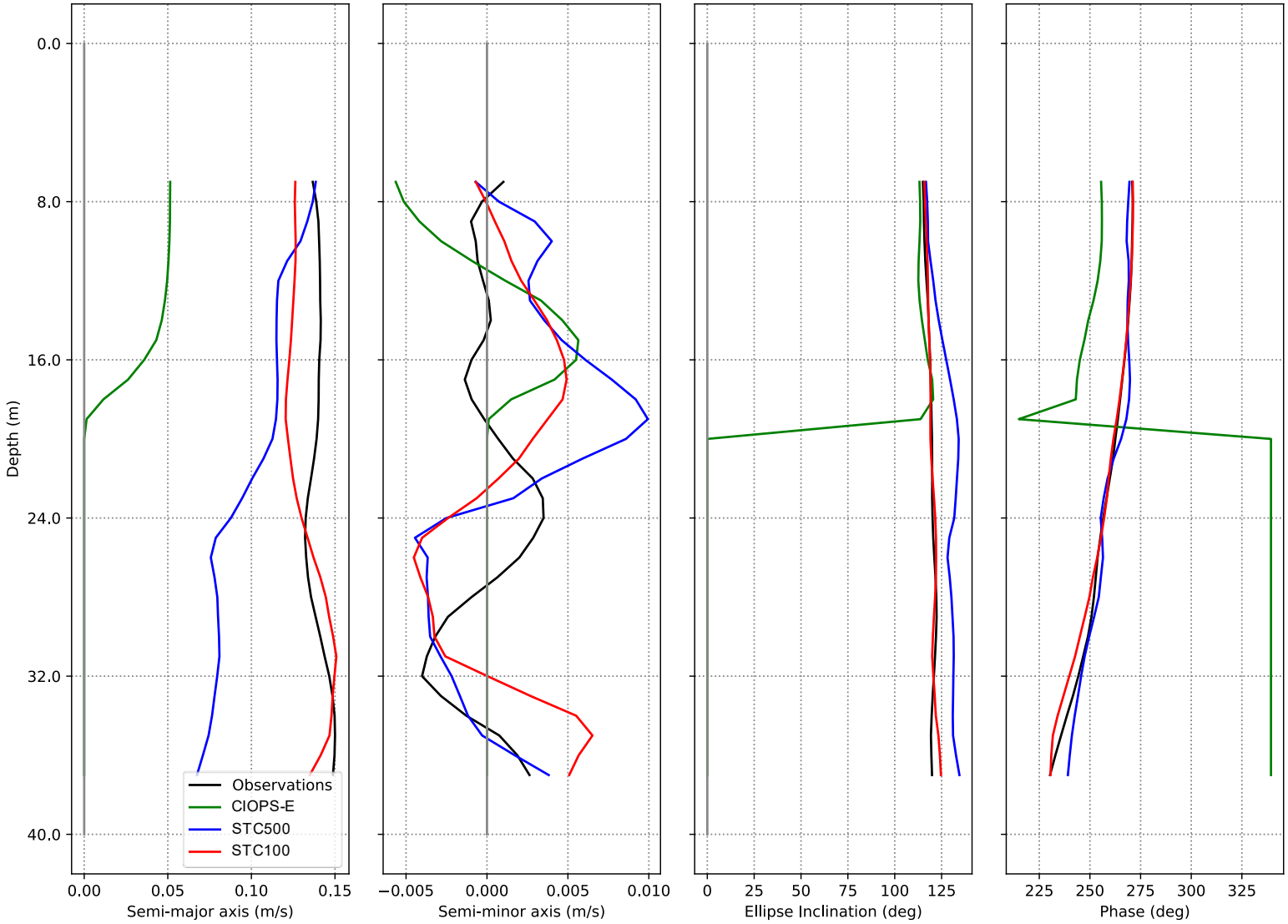

Figure 19. Profile of M2 elliptic constituents at CM7_May2016.

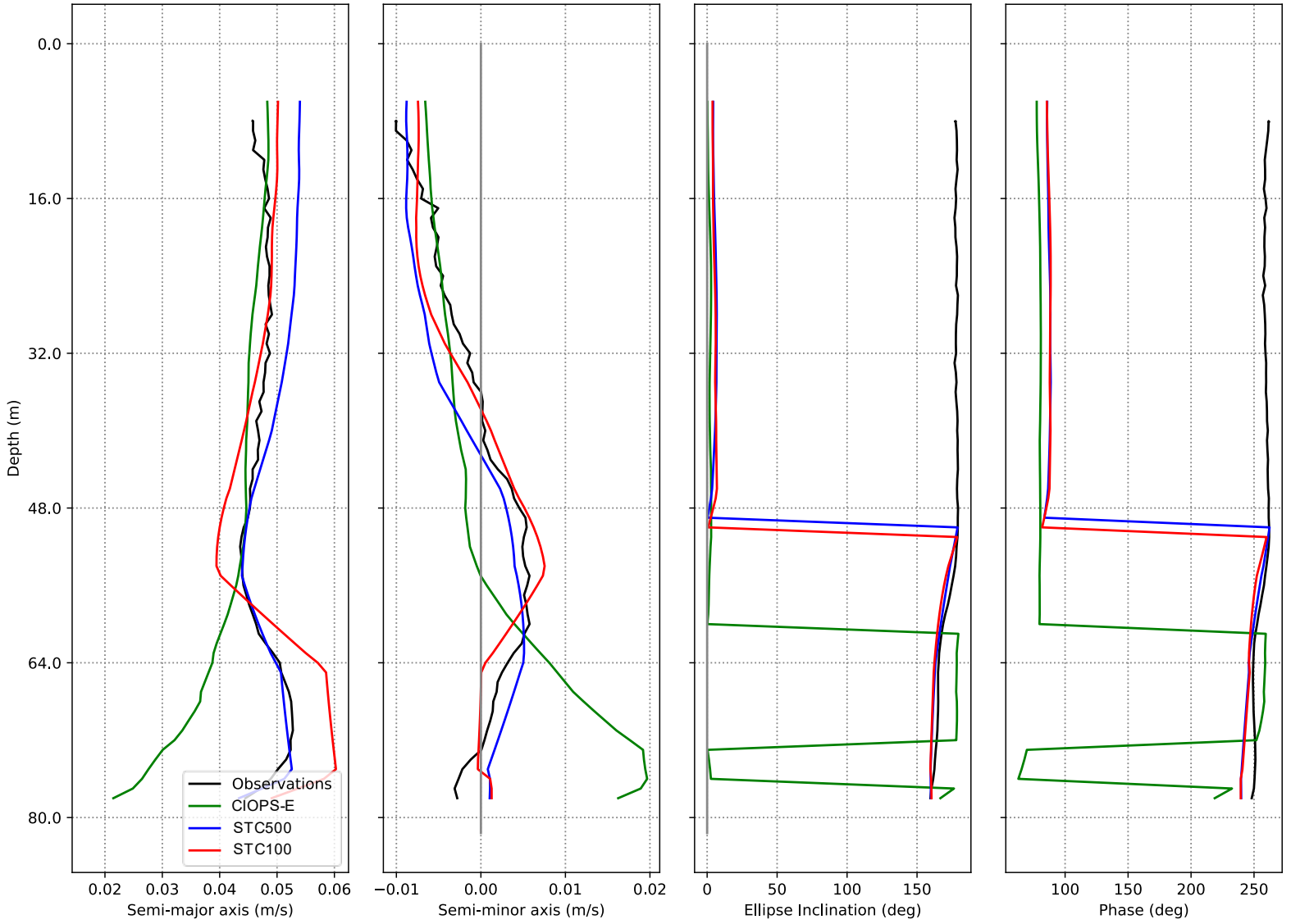

Figure 20. Profile of M2 elliptic constituents at M2086.

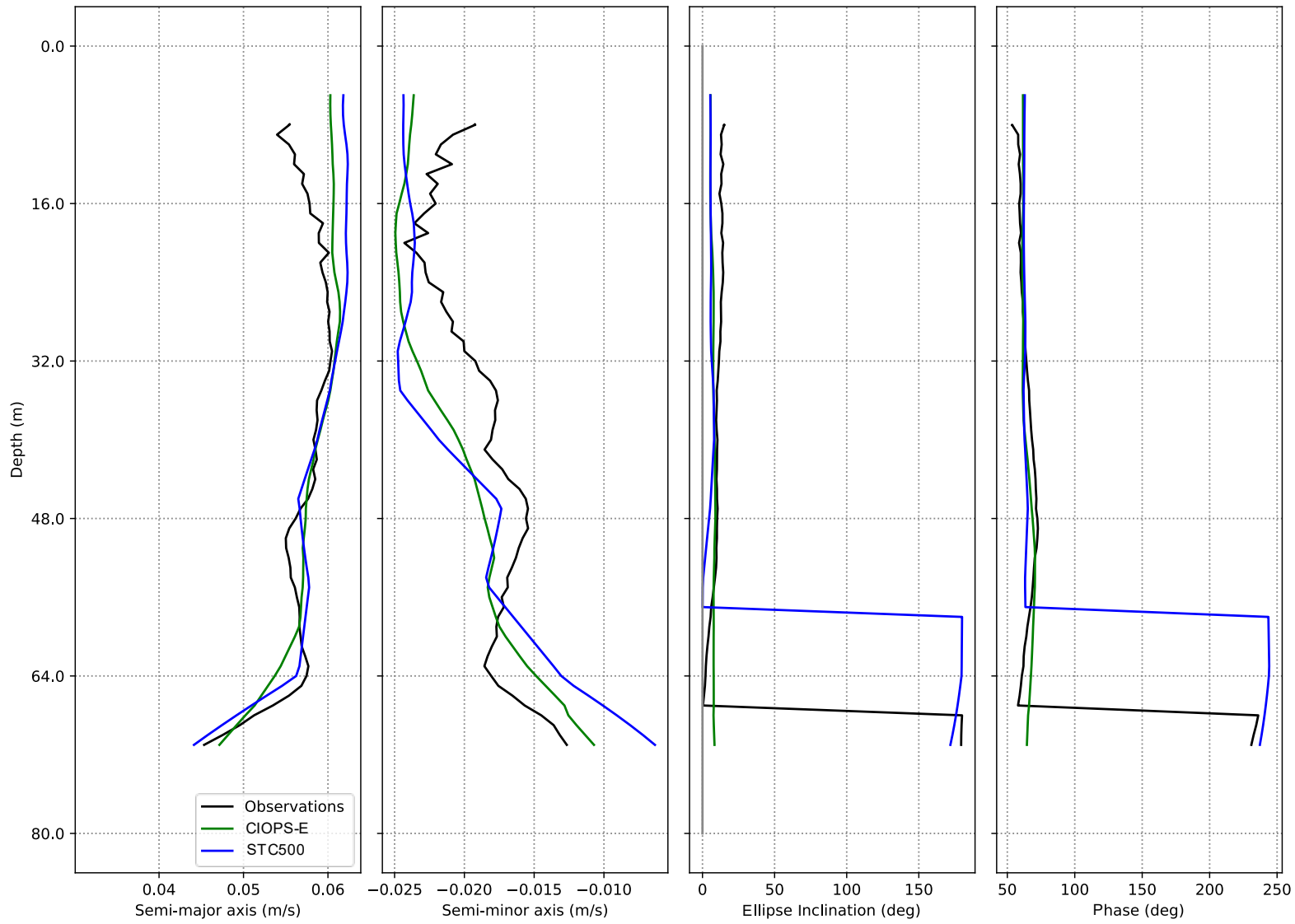

Figure 21. Profile of M2 elliptic constituents at M2087.

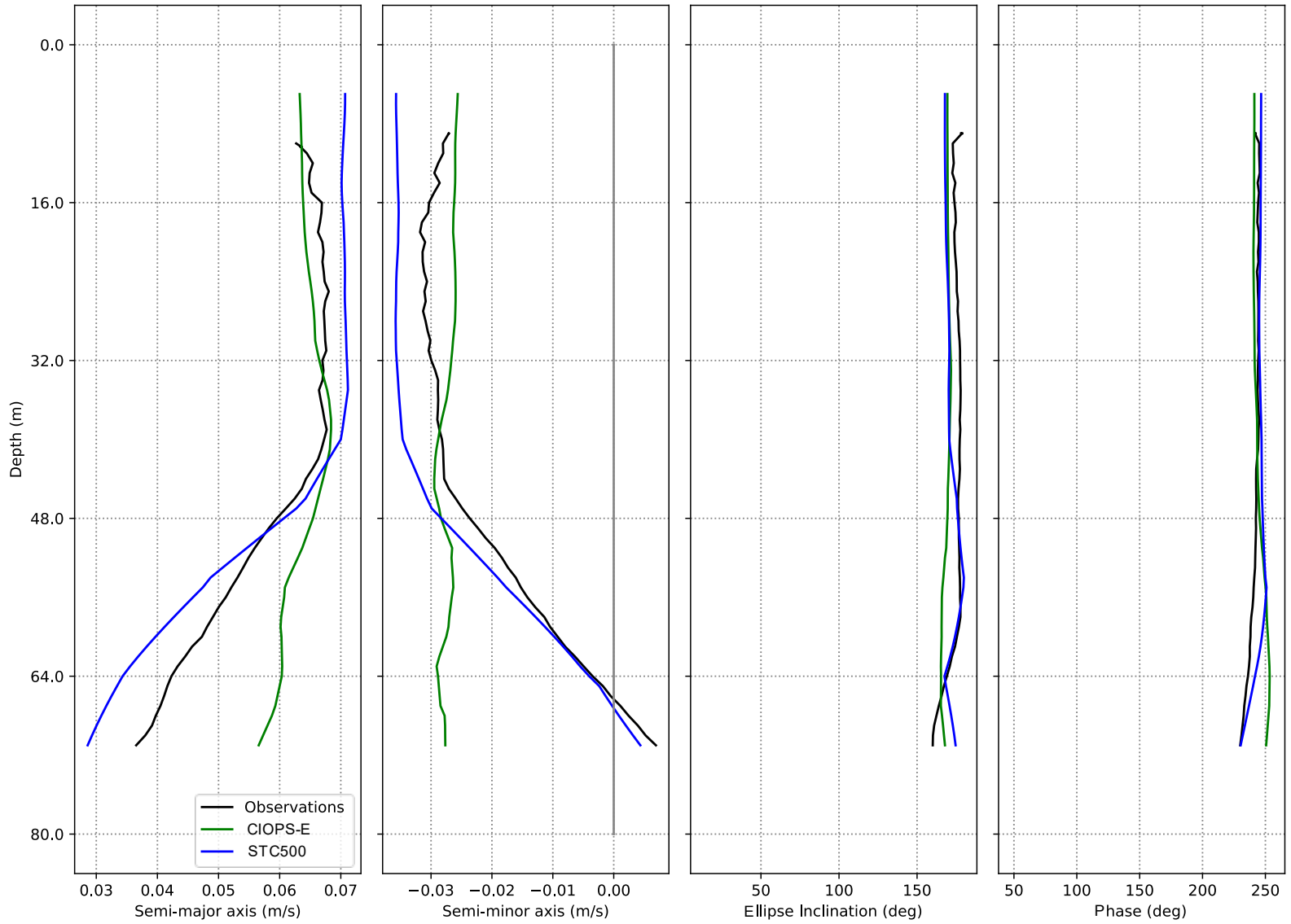

Figure 22. Profile of M2 elliptic constituents at M2088.

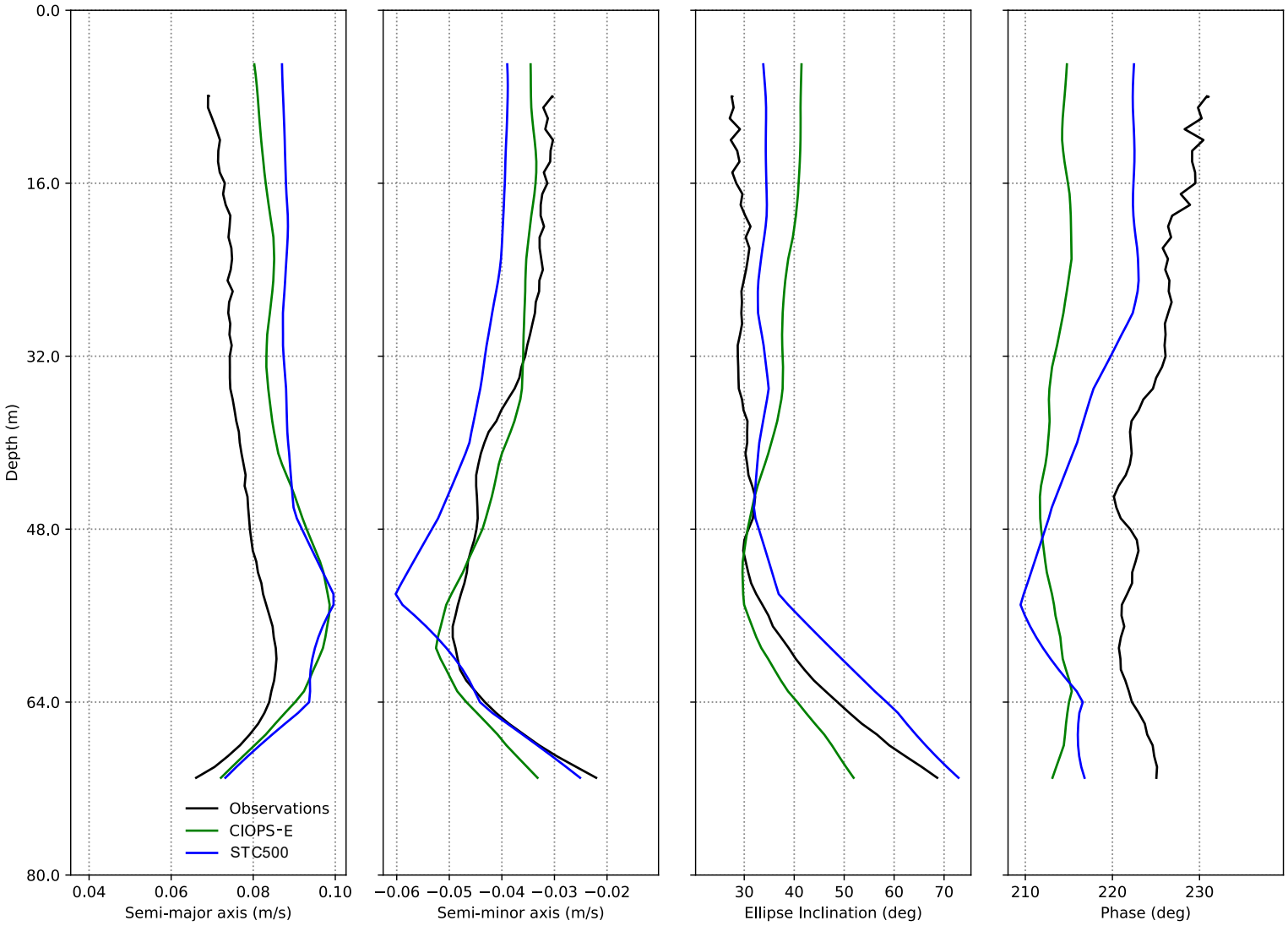

Figure 23. Profile of K1 elliptic constituents at M2087.

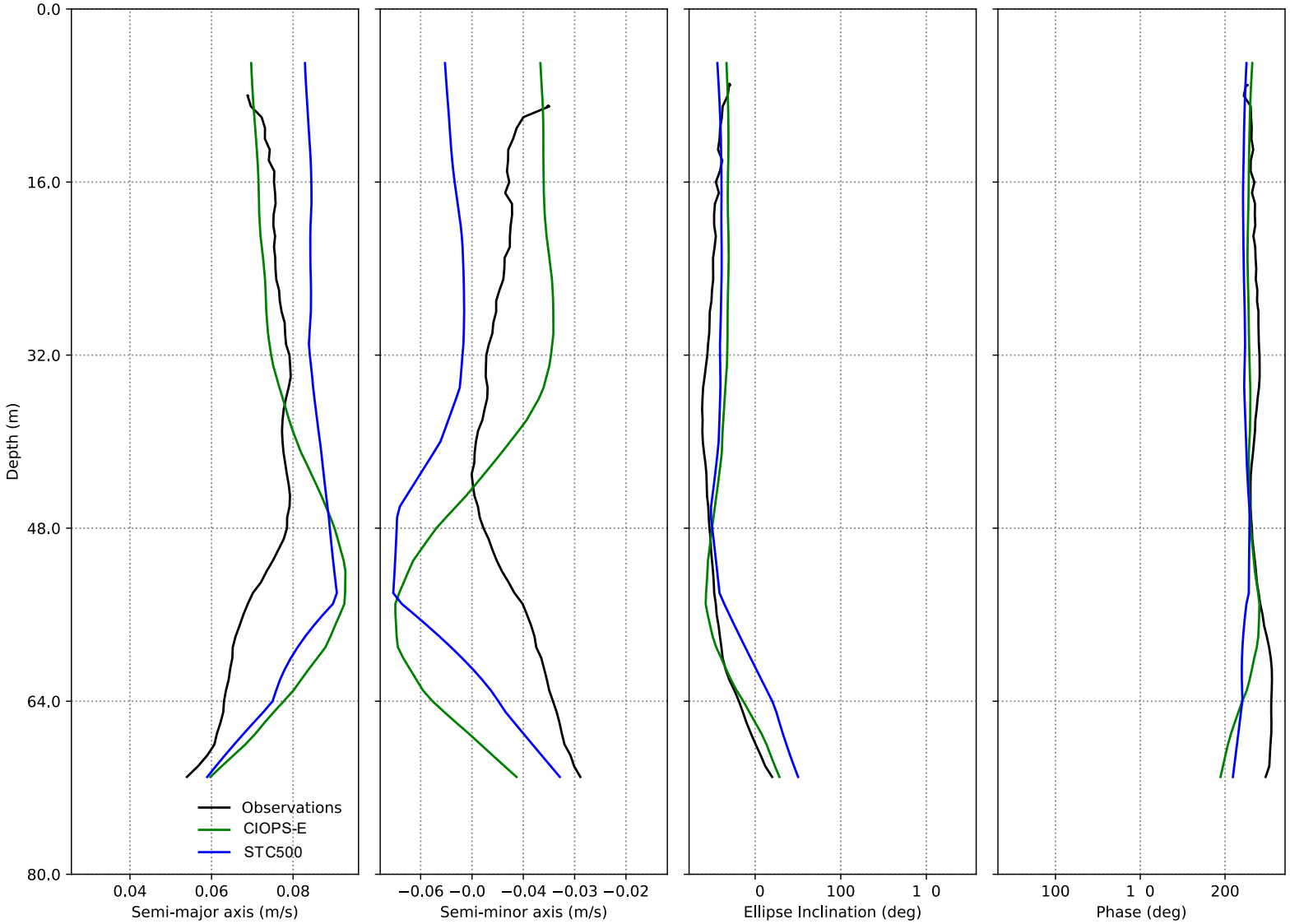

Figure 24. Profile of K1 elliptic constituents at M2088.

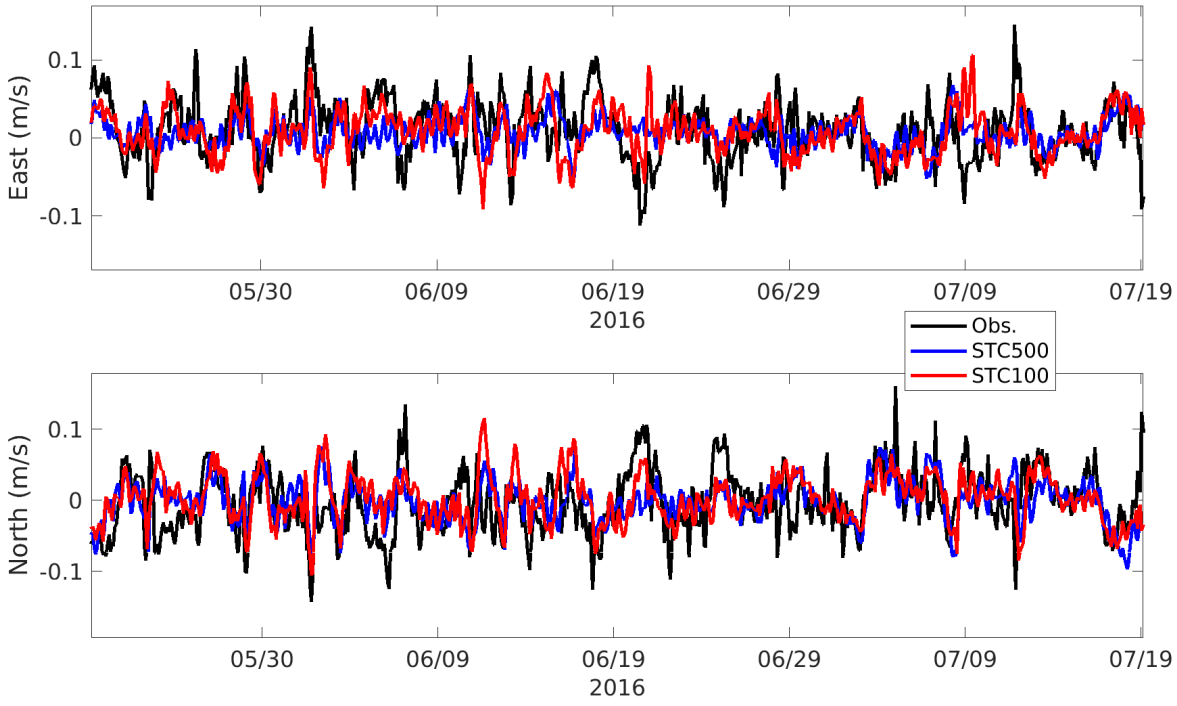

Figure 25. Non-tidal current at depth of 10 m from CM1_May2016.

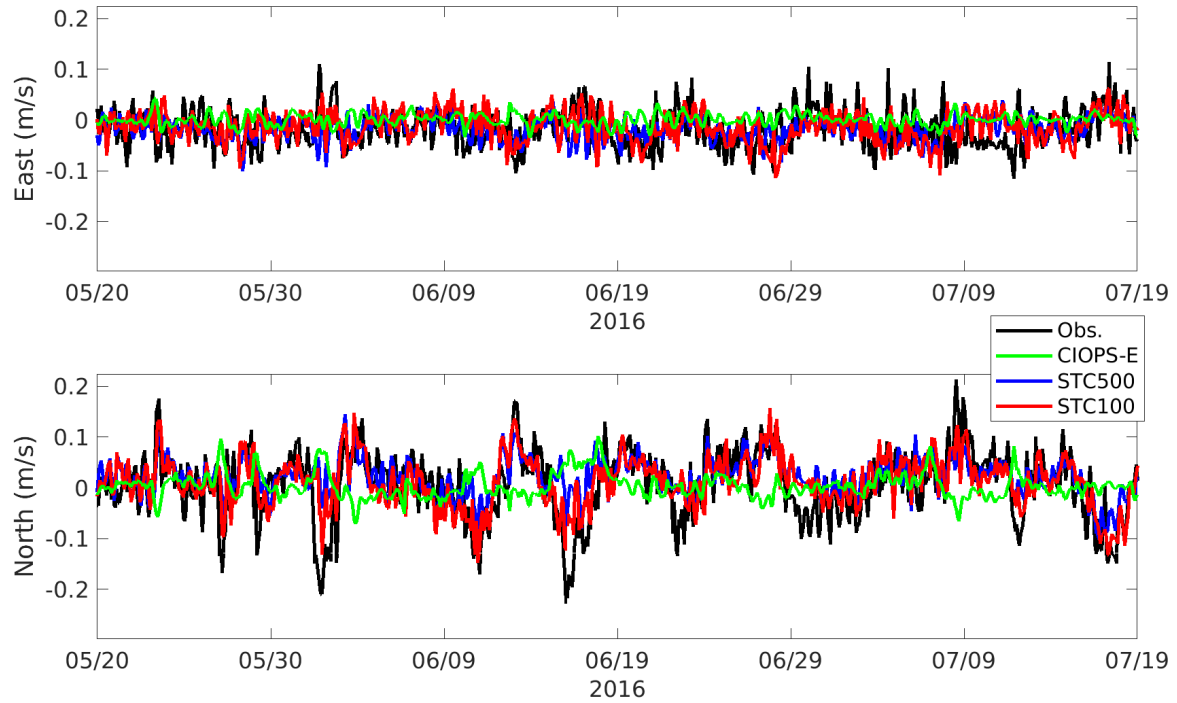

Figure 26. Non-tidal current at depth of 10 m from CM7_May2016.

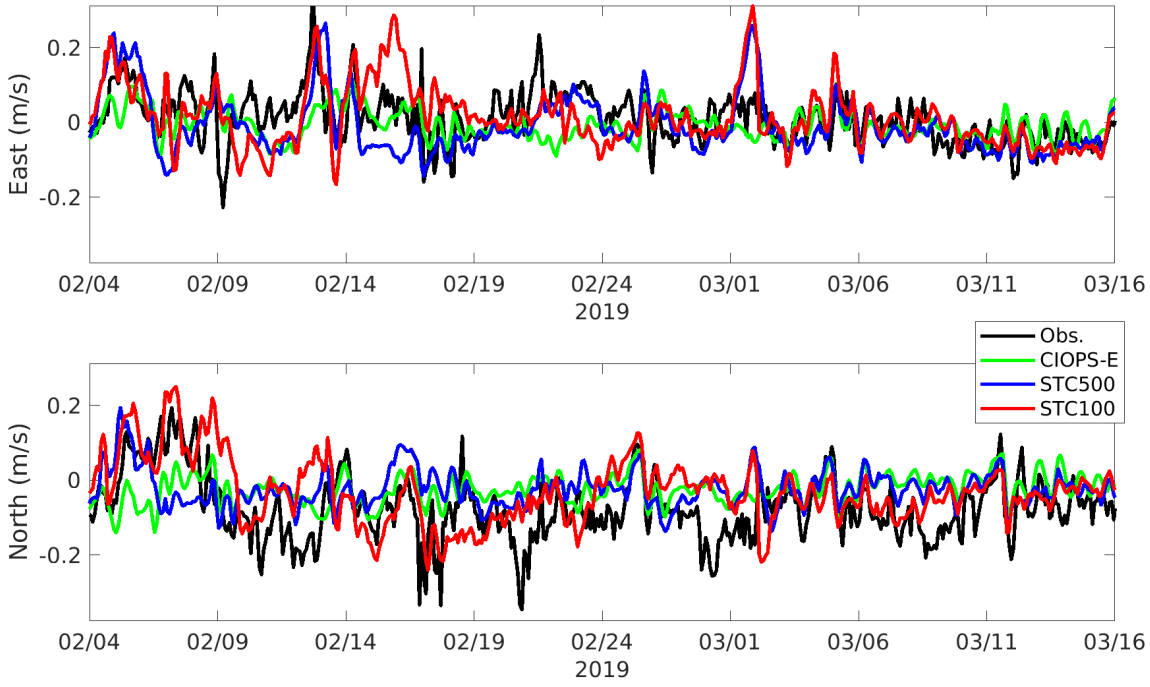

Figure 27. Non-tidal current at depth of 10 m from M2086.

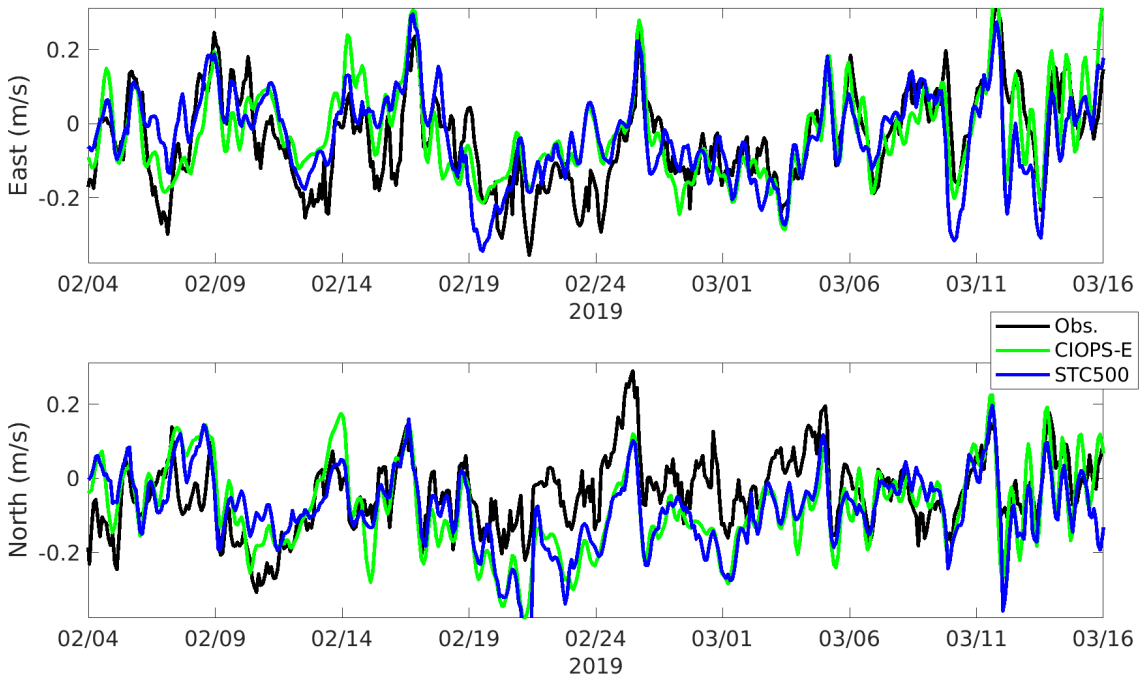

Figure 28. Non-tidal current at depth of 10 m from M2087.

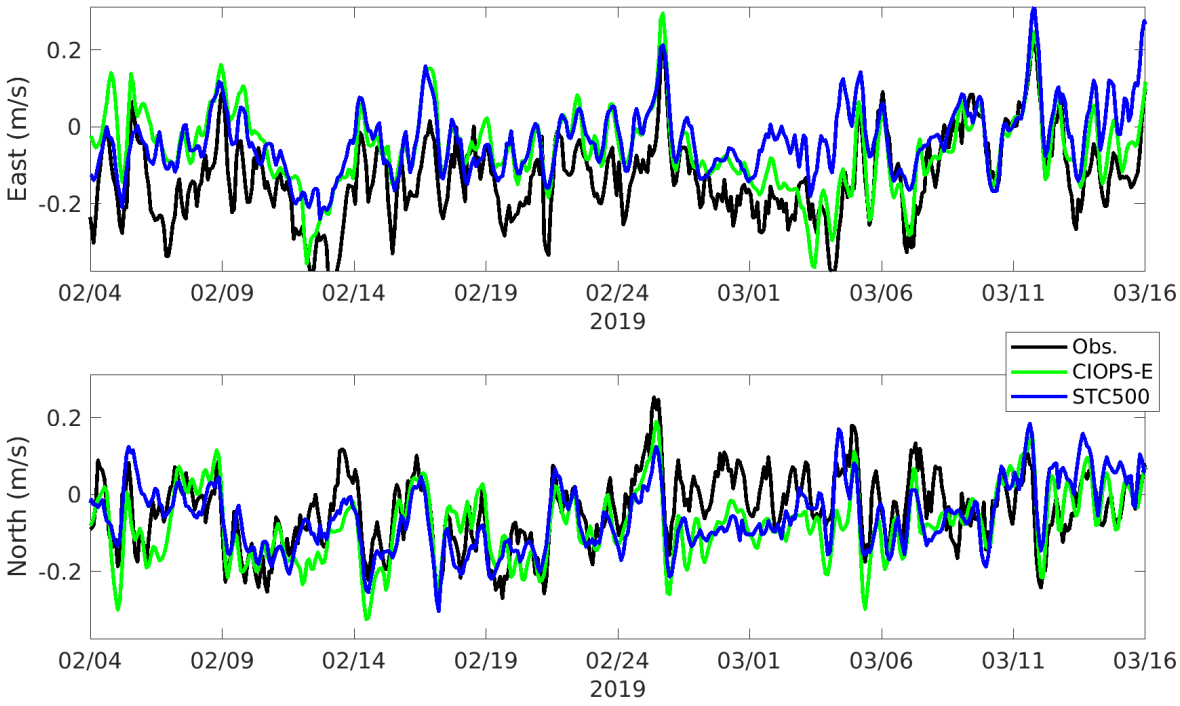

Figure 29. Non-tidal current at depth of 10 m from M2088.

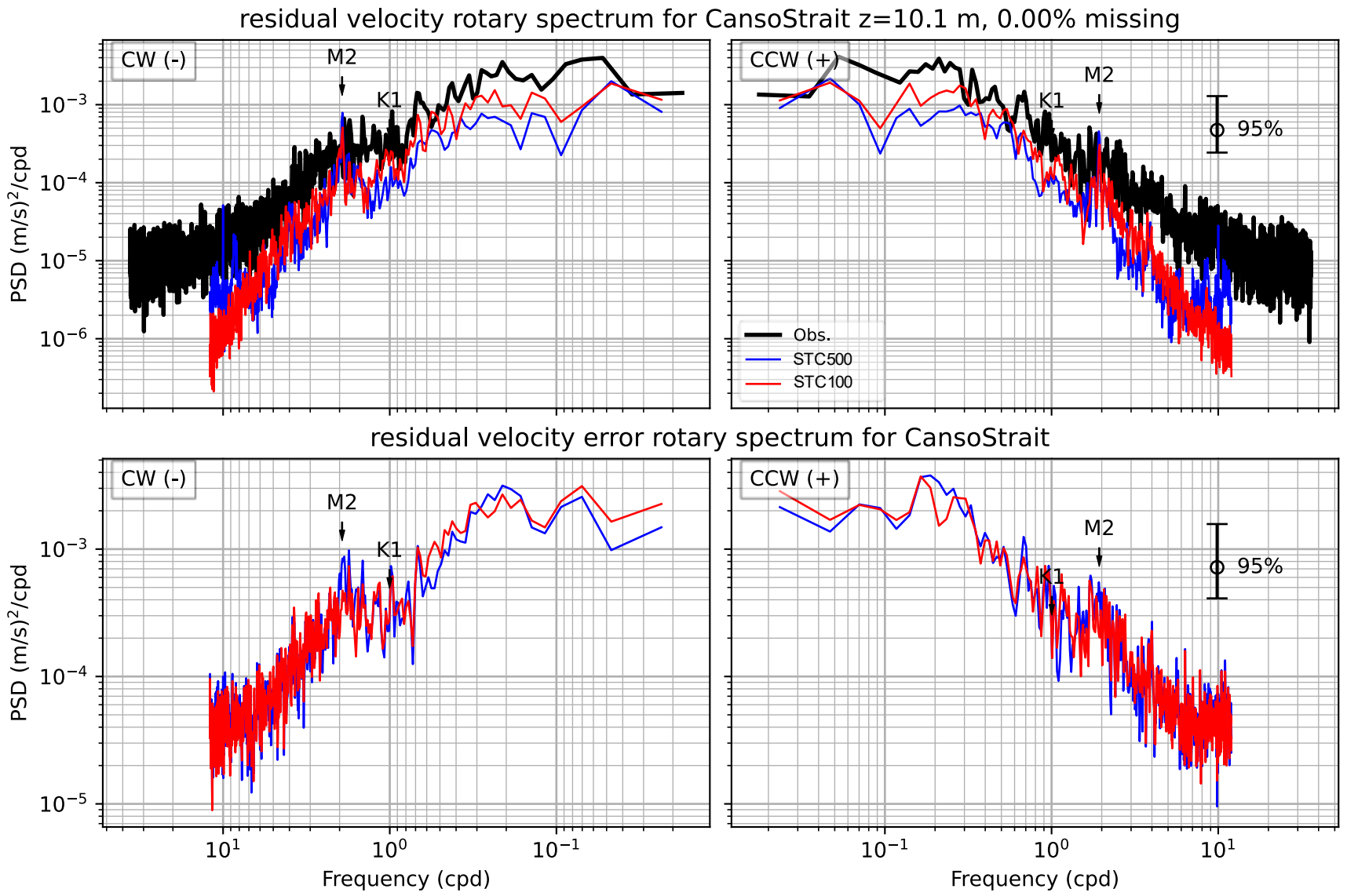

Figure 30. Non-tidal rotary power spectra from CM1_May2016 at depth of 10 m.

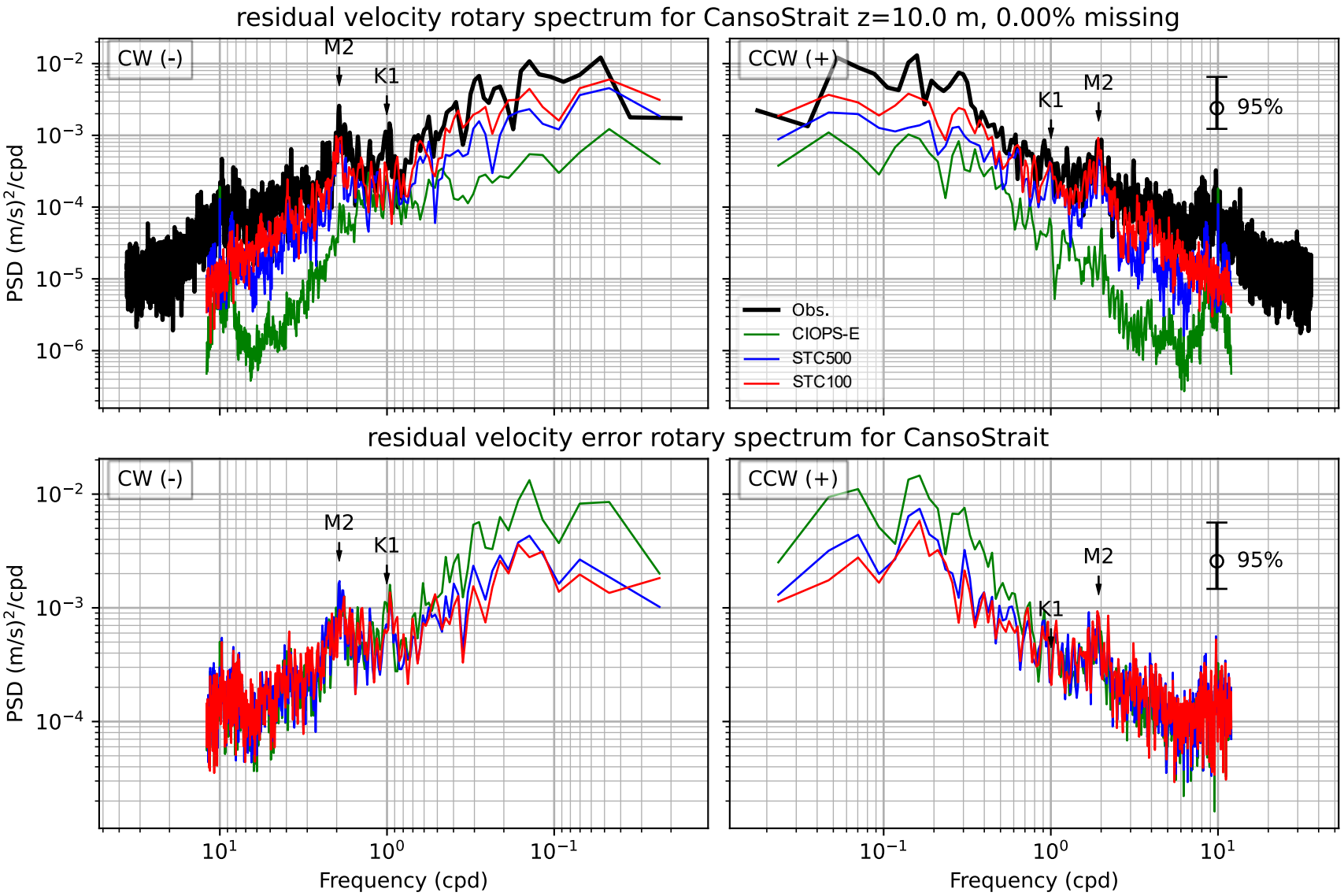

Figure 31. Non-tidal rotary power spectra from CM7_May2016 at depth of 10 m.

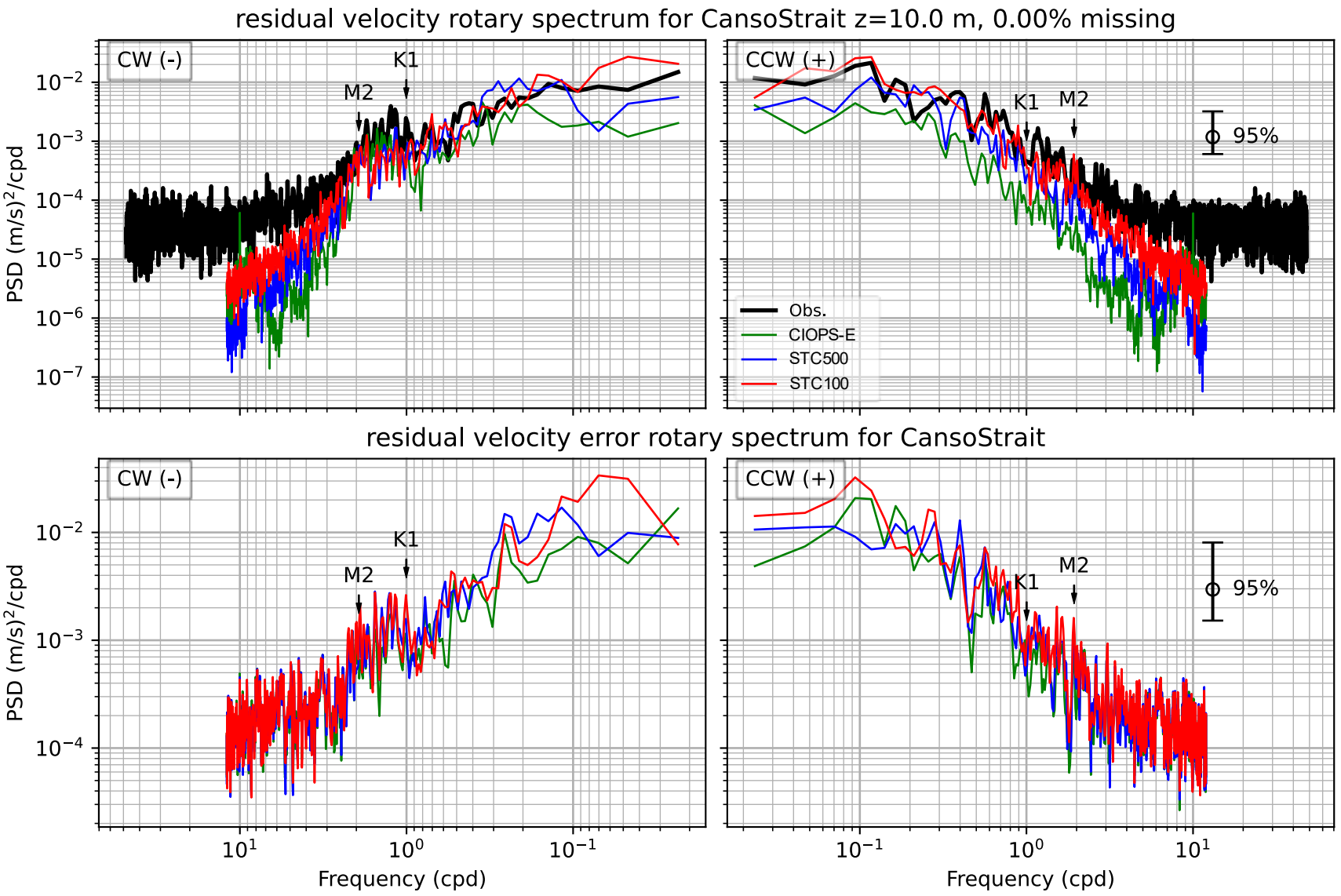

Figure 32. Non-tidal rotary power spectra from M2086 at depth of 10 m.

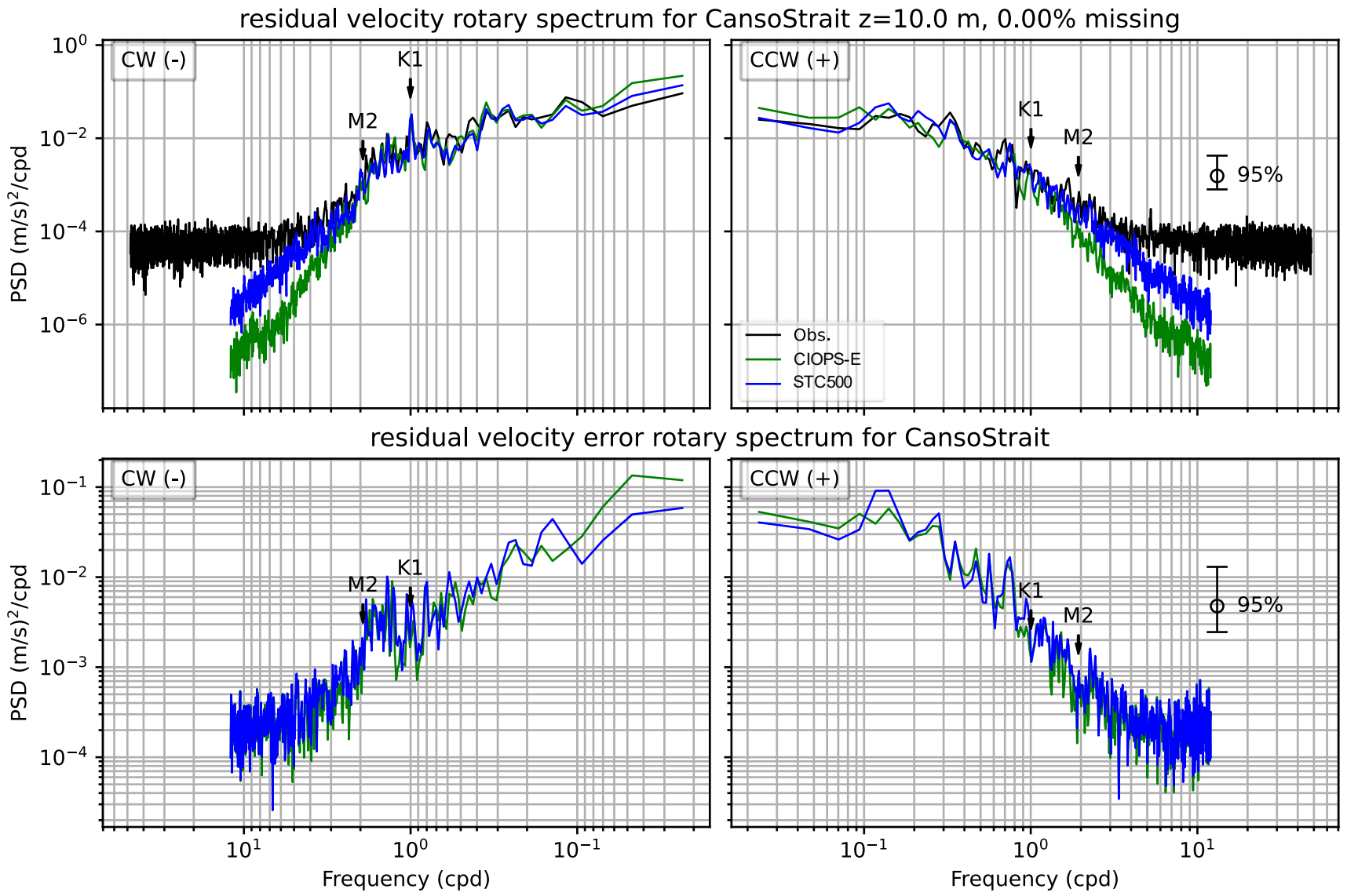

Figure 33. Non-tidal rotary power spectra from M2087 at depth of 10 m.

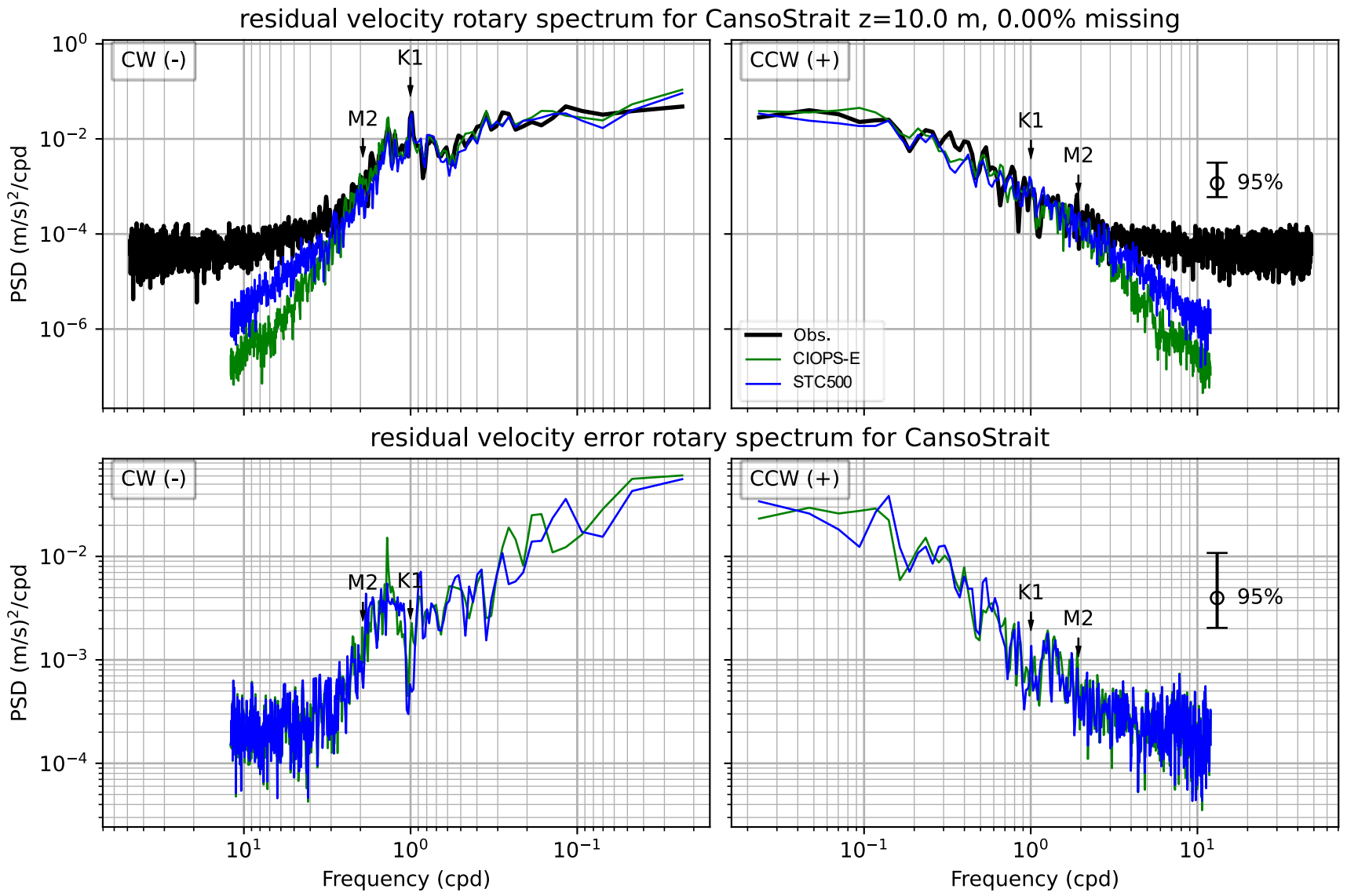

Figure 34. Non-tidal rotary power spectra from M2088 at depth of 10 m.

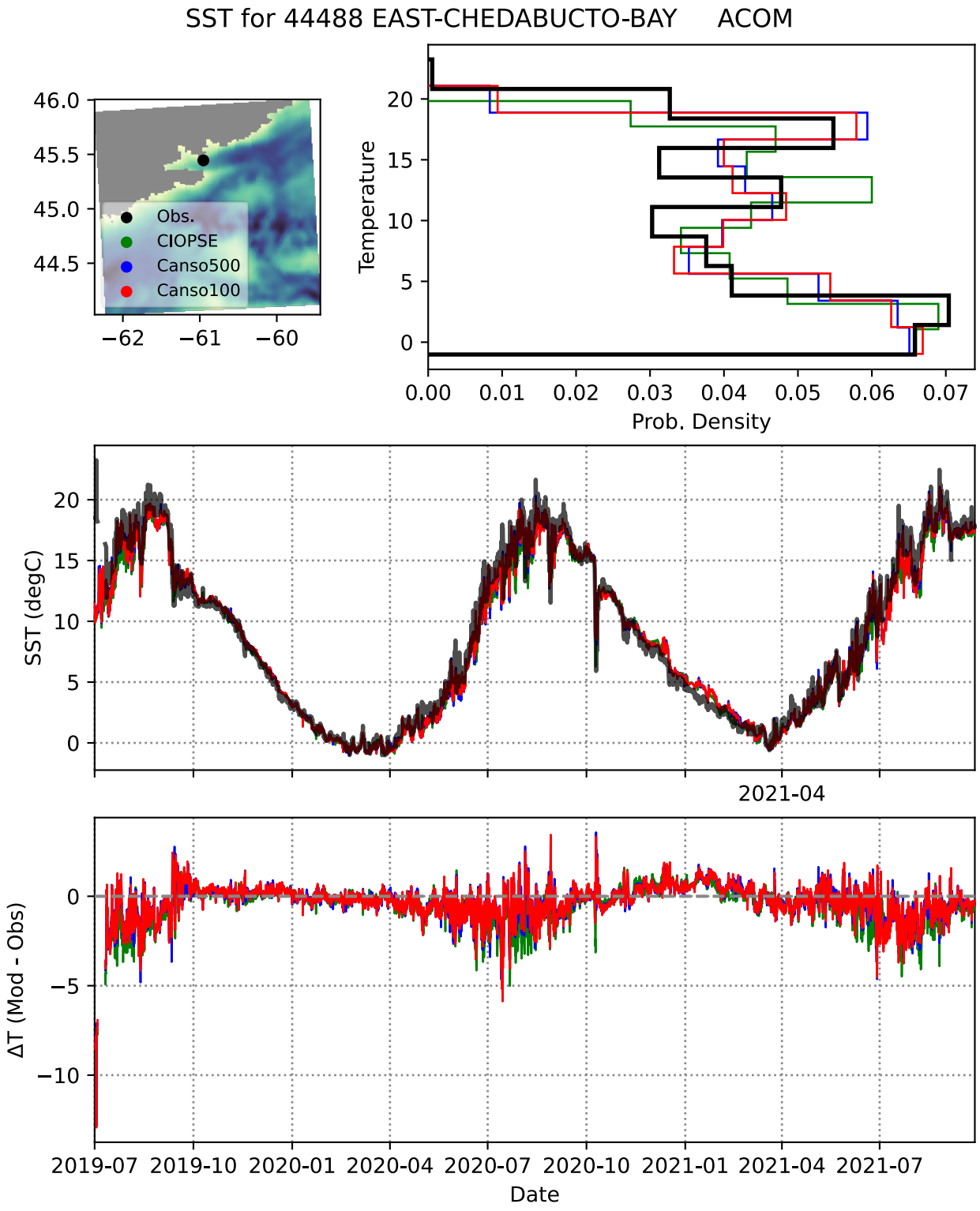

Figure 35. Observed and modelled SST at east station.

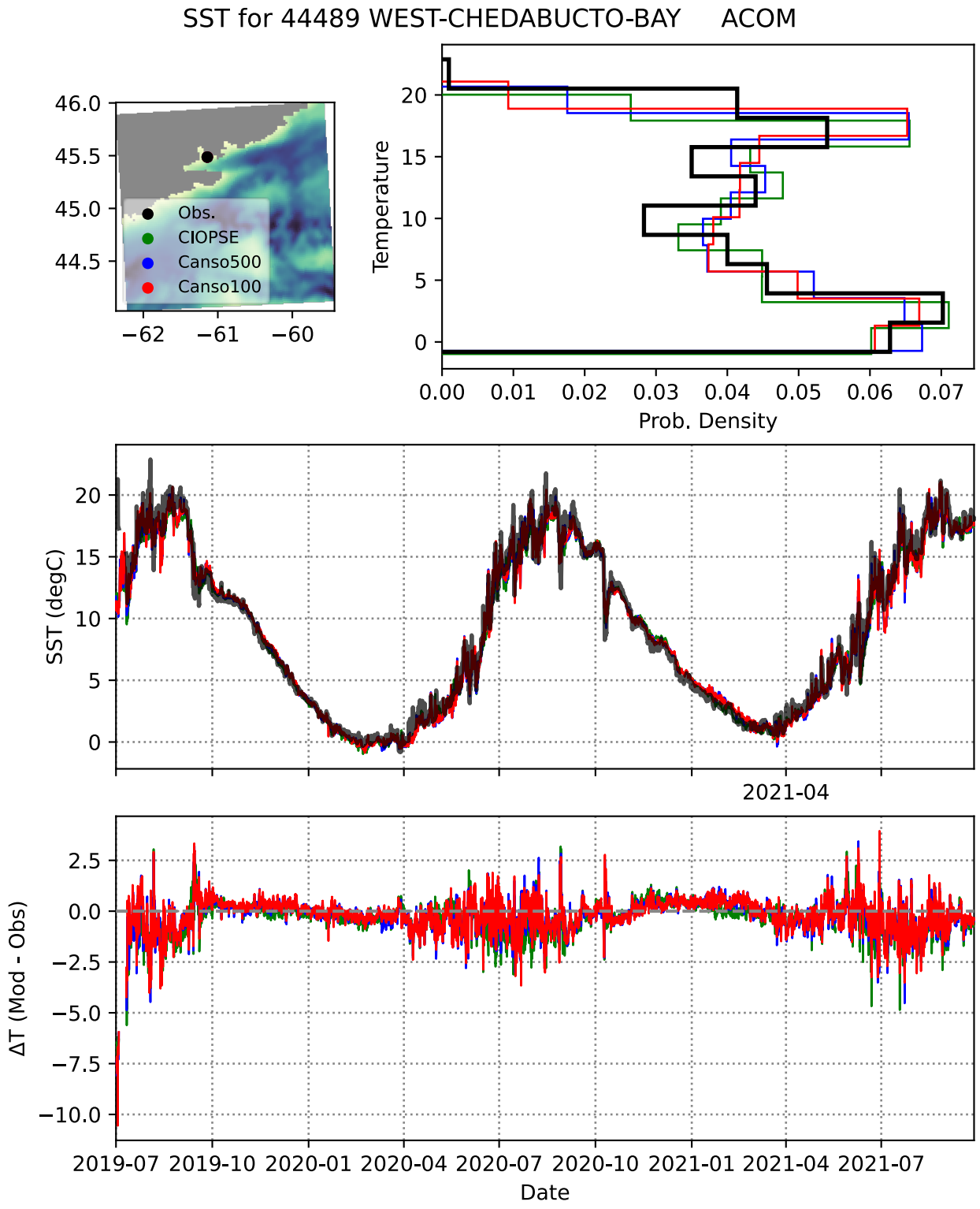

Figure 36. Observed and modelled SST at west station.

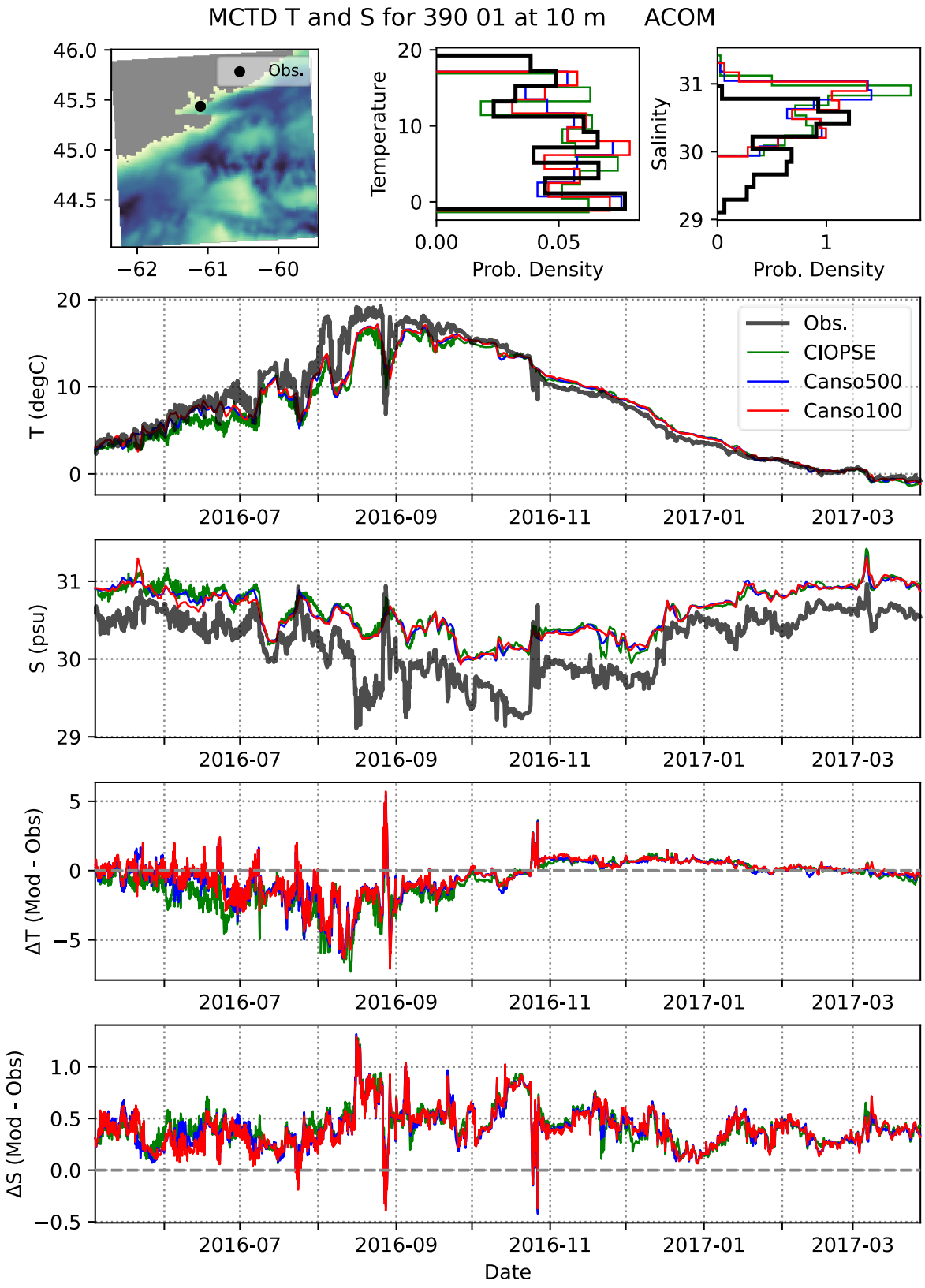

Figure 37. Observed and modelled T-S at CB_10m.

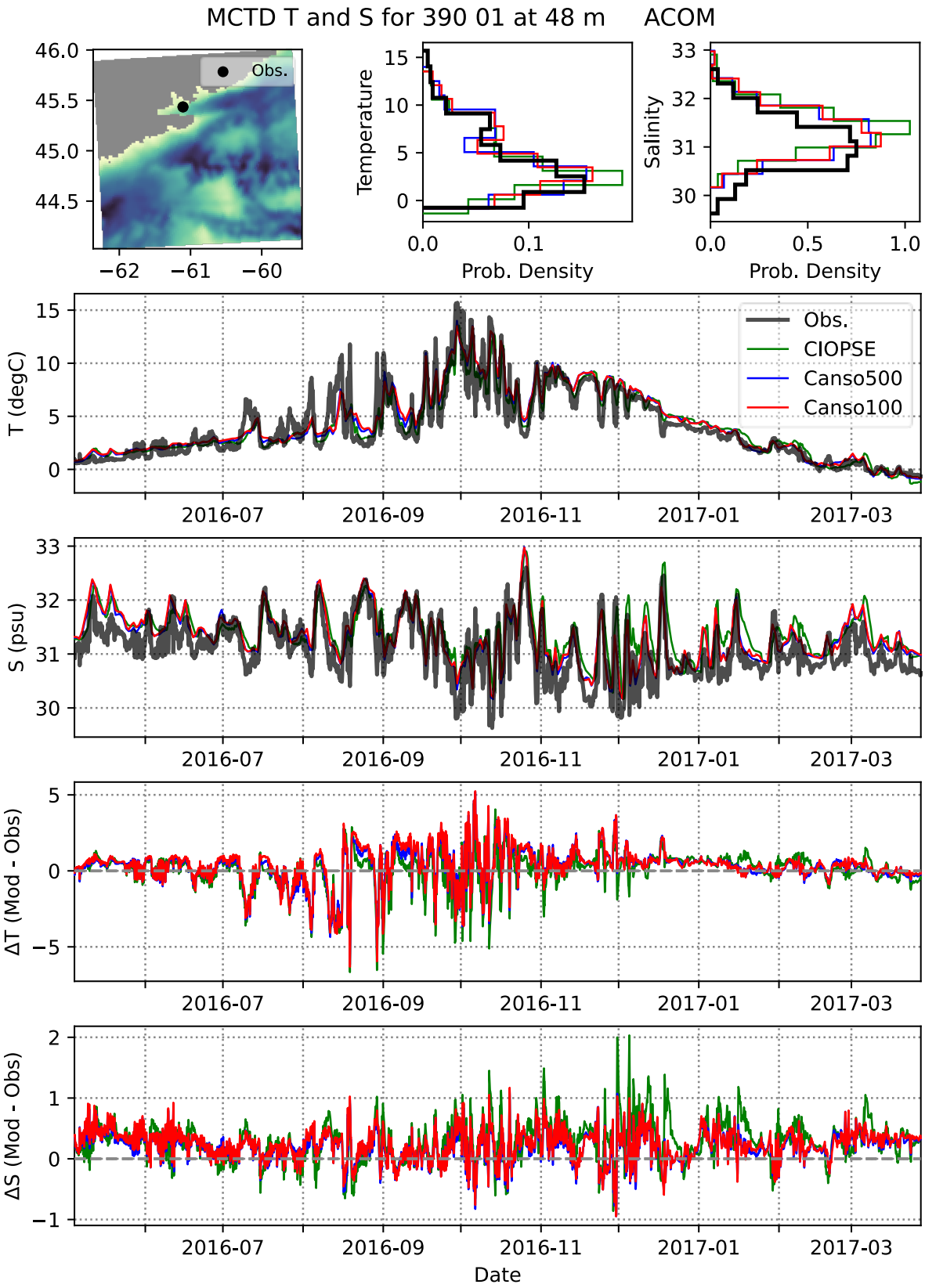

Figure 38. Observed and modelled T-S at CB_48m.

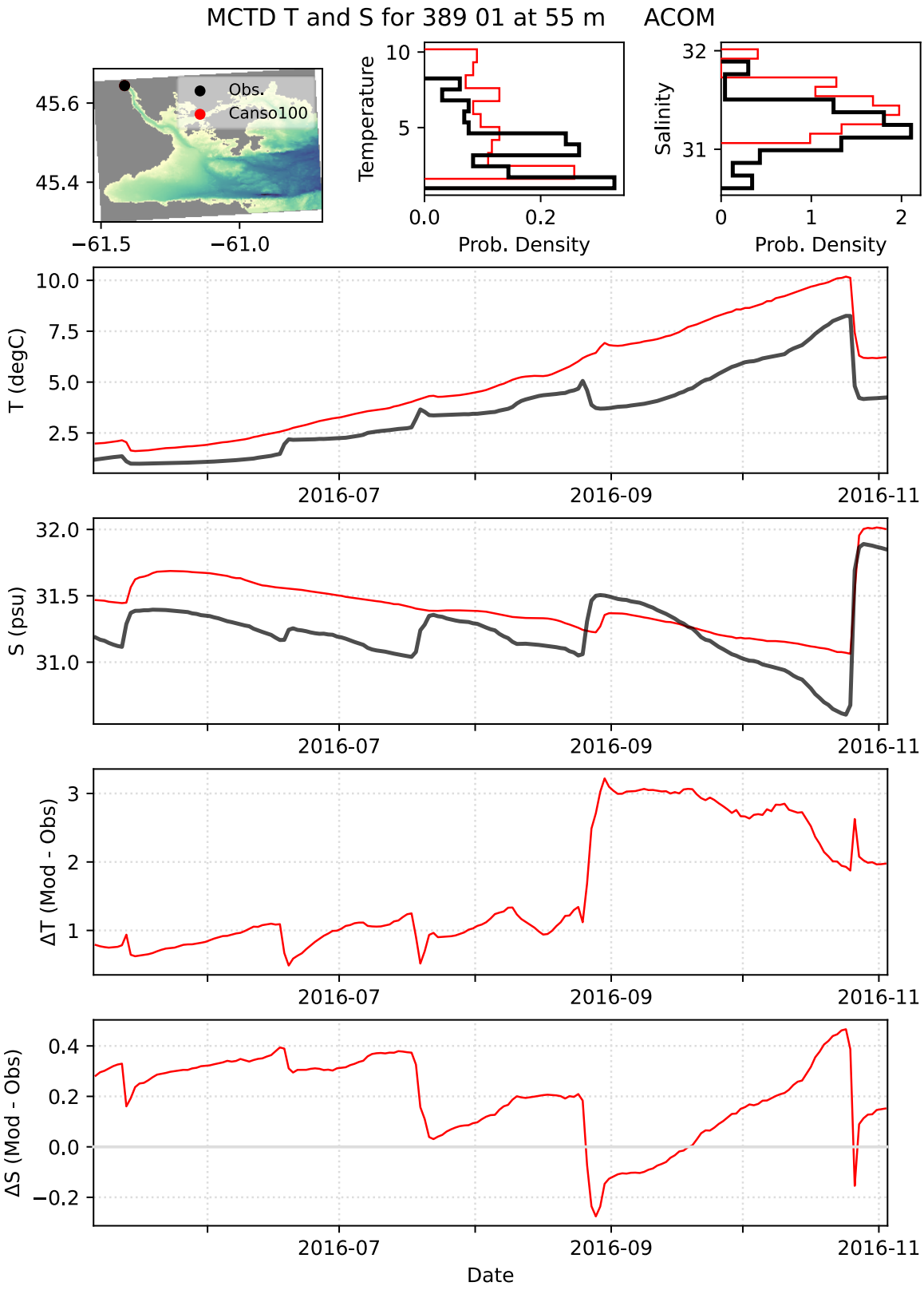

Figure 39. Observed and modelled T-S at CW_55m.

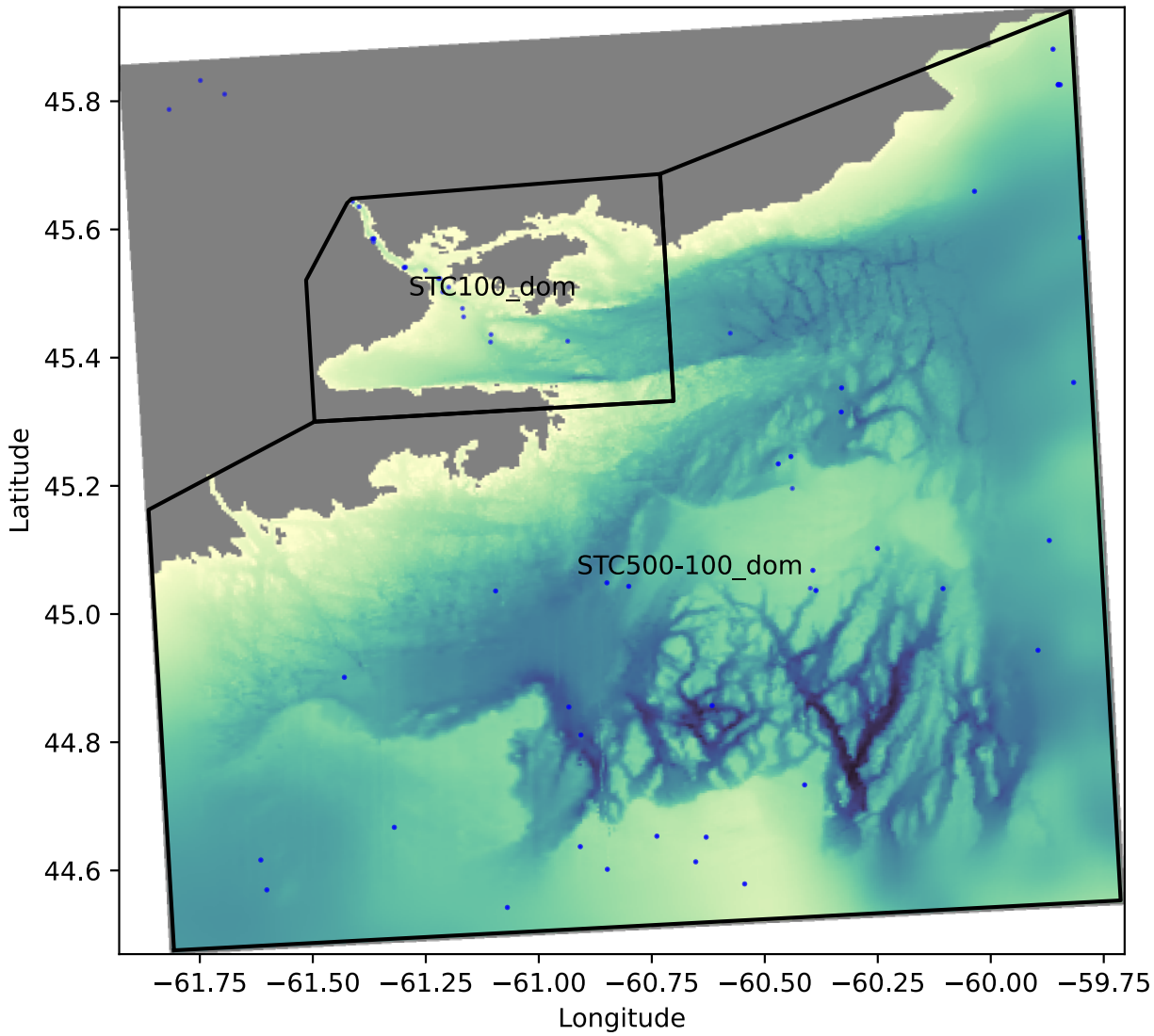

Figure 40. Locations of CTD casts. Black lines show regions used in analysis.

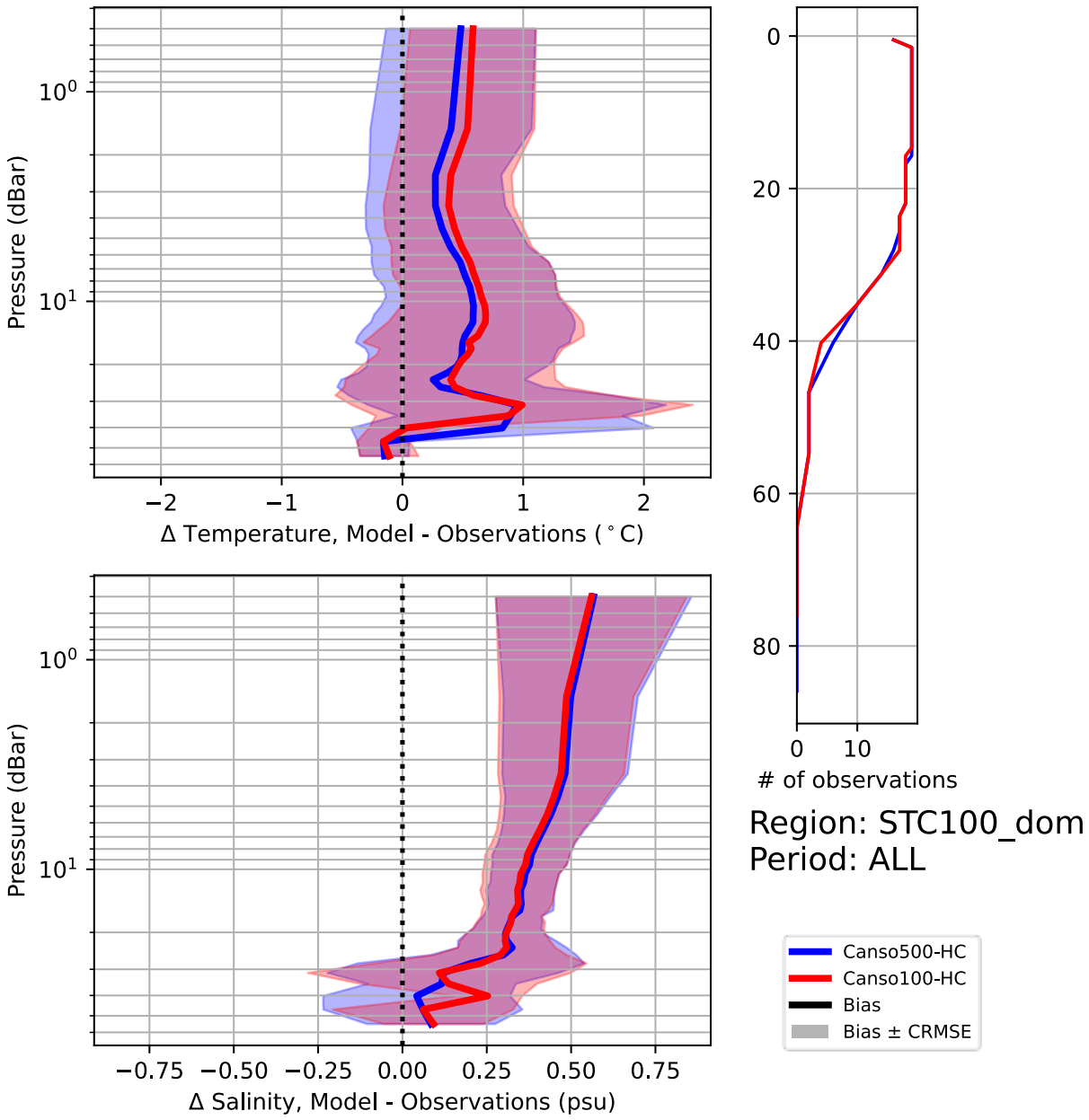

Figure 41. Profiles of CTD T-S bias ± CRMSE for inner region (STC100_dom).

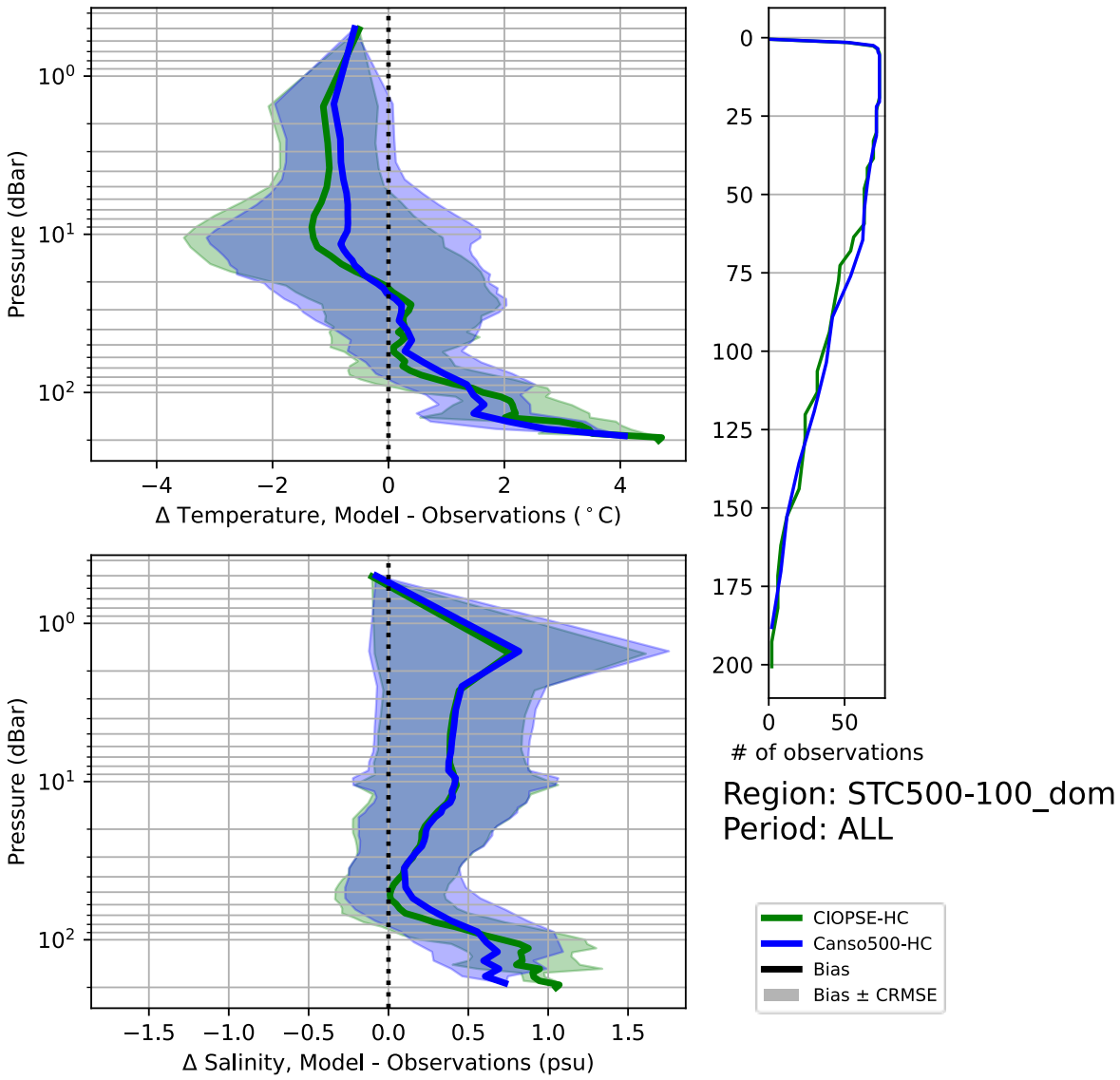

Figure 42. Profiles of CTD T-S bias ± CRMSE for outer region (STC500-100_dom).

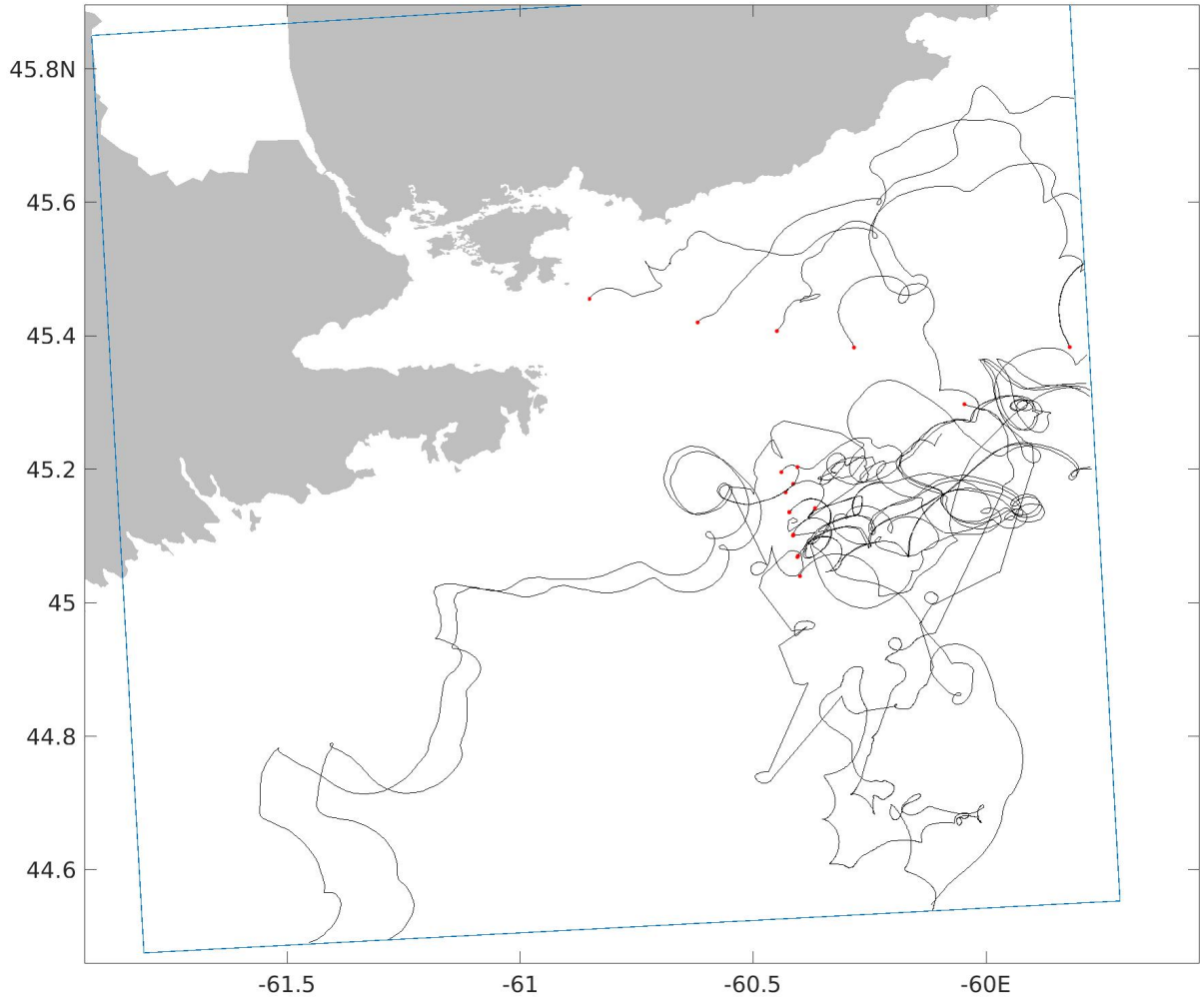

Figure 43. Observed drifter tracks. Red dots showing release location.

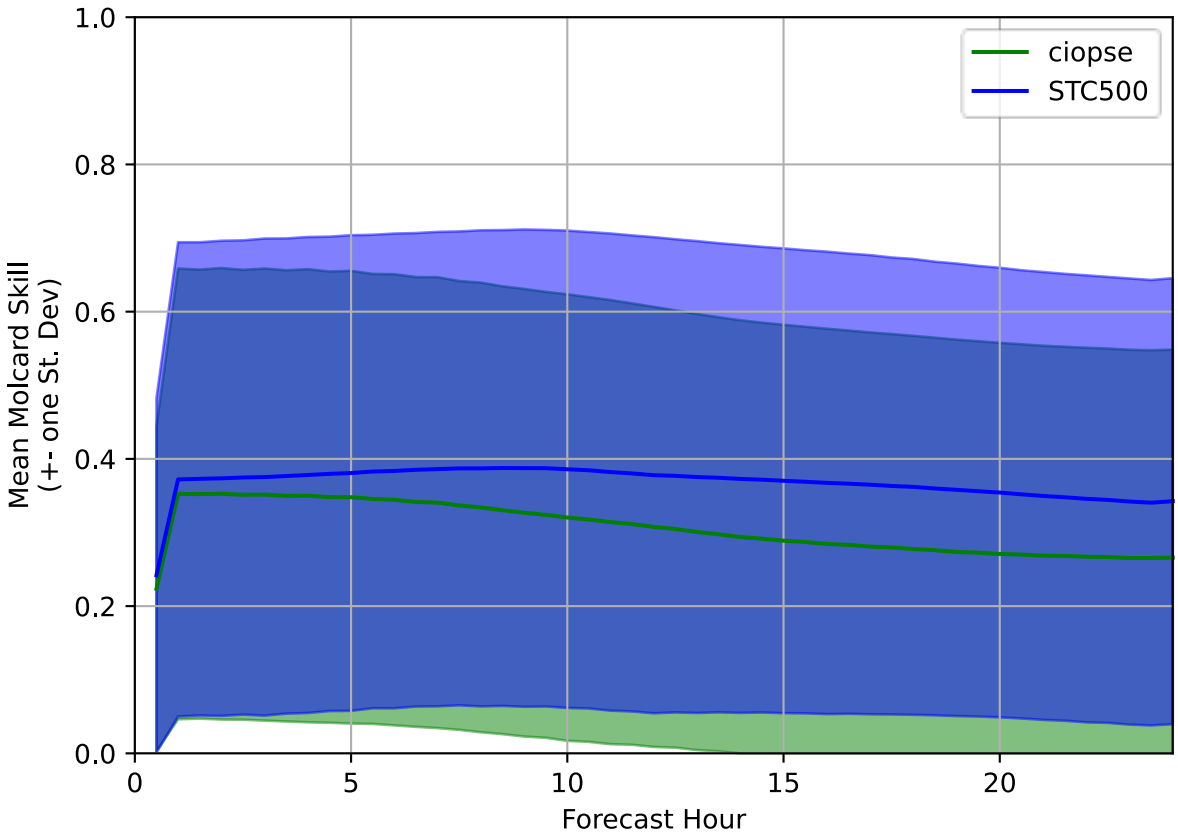

Figure 44. Molcard score from drift analysis.

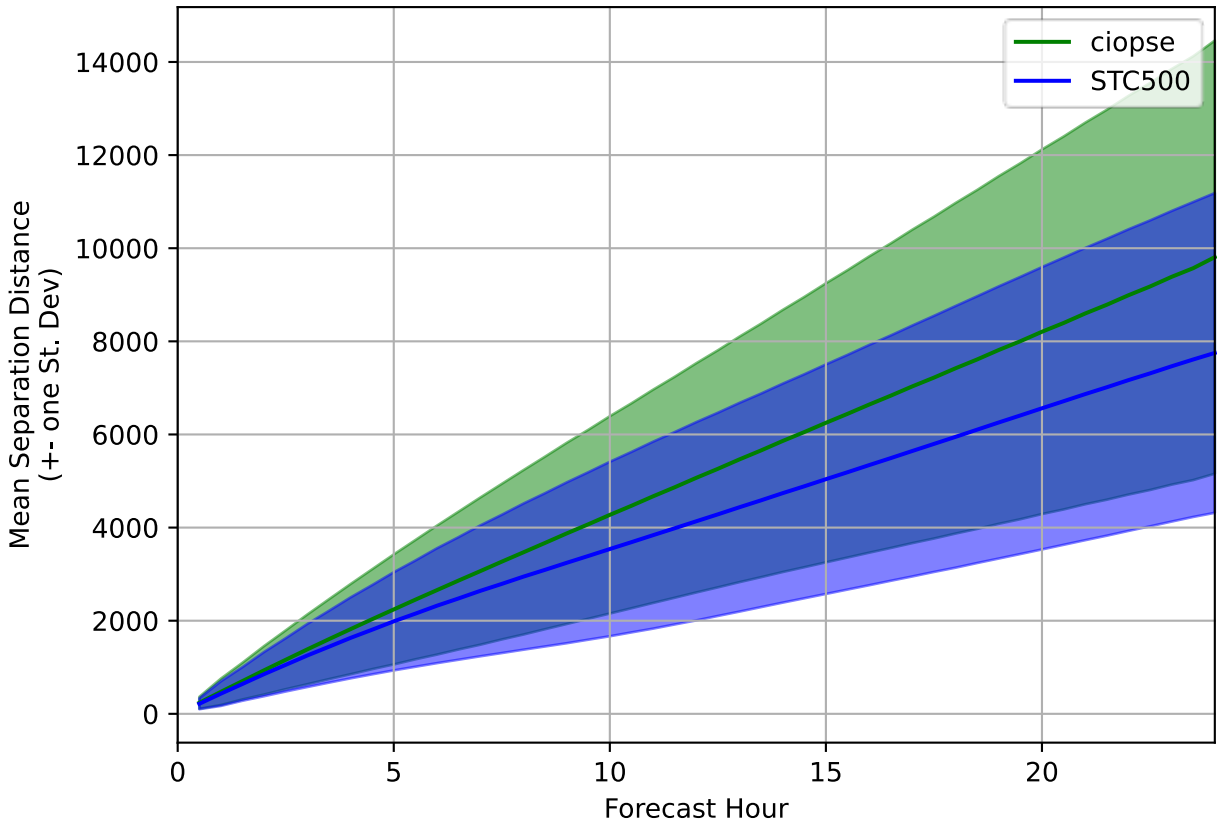

Figure 45. Separation distance from drift analysis.

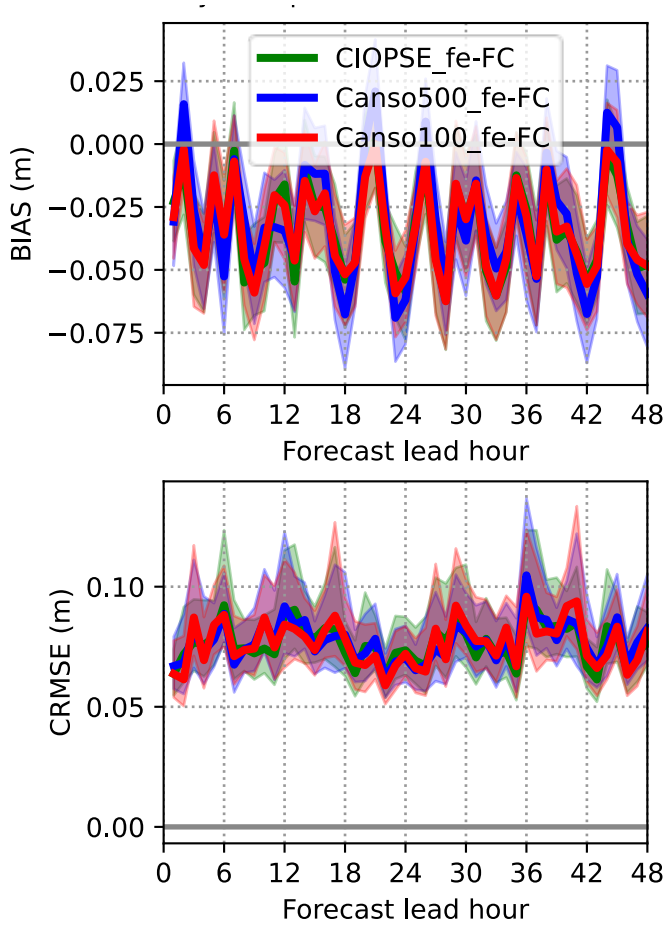

Figure 46. Bias and CRMSE as a function of forecast lead hour at Port Hawkesbury gauge. Highlighted envelopes depict 95% confidence limits with boot-strap estimates.